University of Nottingham
UK | CHINA | MALAYSIA

Performance Enhancement of Direct Torque-Controlled Permanent Magnet Synchronous Motor Drives for Electrified-Transportation Applications

by

Ahmed Nasr Mohamed Abdelwahed

A thesis submitted to the University of Nottingham for the degree of
Doctor of Philosophy, August 2022

Supervision committee:

Assoc. Prof. Chunyang Gu
Prof. Serhiy Bozhko
Prof. Chris Gerada

Abstract

The high-power density, low maintenance expense, and high efficiency of the PMSM drives have contributed to their widespread use in electrified transportation systems. Direct torque control (DTC) is widely adopted in PMSM drives to meet the torque control requirements of these systems. It uses two hysteresis regulators and a switching table to directly manipulate the switching states of the power converter, providing a fast dynamic response, simple structure, and high robustness. However, it is hard to provide adequate steady-state torque performance under different operating speeds because the hysteresis regulator cannot recognize the torque error magnitude, and the switching table cannot ensure the optimal switching transition.

Therefore, this dissertation has investigated the impact of the converter voltage vectors on the torque and flux performances under different operating conditions to identify the best option at each state in the switching table. Based on this investigation, the torque performance improvement is guaranteed through three main stages. First, a flexible switching table (FST)-based DTC strategy has been proposed, the structure of which changes according to the operating condition to minimize the torque ripple without the need for the hysteresis regulator. Then, a multiobjective duty-ratio regulator is employed to achieve further torque ripple reduction

and eliminate the steady-state torque error based on a virtual-reference signal. This improved-torque performance has not been provided only by applying double voltage vectors at each control interval but also by giving the highest priority to the voltage vectors that provide the lowest torque deviation during steady-state operation. Finally, a model predictive control (MPC)-based solution with low complexity is presented to guarantee the optimal voltage vector selection. In this solution, the unnecessary predictions are avoided, reducing the computational efforts, and the control objectives are considered separately, eliminating the need for a weighting factor. The feasibility and effectiveness of the proposed DTC strategies have been verified through comparative evaluations with existing schemes in the literature using a finite-element (FE)-based simulation system and an experimental setup of PMSM drive.

Acknowledgements

First and foremost I am extremely grateful to my supervisors, Dr. Chunyang Gu, Prof. Serhiy Bozhko, and Prof. Chris Gerada for their invaluable advice, continuous support, and patience during my PhD study. Their immense knowledge and plentiful experience have encouraged me in all the time of my academic research.

I would also like to sincerely thank Prof. Giampaolo Buticchi and Dr. Weiduo Zhao for their technical support on my study. I also would like to thank all the members in the power electronics machine control (PEMC) research group. It is their fruitful discussions and support that have made my study a wonderful time.

Last but not least, I would like to express my gratitude to my parents, my wife Sara, and my little son Younes. Without their tremendous understanding and encouragement in the past few years, it would be impossible for me to complete my study.

List of Publications

Journal Papers

1. **A. Nasr**, C. Gu, S. Bozhko, and C. Gerada, "Performance enhancement of direct torque-controlled permanent magnet synchronous motor with a flexible switching table," *Energies*, vol. 13, no. 8, p. 1907, Apr. 2020, doi: 10.3390/en13081907.

2. **A. Nasr**, C. Gu, X. Wang, G. Buticchi, S. Bozhko and C. Gerada, "Torque-performance improvement for direct torque-controlled PMSM drives based on duty-ratio regulation," in *IEEE Transactions on Power Electronics*, vol. 37, no. 1, pp. 749-760, Jan. 2022, doi: 10.1109/TPEL.2021.3093344.

3. **A. Nasr**, C. Gu, G. Buticchi, S. Bozhko and C. Gerada, "A low-complexity modulated model predictive torque and flux control strategy for PMSM drives without weighting factor," in *IEEE Journal of Emerging and Selected Topics in Power Electronics*, Feb. 2022, doi: 10.1109/JESTPE.2022.3152652.

Conference Papers

1. **A. Nasr**, C. Gu, W. Zhao, S. Bozhko and C. Gerada, "Torque ripple suppression for IPMSM using FEA-based model predictive direct torque control," *2021 IEEE Workshop on Electrical Machines Design, Control and Diagnosis (WEMDCD)*, 2021, pp. 204-209, doi: 10.1109/WEMDCD51469.2021.9425636.

2. **A. Nasr**, C. Gu, S. Ijaz, G. Buticchi, S. Bozhko and C. Gerada, "Sequential finite-element-based model predictive torque and flux control method for IPMSM," *2022 5th International Conference on Energy, Electrical and Power Engineering (CEEPE)*, 2022, pp. 1081-1086, doi: 10.1109/CEEPE55110.2022.9783432.

Contents

List of Tables

List of Figures

Nomenclature

2L-VSI Two-Level Voltage Source Inverter.

ANN Artificial Neural Network.

AST Switching Table with AVVs (presented in [48]).

AVV Active Voltage Vector.

BST Basic Switching Table (presented in [25]).

CDTC Conventional DTC.

CS-MPTFC Continuous-Set MPTFC.

DB Deadbeat.

DC Direct Current.

DDC Discrete Duty Controller.

DRM Duty Ratio Modulation.

DRR Duty Ratio Regulator.

DRR-DTC Duty Ratio Regulation-based DTC.

DSVM Discrete Space Vector Modulation.

DTC Direct Torque Control.

EMA Exponential Moving Average.

EMF Electromotive Force.

EV Electric Vehicle.

FE Finite Element.

FEA Finite Element Analysis.

FLC Fuzzy Logic Control.

FOC Field Oriented Control.

FS-MPTFC Finite-Set MPTFC.

FST Flexible Switching Table.

IM Induction Motor.

IPMSM Interior Permanent Magnet Synchronous Motor.

LPF Low Pass Filter.

M2PTFC Modulated MPTFC.

MBST Modified Basic Switching Table (presented in [84]).

MPTFC Model Predictive Torque and Flux Control.

MTPA Maximum Torque Per Ampere.

PI Proportional Integral.

PMSM Permanent Magnet Synchronous Motor.

PWM Pulse Width Modulation.

RMS Root Mean Square.

SMC Sliding Mode Controller.

SPMSM Surface-mounted PMSM.

SRM Switched Reluctance Motor.

ST-DTC Switching Table-based DTC.

SVM Space Vector Modulation.

SVM-DTC Space Vector Modulation-based DTC.

ZST Switching Table with ZVV at one state (presented in [85]).

ZVV Zero Voltage Vector.

Chapter 1

Introduction

This work focuses on torque control techniques of permanent magnet synchronous motor (PMSM) drives for electrified transportation systems. In this chapter, the research background, motivations, and scope of this thesis are introduced. Additionally, the novelties indexed to the following chapters are summarized.

1.1 Transportation-Systems Electrification

Because of the dependence on fossil fuel, transportation is one of the world's fastest-growing sources of carbon dioxide emissions, accounting for about one-fifth of global emissions in the past four years [1]. These emissions are the major contributor to climatic change and public health issues. As a result, standards and regulations have been implemented over the years in many countries to limit transportation-related emissions. For example, more than 20 countries had declared restrictions on the sales of conventional vehicles or constrained all new sales to be zero-emission vehicles by the end of 2020 [2]. Transportation electrification is considered one of the promising

solutions to commit to these policies, especially in countries that depend on renewables or nuclear to generate their electricity needs. The electric vehicles (EVs) market reflects a clear picture of the growth rate of the electrified transportation systems demand. In 2020, the global EV stock hit the 10 million mark, increasing by 43% compared to 2019. China achieved the highest annual sales volume of 3.5 million EV units in 2021, with a yearly production volume of around 4.1 million EVs [2].

1.1.1 Advantages Compared with Traditional Systems

In all forms of transportation, the motion is generated through the mechanical forces/moments produced by mechanical devices (effectors) such as tires, propellers, jets, fins, and rudders. The direction and magnitude of these forces are controlled using power transfer systems (actuators) [3]. In conventional transportation systems, the actuators can be hydraulic or pneumatic, where the motion is respectively generated based on pressurized oil or air [4]. Transportation electrification refers to the replacement of the conventional power transfer systems with more efficient and clean electrical systems to drive both propulsion and non-propulsion loads. The electrical drive systems can achieve the following advantages compared to the others:

- They are easier to be monitored and communicated than the others, reducing failure rates and increasing the productivity. Additionally, they can be controlled to achieve optimal efficiency and dynamic performance [5].
- They enhance the steps towards automated and smart vehicles that can improve the efficiency of transportation methods and boost the countries economy [6].

- They require simple power wiring, avoiding the arrangements needed in other systems for pressurization network and the corresponding audible noise, safety issues (such as leakages and fire hazards), and need for installation space and regular maintenance [4].
- They allow the regenerative-braking operation mode, recovering some of the mechanical energy that usually wasted in conventional vehicles by friction during deceleration. This contributes to improve the urban fuel economy [5].

Therefore, the efforts of transportation electrification translate to a demand for higher power density and more efficient electric drive systems.

1.1.2 Torque-Driven Applications

In electrified transportation systems, many applications use the torque produced by an electric motor to control the effector and satisfy their motion control objectives. Examples of these applications are the dynamically-positioned vessels [7], the propulsion-controlled aircraft [8], and independent-drive EVs [9]. The common aspect of them is the distribution of several effectors in the system, aiming at performance improvement in steady-state and transient conditions. The control structure employed in these applications is often hierarchical with three levels, as shown in Fig. 1.1 [3]. The upper-level controller generates a vector of control efforts (i.e., forces or

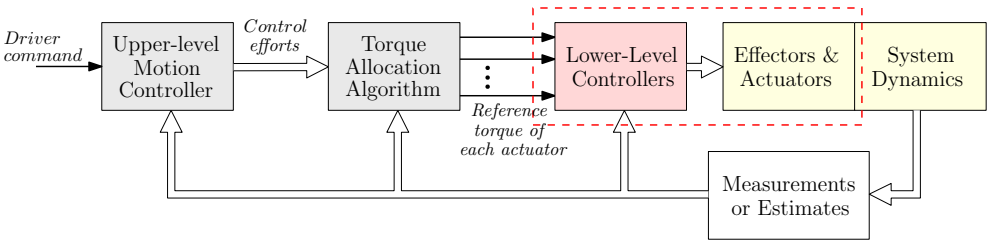

Figure 1.1: Overall control structure of electrified transportation system.

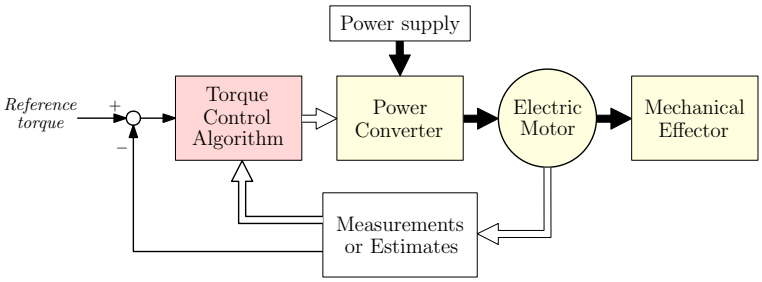

Figure 1.2: Block diagram of the typical closed-loop torque control scheme.

moments) according to the overall motion control objectives and the driver demands. Then, a middle-level controller allocates the total commanded forces and moments to each effector according to the allocation algorithm considering performance requirements, such as energy efficiency maximization and tear-and-wear minimization [3]. Finally, a lower-level controller is designed to control the torque of each actuator to achieve the demanded magnitude and direction of forces using the effector. The realization of this controller is typically implemented using a closed-loop control technique, shown in Fig. 1.2, where the motor torque is measured or estimated for comparison with the reference torque and, in response to the error, the power fed to the motor is accordingly adjusted using power-electronic devices [10]. Hence, the reliability, efficiency, and power density of the electric motor along with the performance achieved by the torque control algorithm are of undoubted importance to accurately satisfy the motion control objectives of the transportation application.

1.2 Electric Machines in Electrified Transportation

The electric motors play essential roles for the energy conversion in the electrified transportation. They provide much higher efficiencies than the inter-

nal combustion engines utilized in conventional transportation, consuming less energy. Also, they are faster in response time, and the matching between their torque-speed characteristics and the application requirements can be considered during the preliminary design process [11].

The commonly considered electric motors in electrified transportation are direct current (DC) motors, induction motors (IMs), switched reluctance motors (SRMs), and permanent magnet synchronous motors (PMSMs) [12]. The advantages and disadvantages of each type are summarized in Table 1.1. Among these motors, PMSMs possess many features favorable in the transportation industry. Unlike DC motors, PMSMs do not use brushes or mechanical commutators. As a result, they have a longer lifetime, smaller size, and better reliability as almost no maintenance is needed. Compared with IMs, both PMSM and SRM provides higher efficiency, as their rotor structure includes neither squirrel cage nor copper winding (i.e., no ohmic losses by the rotor). However, the former depends on permanent magnets to produce the rotor magnetic field, achieving much higher power density than IMs and SRMs [6]. Hence, PMSMs are more suitable for transportation applications where the installation space for the electric drive is limited. Due to these advantages, PMSMs are extensively adopted in various transportation applications, ranging from electric scooters [13] to aircraft [14].

As shown in Fig. 1.3, PMSMs adopted in electrified transportation can be classified into two main types according to the arrangement of the permanent magnets: surface-mounted PMSMs (SPMSMs) with magnets attached to the rotor core surface and interior PMSMs (IPMSMs) with magnets buried inside the rotor core. Table 1.2 summarizes the main features of SPMSM and IPMSM. In both motors, electromagnetic torque is imparted on the rotor due to the interaction between the magnetic flux of

Table 1.1: Advantages and disadvantages of different electric motors.

Motors	**Advantages**	**Disadvantages**
DC motor	• High starting torque. • Simple speed control.	• Bulky construction. • Brushes cause malfunctions. • Require regular maintenance. • Low efficiency.
IM	• Universal availability. • Simple and rugged structure. • Low noise and torque ripple. • Low maintenance cost.	• Low efficiency. • Poor power factor. • High starting current.
SRM	• Simple and robust structure. • Low cost. • High efficiency at high speeds.	• Low efficiency at low speed. • High torque ripple, noise, and vibration.
PMSM	• High efficiency. • High power density. • Silent operation. • Maintenance-free operation. • Allow high-torque operation.	• High initial cost due to magnets. • Magnets are sensitive to high temperature.

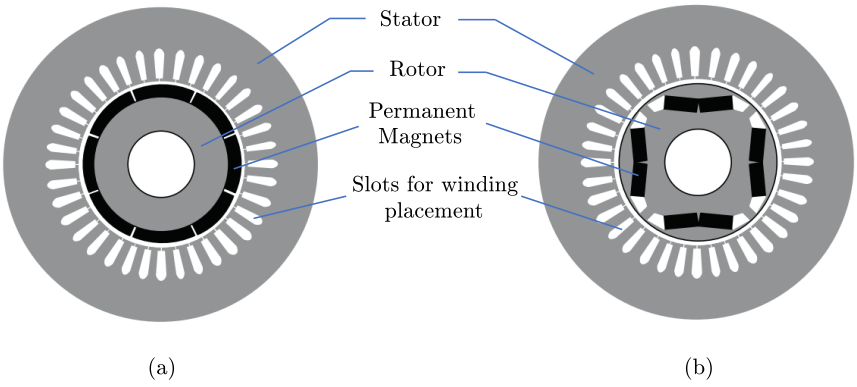

Figure 1.3: Axial view of the typical PMSM types. (a) SPMSM. (b) IPMSM.

the permanent magnets and the current following through the stator winding placed in the stator core slots [15]. IPMSM can produce an additional torque component (reluctance torque) due to the rotor saliency that represents the ratio between the highest and lowest magnetic permeabilities of the magnetic path [4], providing higher torque to volume ratio compared to SPMSMs (if they use similar magnets size). Also, IPMSM allows higher op-

Table 1.2: Main features of SPMSM and IPMSM.

IPMSM	**SPMSM**
• Higher torque density.	• Simpler structure.
• Wider constant-power range.	• Better torque quality.
• Allow higher operating speeds.	• Allow larger tolerances.
• Better flux weakening capability.	• Simpler modeling and control.

erating speeds because the magnets are well protected inside the rotor core from mechanical shock, centrifugal forces, or vibrations. Under high-speed operation, the back electromotive force (EMF) of the stator winding can exceed the terminal voltage. Hence, the excitation current angle should be adjusted such that the stator flux partially opposes the permanent magnet effect (i.e., flux weakening). Despite the resulting reduction of the electromagnetic torque, in that case, the additional reluctance torque of IPMSM allows an extended speed range compared to SPMSM [11]. For these reasons, IPMSM is preferred for traction systems where a wide-constant power operation region is crucial [16].

On the other hand, the rotor geometry of IPMSM is more complex than that of SPMSM, which means that the time and cost involved in manufacturing are higher for the former. Furthermore, SPMSM allows larger design tolerances, which can be desired in a direct drive motor where vibrations can cause excessive friction between the stator and rotor cores [17]. The effective air gap in SPMSM is uniform and relatively larger than that in IPMSM because the permeability of both magnets and air is approximately similar. Consequently, the stator winding inductance of SPMSM can be considered independent of the angular position of the rotor, and the magnetic saturation is less significant [18]. These results in simpler modeling and control techniques of SPMSM. Moreover, if SPMSM has similar dimensions as those of IPMSM, it offers lower inertia and faster

dynamic response with better torque quality [19]. Thus, SPMSMs are widely adopted in many applications, such as high-precision actuators [20] and direct-drive appliances [17].

1.3 The Need for High-Performance Torque Controller

The electromagnetic torque of a motor is the fundamental control target of motor drive systems, as it can provide a precise control for the position or speed of driven loads. To achieve that, the torque control technique obtains the necessary voltage adjustment on the motor terminals by governing a power converter.

As mentioned in 1.1.2, the reference torque is decided based on higher-level controllers and the driver command to achieve the motion control objectives of the transportation system, which needs to be tracked by the electric drive with the following requirements:

- Fast and accurate tracking of the reference torque during transient conditions can improve the transportation system maneuverability and guarantee stability [21, 22].
- Torque tracking with minimum steady-state ripple can avoid both acoustic noise and vibration that reduce ride comfort and cause wear and tear of the mechanical components (such as the shaft, bearings, and loads) [23, 24].
- Power consumption and losses minimization can improve the overall system efficiency and reduce the need for cooling setup (i.e., cost reduction) [21].

- Reduced number of sensors required for measurement can improve the reliability and reduce the control complexity and cost [25].
- Low complexity of the control algorithm to reduce the price of control hardware and allow short sampling intervals [26].

To meet the torque performance requirements, field-oriented control (FOC) and direct torque control (DTC) have become the most commonly adopted control schemes since they were first introduced around 1970 [27] and 1990 [28], respectively. In FOC, the torque is indirectly controlled by separating the stator current vector into two components in a rotating reference frame synchronized with the rotor flux vector. Then, two current control loops are employed to obtain the stator voltage components. This voltage is synthesized on the motor terminals using the power converter with pulse width modulation (PWM) technique [29]. Thus, accurate information of the rotor angular position is necessary in FOC for the reference frame synchronization, which can usually be measured using an encoder or resolver mounted on the rotor shaft.

On the other hand, the torque is directly controlled in DTC through the angular position of the stator flux vector relative to the rotor flux vector without the need for rotating-frame transformation. Therefore, the DTC is inherently a sensorless control technique. Also, DTC employs two hysteresis regulators and a switching table to directly decide the switching states of the power devices of the converter and adjust the stator terminal voltage without the need for current control loops or a particular PWM strategy. As a result, the DTC can guarantee faster torque dynamic performance with lower switching frequency and an uncomplicated control structure than the FOC [30]. However, it suffers from higher torque/stator-flux ripples and steady-state torque error. These performance issues are undesired

in electric drives, as they cause mechanical vibration, acoustic noise, and weak torque tracking capability. Consequently, many extensions have been presented in the literature for DTC of PMSM, such as on-line tuned hysteresis regulator [31, 24], duty ratio regulator [32–37], space vector modulation [38, 39], and model predictive control [40–47], as will be detailed in the following chapter (Section 2.3). However, these extensions either complicate the control implementation (by introducing additional control parameters or increasing the computational efforts), increase the switching frequency, or improve one of the torque performance indices while degrading the other (for example, achieving torque ripple reduction with increased steady-state torque error).

1.4 Objectives and Novelties of the Thesis

The main goal of this research is to improve the torque performance of DTC without degrading its fast dynamic response or complicating the control implementation. To achieve this, the following objectives have been considered:

- Investigation of the DTC principle for PMSM drives and analyzing the sources of the torque ripple and steady-state error.
- Generalized theoretical analysis for the impact of each switching state of the power converter on the torque and flux responses of the PMSM.
- Assessment of switching tables with different structures from the perspective of that theoretical analysis to select the switching states according to the operating condition.
- Investigation of torque ripple minimization in both rotation directions using a flexible switching table without hysteresis regulators.

- Evaluation of the conventional and flexible switching tables in both simulations and experiments.
- Investigation of an advanced duty ratio regulator for DTC, aiming at achieving further torque ripple reduction while eliminating the steady-state error.
- Experimental evaluation of the advanced DTC with duty ratio regulator compared to relevant methods existing in the literature.
- Investigation of a computationally efficient model predictive solution for DTC to guarantee the optimal switching state while avoiding the unnecessary weighted evaluation of all the possible switching options of the power converter.
- Simulation and experimental evaluation of both the classical and simplified solutions.

According to these objectives, the contributions of this thesis can be summarized as follows:

- A performance-improved DTC strategy has been proposed, which employs a flexible switching table that changes its structure according to the operating conditions. Compared to the conventional schemes, the proposed strategy achieves the lowest torque ripple with reduced flux ripple and average switching frequency. Also, it further simplifies the control implementation by removing the hysteresis regulators.
- An enhanced duty-ratio regulation method has been developed to provide further torque-performance improvement for DTC of PMSM. In this method, a duty ratio regulator is utilized not only to control the switching instants of the power converter but also to restrict the switching states that cause high torque pulsations during steady-state

operation. Moreover, a virtual reference generator is used to eliminate the steady-state torque error and optimize the duty ratio calculation. Therefore, further torque ripple reduction is achieved with the minimum steady-state torque error while maintaining the fast dynamic response of the conventional DTC.

- A low-complexity model predictive solution for DTC of PMSM has been developed to guarantee the selection of the optimal switching states and the corresponding switching instant. First, it preselects two candidate switching states based on the torque error to avoid the unnecessary torque and flux predictions, reducing the computational efforts. Then, the switching instant of each candidate is determined considering the torque ripple minimization, and the optimal option is chosen based on the flux error. Therefore, the need for a weighting factor in the classical cost function is omitted, simplifying the control implementation.

1.5 Outlines of the Thesis

The rest of the thesis chapters is organized as follows:

Chapter 2 presents the literature review of the direct torque controlled PMSM drives, including main components, challenges, and attempts to address the performance issues.

Chapter 3 describes the simulation model of PMSM drive system and the experimental setup used to investigate and verify the torque performance under different control strategies.

Chapter 4 introduces a generalized investigation on how the torque

and flux responses are affected by the different switching states of the power converter. Then, a flexible switching table-based DTC strategy is proposed to enhance the steady-state performance of the PMSM drive. Simulation and experimental evaluation for both the classical methods and the proposed strategy are also presented.

Chapter 5 presents the advanced duty ratio regulation-based DTC with further reduced torque ripple and steady-state error. The feasibility and effectiveness of the proposed strategy are verified through a detailed comparative assessment with three conventional DTC schemes using experimental results obtained from the laboratory setup of a 0.75-kW PMSM drive.

Chapter 6 proposes a modulated model predictive control technique for DTC of PMSM with reduced complexity. First, the control set is analyzed to artificially omit the unnecessary switching states from the prediction stage. Then, the control objectives are separately satisfied based on duty ratio modulation and cost function evaluation to eliminate the need for a weighting factor. Finally, the effectiveness of the proposed control scheme is verified through a comparative assessment with the conventional methods by means of simulation and experimental results.

Chapter 7 summaries the key conclusion of this thesis and the recommendations for some potential research work that can be addressed in the future.

The story line of this thesis can be illustrated by Fig. 1.4.

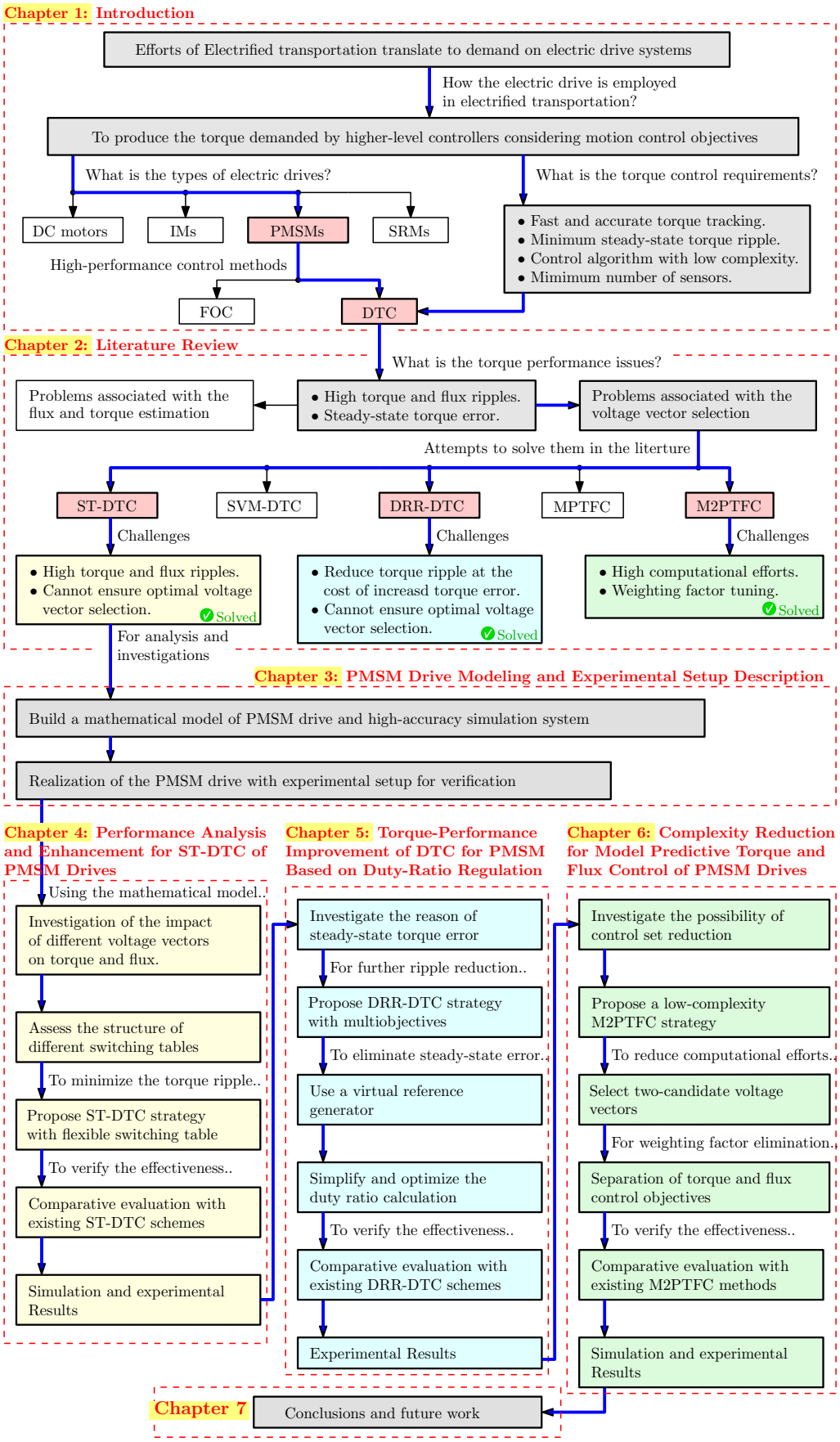

Figure 1.4: Story line of the thesis.

Chapter 2

Literature Review

2.1 Chapter Overview

The torque control technique plays a major rule for high-performance operation of motor drive systems, as it can precisely control the position or speed of the driven loads. It governs the power converter to satisfy the necessary voltage adjustment on the motor terminals, in order to force the torque to smoothly and accurately follow a predefined command depending on the application. With the recent massive development of micro-processors, semiconductor devices, and modeling techniques [15, 16, 48, 49], a considerable efforts have been dedicated to accomplish that aim. In this chapter, an introduction to the state-of-the-art torque control methodologies for PMSM drive systems is provided. Specifically, the operating principles of various classes of the direct torque control schemes are discussed along with their merits and demerits. The attempts to overcome the performance issues of these techniques are also revisited and discussed. The improved torque control methods are compared with the conventional control schemes, and important observations are summarized.

2.2 Overview of Direct Torque Control

Since direct torque control (DTC) was first implemented on PMSM drives by Zhong *et al* [50] in 1997, its analysis and development have become an ongoing research topic. The key idea of this control scheme is to directly manipulate the torque through control of the amplitude and angular position of the stator flux vector relative to the rotor flux vector [51]. Accordingly, the voltage vector applied to the machine winding needs to be adjusted to force the torque and stator flux amplitude to follow their reference values (T_e^{ref} and ψ_s^{ref}). As shown in Fig. 2.1, the core of DTC can be divided into four main steps:

1. Estimation of the torque and stator flux vector.
2. Identification of the reference stator flux amplitude.
3. Selection of the reference stator voltage vector.
4. Generation of the switching signals to synthesize the reference voltage vector.

The switching table-based DTC (ST-DTC) is the classical control scheme where the stator flux vector ($\boldsymbol{\psi}_{\alpha\beta}$) can be estimated using either the volt-

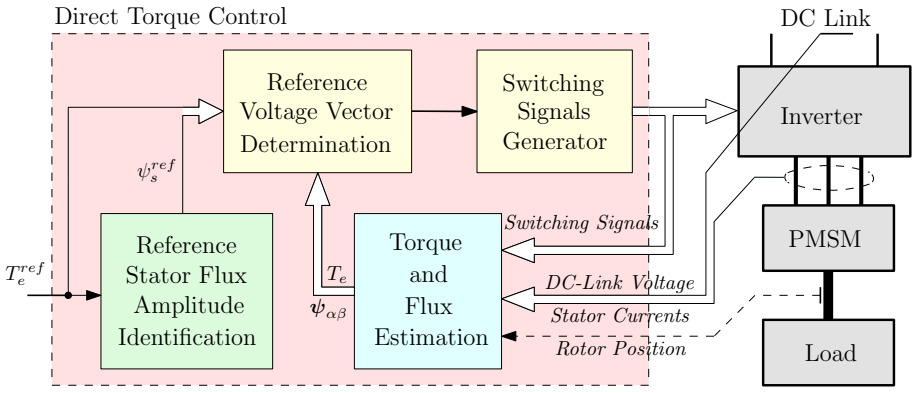

Figure 2.1: Block diagram of the DTC core.

age or current model of PMSM, which is then employed to estimate the torque (T_e) based on the measured stator current [52, 53], as shown in Fig. 2.2. Compared with the current model-based estimation, the voltage-based model is less parameter dependent (depends on the stator winding resistance only) and allows the position sensorless DTC if the starting rotor position is known to determine the initial stator flux [51]. Moreover, two hysteresis regulators and a look-up table are used to directly select the switching states to maintain the torque and stator flux amplitude within hysteresis bounds around their corresponding reference signals. This direct setting of the switching devices of the inverter eases the control implementation, while providing almost the theoretical maximum dynamic torque response. Also, it omits the need for a particular pulse width modulator (carrier-based or space-vector PWM), reducing the switching frequency and losses [54]. Therefore, ST-DTC has been increasingly popular control scheme in various high-performance PMSM drives [55, 56].

However, various issues associated with the ST-DTC components have been reported in the literature along with remedial strategies and exten-

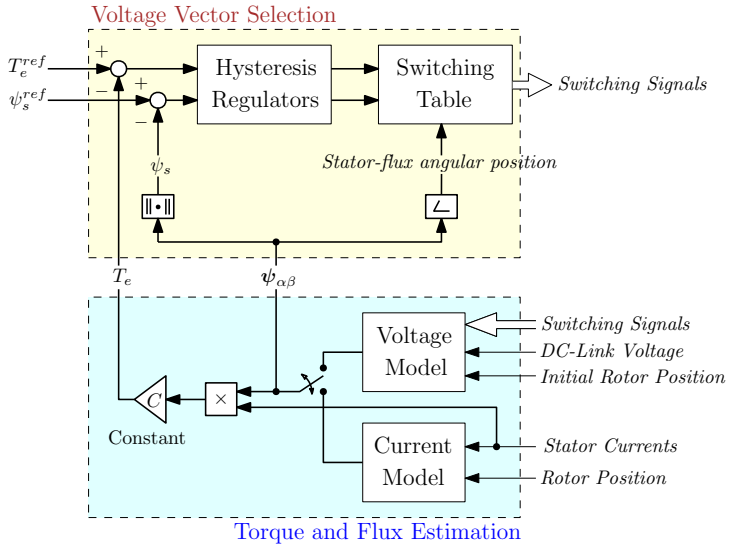

Figure 2.2: Block diagram of the ST-DTC structure.

sions to enhance the control performance and the system efficiency. The problems of the stator flux estimator are studied in [57], which can be summarized as follows:

- *Model-machine mismatch.* The voltage model used to estimate the stator flux vector is sensitive to the stator resistance that varies with the temperature. The model-machine mismatch deviates the stator flux modulus from its reference value, causing torque and speed oscillations [58]. To overcome this issue, the stator resistance is on-line tuned using either PI regulator [59, 57], fuzzy controller [60, 61], sliding-mode observer [62], recursive least square method [63], or analytical strategy [58]. A detailed comparison between these methods can be found in [64].
- *Sensitivity to DC offset.* In the voltage model-based flux estimation, the difference between the stator voltage and the voltage drop of the stator resistance needs to be integrated. This integration accumulates any DC offset in the measured DC-link voltage or stator currents, which causes instability. To avoid that, low-pass filter (LPF)-based solutions have been presented in [65–67] and comparatively evaluated in [68], [69] and [70]. To avoid stability issues of these solutions at low operating speeds, an accurate estimation of the stator frequency is needed to program the cut-off frequency of the LPF, which complicates the DTC implementation. Alternatively, adaptive flux observers have been proposed in [71–74], where the current model is used to correct the voltage model-based flux estimation.
- *Initial rotor position estimation.* Since the voltage model requires the rotor position information only during motor start, it is uneconomical to employ a position sensor for that purpose. Instead, initial position estimators have been presented in [75–78], which are based

on concepts, such as magnetic saliency, high-frequency signal injection, Kalman filters, and inductance identification [25]. Inaccurate estimation of the initial rotor position may cause instability or start the motor in the wrong rotation direction [57].

Because the sensorless control of PMSM drives is not the main objective of this work, the voltage model-based flux estimation and its corresponding extensions are not further discussed. Also, to avoid the implementation complexity and the stability issues of these estimators, a current model can be considered as a feasible choice for flux estimation of a PMSM laboratory prototype with a position sensor, assuming that the parameters are known and constant for the operating range of interest [30, 32, 33].

As for the reference stator flux amplitude in the ST-DTC, a constant value based on the permanent magnet flux is used [50], ignoring important control aspects, such as optimizing the drive system efficiency [62, 79, 80] and widening the operating-speed range [81]. The copper losses is minimized using a maximum torque per ampere (MTPA) strategy where the relationship between the reference torque and the reference stator flux amplitude obtained using either a look-up table [62] or a machine model [79]. The parameter dependence of these strategies can be avoided by deriving the torque-flux relationship in a different reference frame system [82] or using extremum-seeking control [83]. In [80], the reference stator flux amplitude is calculated based on the optimum flux- and torque-producing current components to minimize both the iron and copper losses.

The voltage vector selection based on hysteresis regulators and switching table causes high torque ripple and steady-state error. These issues are undesired in electric drives, as they produce mechanical vibration, acoustic noise, and weakens the torque tracking capability [23, 24]. The main

reasons for the torque performance degradation in ST-DTC can be summarized as follows:

- *Selection of the optimal voltage vector.* The fixed switching table does not guarantee selection of the voltage vector that minimizes the torque ripple. Although there are many modified switching tables that have been presented in [84–86] to reduce the torque ripple, the dynamic performance can be negatively affected. Hence, model predictive control-based solutions have been used in [87, 88], where all the possible voltage vectors are evaluated at every control cycle using a cost function, ensuring the optimal voltage vector selection.

- *Sampling frequency.* The selected voltage vector is applied for the entire control period, which is unnecessary in many cases. As a result, the sampling frequency needs to be high to reduce the torque ripple, imposing high requirements of the digital signal processor used for DTC implementation [89]. As a solution, duty ratio regulators (DRRs) are utilized in [32–36] where two or more voltage vectors are applied every control cycle.

- *Hysteresis boundaries tuning.* Because the hysteresis regulators cannot recognize the magnitude of the torque error, resulting in operating-condition-dependent switching frequency and inevitable steady-state torque error [90]. The torque boundaries can be adjusted using an external control loop to reduce the torque error [31, 24] and keep constant switching frequency [91].

- *Unitary implementation delay.* Ideally, the current measured at the sampling instant k is employed for torque and flux estimation, and the selected voltage vector is also applied at the sample k. However, due to digital implementation, these estimations need time, and the voltage vector will rather be applied at the start of the future control

sample $(k+1)$ [92]. Because the torque and flux at the $(k+1)$th sample turn into different values from those estimated at the kth sample, the DTC performance degrades if this delay is ignored. As a compensation, single-step prediction for the torque and flux is needed to select the proper voltage vector at the sampling instant $(k+1)$ [93].

The selection and synthesization techniques of the reference voltage vector play a major role to satisfy the desired torque performance in DTC of PMSM. The attempts of improving these techniques are further discussed in following section.

2.3 Improvements in Torque Performance of DTC

Various methodologies have been used to improve torque performance of DTC for PMSM drives, which can be categorized into three main classes: modification of the torque regulator and switching table, incorporation of multiple voltage vectors, and optimization of the voltage vector selection. These methodologies vary from each other in the sense of how the reference voltage vector is determined and synthesized, which are briefly outlined, as shown in Fig. 2.3.

2.3.1 Modifying the Torque Regulator and Switching Table

Many research works attempt to improve torque performance of DTC by modifying the torque regulator and the switching table, retaining the ease

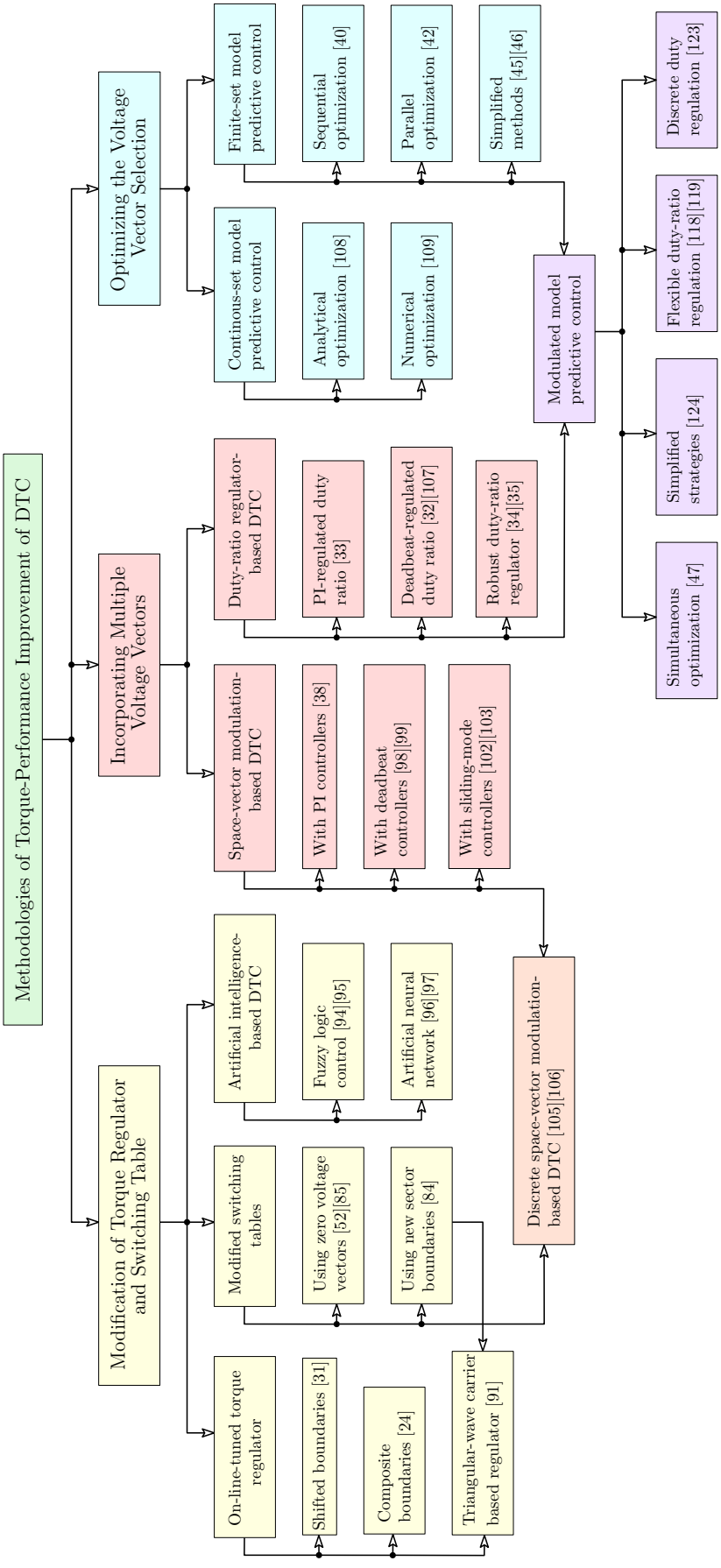

Figure 2.3: Overview of the methodologies used to improve torque performance of DTC.

of implementation of the conventional scheme. The modification of the torque regulator focuses on providing a dynamic hysteresis boundaries to eliminate the steady-state torque error [31, 24] or achieving constant switching frequency with torque ripple reduction [91]. As for the switching table, the structure is modified in terms of the included voltage vectors and the number of table states, in order to reduce the torque ripple [50, 52, 84, 85]. Other studies replaced the hysteresis regulators and switching table with artificial intelligent-based strategies, including fuzzy logic control (FLC) [94, 95] and artificial neural networks (ANNs) [96, 97]. These methods maintain the robustness of the conventional scheme as there are no precise inputs needed, but they depend on the designer experience and complicate the control implementation [37].

2.3.1.1 On-line-tuned hysteresis regulators

Based on the idea that the average torque changes positively with the position of the hysteresis band relative to the reference torque, on-line tuned hysteresis torque regulators have been proposed in [31, 24]. In [31], both the upper- and lower-hysteresis boundaries of the torque regulator are shifted by a distance depending on the average error between the reference and estimated torque signals. For this purpose, a PI controller is employed to obtain the shifting distance. On the other hand, a composite torque regulator is used in [24], which incorporates two dynamic hysteresis boundaries to the original boundaries. The dynamic hysteresis boundaries are adjusted using two separate PI controllers and an indicator for the average values of the positive and negative torque errors. Although employing either the shifted- and composite-hysteresis-based torque regulators can eliminate the steady-state torque error in DTC, the latter can provide a slightly higher torque-ripple reduction. However, both methods have no consideration for

the high torque ripple caused by the application of only one voltage vector for the entire control cycle.

2.3.1.2 Modified switching tables

Different switching tables have been proposed in [50, 52, 84, 85], which vary according to the number of levels of the torque hysteresis controller, the inclusion of the zero voltage vectors (ZVVs), and sector boundaries. The switching table used with the conventional DTC [50] requires a two-level (2L) hysteresis torque controller and employs only the six active voltage vectors (AVVs) provided by the two-level voltage source inverter (2L-VSI). In [52], the role of ZVVs in DTC systems of PMSM has been investigated, and a DTC strategy has been proposed using a three-level (3L) hysteresis torque comparator and a switching table similar to the basic one proposed in [28] for IMs. It is revealed in [52] that the torque ripple of the DTC system can be reduced using ZVVs, because they cause torque reduction with a lower rate than that of the AVVs.

A modified version of the basic switching table has been presented in [84] by redefining the boundaries of the sectors where the stator flux vector is located. The main control objective of this modification is the torque ripple reduction; however, it causes a higher stator flux ripple. The effect of using ZVVs at only one state of the switching table has been studied in [85], and the simulation results show that it can be beneficial for the steady-state performance and the average switching frequency. However, the dynamic response of the torque is not considered. In addition, according to the analysis of the ZVVs' effect on the DTC of the PMSM presented in [52], it is supposed to deteriorate when a torque reduction is commanded. Moreover, from a practical point of view, the control algorithm has to

be insensitive to the direction of rotation, but the switching table in [85] will not allow the motor speed reversal, as it employs ZVVs to reduce the torque and the stator flux. These switching tables are further discussed and compared in 4.4.

2.3.2 Incorporating Multiple Voltage Vectors

The limited number of admissible voltage vectors (with constant amplitude and angle) and the application of a single voltage vector for the entire control cycle can be considered as the principle causes of torque ripple in DTC. Hence, several investigations have been performed to solve this issue through allowing the control system to synthesize a higher number of voltage vectors than those utilized in the conventional DTC. In order to apply this principle, two or more voltage vectors are incorporated in each control cycle using a space-vector modulator (SVM) or a duty ratio regulator (DRR).

2.3.2.1 Space vector modulation-based DTC (SVM-DTC)

As shown in Fig. 2.4, SVM-DTC selects the reference voltage vector by using a PI controller and a model-based calculator instead of the hysteresis regulators and switching table [38, 39]. The PI controller generates the desired variation in the load angle $\Delta\delta$ (i.e., the variation in the angular position of the stator flux vector relative to the rotor flux vector) based on the instantaneous torque error. The desired variation in the load angle is utilized to calculate the reference angular position of the stator flux vector. Then, the machine model employs the reference stator flux vector to calculate the reference voltage vector that is then synthesized using SVM.

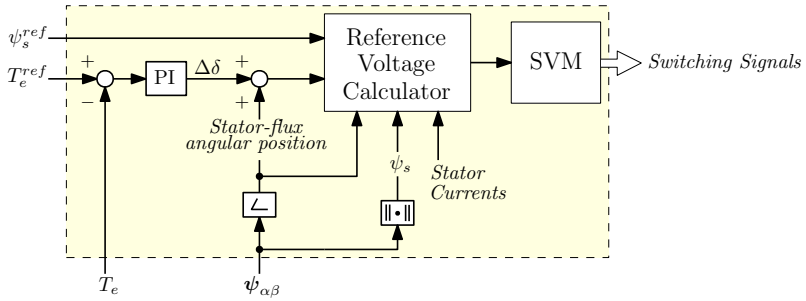

Figure 2.4: Block diagram of SVM-DTC.

Although this method can achieve lower torque ripple than the conventional scheme under the same sampling frequency, the PI controller can slow down the dynamic response if it is not properly tuned.

Instead, deadbeat (DB) controllers are utilized in [74, 98, 99] to improve both the steady-state and transient performances by a direct derivation of the desired deviation in the load angle from the demanded torque change using the machine model. However, this derivation causes other issues, such as the computation complexity and the reduced robustness against the parameters variation. In [100], simplified derivations are directly employed for reference voltage vector calculation based on the torque error without the need to obtain the load angle first. To enhance the robustness against parameters variation, an on-line parameter identification strategy can be integrated with the DB control system [101]. As an alternative solution, a sliding mode controller (SMC) is employed in [102, 103], which can handle the unknown disturbances and modeling inaccuracies, notwithstanding the high-frequency chattering in torque and flux [104].

The control issues associated with integrating either PI, DB, or SMC with SVM-DTC can be avoided by replacing the SVM with its discrete version (DSVM) that allows generating new candidate voltage vectors from the basic voltage vectors admitted in the classical DTC [105, 106]. These

candidate voltage vectors are sorted in a switching table, and the most appropriate voltage vector among them is selected using multi-level hysteresis regulators. The DSVM synthesizes the selected voltage vector by employing a number of basic voltage vectors for prefixed time periods at every control cycle. Thus, the higher the number of candidate voltage vectors is, the better steady-state torque performance will be. However, this higher the number of candidates requires a more complex switching table which cannot guarantee the selection of the optimal voltage vector. The DSVM-based DTC strategy can be considered as a compromise between the robustness and ease of implementation of the classical DTC, and the improved steady-state performance of the SVM-DTC. Nevertheless, the utilization of SVM or DSVM to synthesize the reference voltage vector results in higher switching frequency, which is undesirable in medium- and high-voltage drives [54].

2.3.2.2 Duty ratio regulator-based DTC (DRR-DTC)

The concept of duty ratio (D) regulation is introduced in the DTC to adjust the amplitude of the AVV selected from the switching table, aiming at reducing the torque ripple without increasing the sampling frequency. Thus, the reference voltage vector is synthesized in DRR-DTC by applying one AVV and one ZVV at every control period. Fig. 2.5 shows the basic control diagram of the DRR-DTC scheme.

Several DRR-DTC strategies have been presented in the literature [32–37], which vary in the sense of how the duty ratio is decided. In [32], the duty ratio is obtained such that it achieves a certain control objective, such as minimizing the torque error at the end of each control cycle or the root-mean-square (RMS) value of the torque ripple [107]. For this purpose, the

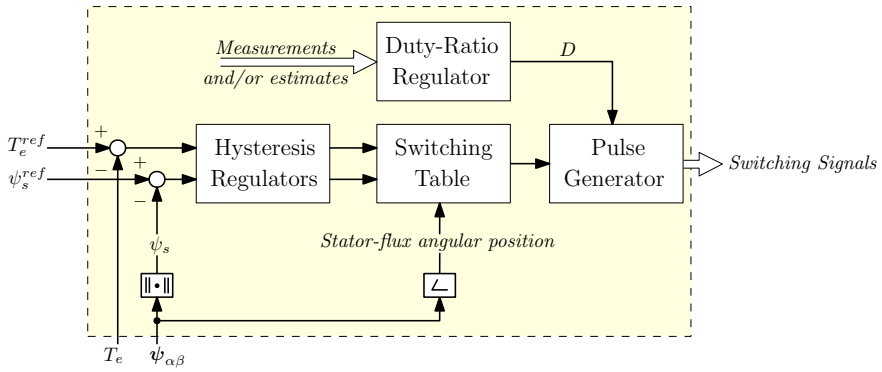

Figure 2.5: Block diagram of DRR-DTC.

impact of the selected voltage vector on the electromagnetic torque needs to be predicted using the machine model, which increases the calculation complexity and the reliance on the machine parameters. Consequently, a robust DRR has been proposed in [35], which calculates the duty cycle based on the weighted errors of torque and stator-flux amplitude. However, this method neglects the impact of the operating speed and load torque on the torque response, resulting in a considerable steady-state torque error compared to the classical DTC method.

On the other hand, the operating speed is considered while calculating the duty ratio in [34], reducing the steady-state torque error at the cost of higher torque ripple compared to the method presented in [35]. However, both methods in [35] and [34] include control parameters with no solution to get their optimal values. In [37], the duty ratio is calculated based on the deviation rates of the stator currents in the rotating reference frame instead of using that of the electromagnetic torque, introducing a weighting factor that can be set to reduce the flux ripple of the DRR-DTC strategy. For higher reliability, a PI controller is employed in [33] to determine the duty cycle depending on the torque error and the operating speed. These DRR-based methods are further discussed in 5.5. In addition to the duty ratio regulation, Foo and Zhang [91] maintained the switching frequency con-

stant by comparing the output of the PI regulator with a triangular-wave carrier signal. Because the PI regulator deteriorates the torque dynamic response in [91], a modified switching table has been proposed to replace the traditional table during system dynamics that can be indicated from the saturation state of the triangular-wave carrier-based comparator. Although the DRR-DTC strategies can achieve lower torque ripple compared to the conventional DTC scheme under the same sampling frequency, they cannot ensure the optimal torque performance because the dependence on switching table and hysteresis regulators to select the active voltage vector.

2.3.3 Optimizing the Voltage Vector Selection

To guarantee the optimal voltage vector selection, model predictive torque and flux control (MPTFC) has been introduced in many studies as an effective alternative to different forms of DTC. MPTFC uses the dynamics model of the PMSM under control to predict the trajectories of the controlled variables (i.e., torque and flux) for a certain prediction horizon. Then, a cost function is employed to obtain the optimal voltage vector that achieves predefined control objectives. Fig. 2.6 illustrates the basic idea of the optimal voltage vector selection in MPTFC when the prediction horizon is one sample. MPTFC can be divided into two families,

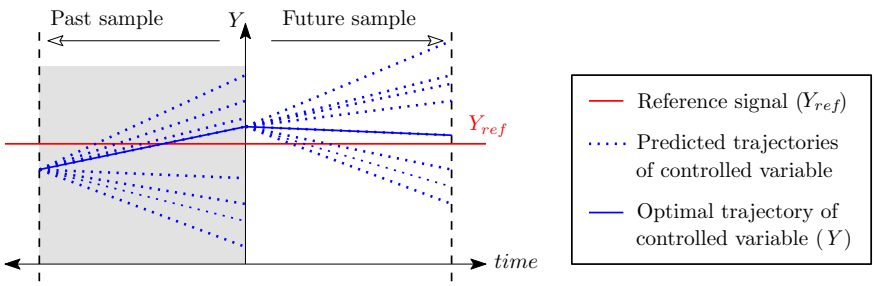

Figure 2.6: Sketch to illustrate the basic idea of the optimal voltage vector selection in MPTFC.

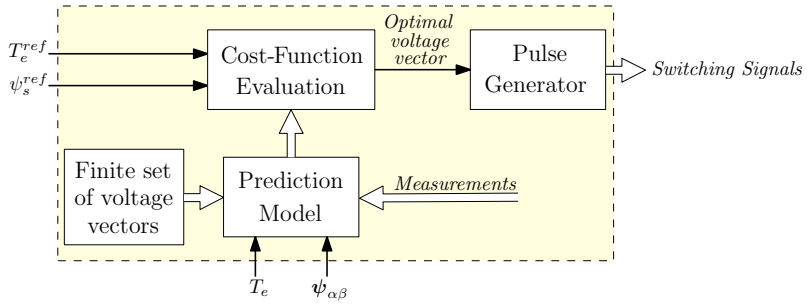

Figure 2.7: Block diagram of MPTFC.

namely, continuous-set (CS-MPTFC) and finite-set (FS-MPTFC) [108]. CS-MPTFC solves an online-optimization problem to find a continuous optimal voltage vector, hence a SVM is needed [109]. On the other hand, FS-MPTFC selects the optimal voltage vector among the finite control set admitted by the power converter, i.e., direct manipulation of the switching transitions [110]. Therefore, the FS-MPTFC can achieve faster dynamic response and lower switching losses [109, 111], and it will be further discussed in the following subsections.

2.3.3.1 Model predictive torque and flux control

Fig. 2.7 shows the block diagram of MPTFC. Compared with ST-DTC and DRR-DTC, MPTFC achieves better steady-state performance regarding the torque and flux ripples by ensuring selection of the optimal voltage vector at every control cycle [112, 87]. There are two main drawbacks in the conventional MPTFC, which are undesired in practical implementation. First, the cost function includes different control objectives, such as the trajectory error in torque and flux. As a result, a weighting factor with complex tuning procedures is required [113, 114]. Moreover, it needs a high sampling rate for further torque ripple reduction, requiring intensive computations for the prediction stage [115].

To solve the first problem, various investigations attempt to omit the weighting factor using either sequential or parallel optimization strategy [40–44]. In these strategies, a cost function is defined for each control objective instead of the weighted multiobjective cost function, as shown in Fig. 2.8. From the point of view of each cost function, the admissible voltage vectors are ranked in a group of predefined number of candidates from which the optimal option can be selected. As shown in Fig. 2.8(a), the sequential MPTFC [40, 41] indicates the best two or three voltage vectors depending on the torque control objective, then selects the optimal candidate according to the flux control target. On the other hand, the parallel MPTFC [42, 43], shown in Fig. 2.8(b), evaluates the entire set of voltage vectors by an independent consideration for the control objectives. Based on these evaluations, the voltage vectors are sorted in two groups to indicate the best three candidates in each group. Then, the optimal voltage vector can be selected based on different criteria, such as common vector [44] and minimum cross error [43]. As a result, the parallel MPTFC provides better balance between the torque and flux control performances compared with the sequential technique. Despite the elimination of the need for a weighting factor by these methods, they need intensive computation because of the required predictions of torque and flux trajectories under all the possible voltage vectors of the inverter.

Therefore, other studies [45, 46] investigated simplifying the MPTFC scheme by using artificial preselection of a smaller number of candidate voltage vectors before the prediction stage. In [45], three voltage vectors are preselected from a modified switching table according to the torque error sign and the angular position of the stator flux vector. In [46], four candidate vectors are decided at every control cycle depending on the optimal voltage vector chosen in the past sample. These strategies can effectively

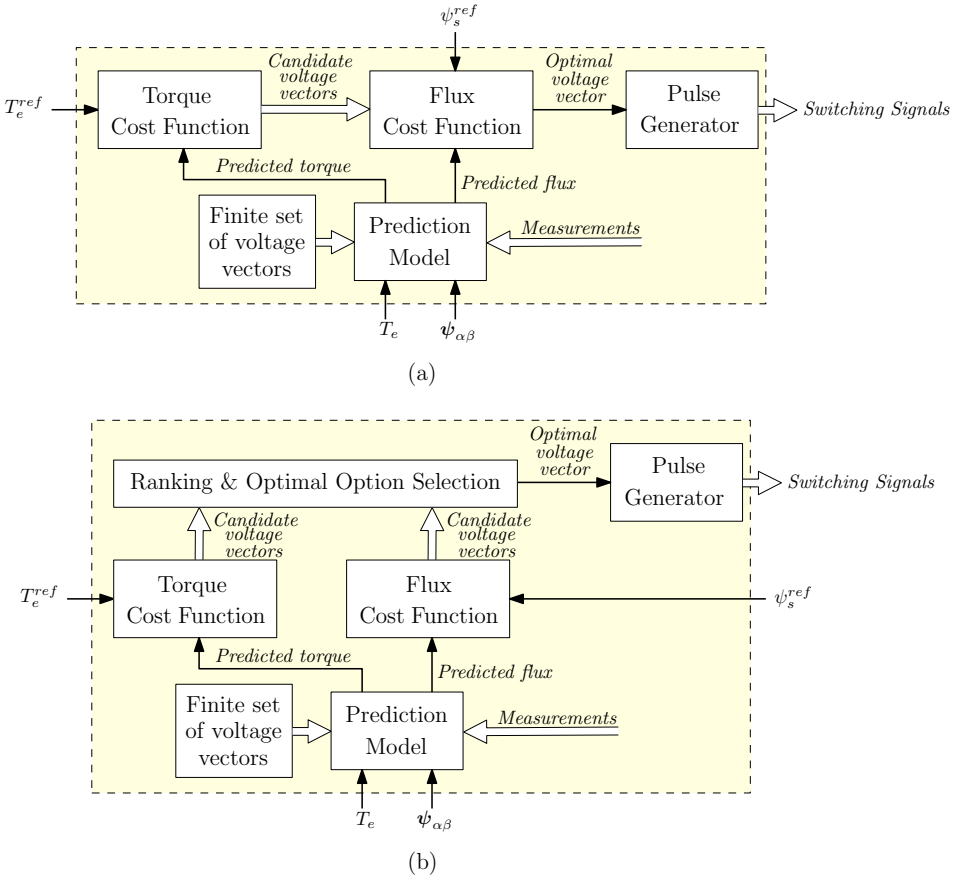

Figure 2.8: Block diagram of MPTFC without weighting factor. (a) Sequential MPTFC. (b) Parallel MPTFC

reduce the computation burden at the cost of a slight degradation of steady-state performance. The simplified methods presented in [40–46] does not consider the second issue, i.e., the need for high sampling frequency to achieve further torque ripple reduction.

2.3.3.2 Modulated model predictive torque and flux control

The second issue can be addressed by incorporating the duty-ratio modulation concept into MPTFC, as can be called modulated MPTFC (M2PTFC). In [116] and [117], after selecting the optimal voltage vector, its duty cycle is regulated based on different control targets, following the same concept adopted in DRR-DTC methods [32] (shown in Fig. 2.5). Although this

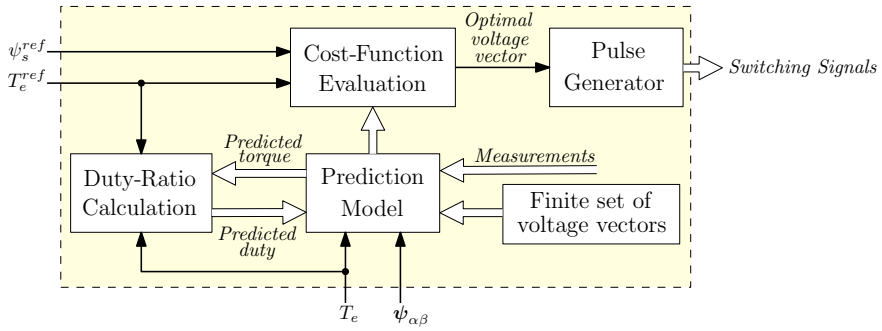

Figure 2.9: Block diagram of M2PTFC method.

duty regulation can provide lower torque ripple compared to the classical MPTFC, the resulting voltage vector from combining the optimal voltage vector with a ZVV cannot achieve the optimal torque performance because of ignoring the duty ratio during the cost function evaluation stage. Alternatively, the conventional M2PTFC presented in [47] optimizes the duty cycle for the admissible set of voltage vectors first to guarantee torque ripple reduction over a wide speed range. Then, the voltage vectors with their corresponding duties are simultaneously evaluated by a cost function to select the optimal solution that minimizes the torque and flux errors. Fig. 2.9 shows the block diagram of the M2PTFC scheme.

The flexibility of the conventional M2PTFC strategy has been enhanced in [118] and [119] to provide further torque ripple reduction. In [118], the total working duration of AVV and ZVV is derestricted from being equal to the control period, while in [119], the second voltage vector is exempted from being a ZVV. Zhou *et al.* [120] and Wang *et al.* [121] attempt to achieve more precise torque tracking behavior by extending the control set with additional virtual voltage vectors. Since the methods introduced in [47, 118–121] increase the number of admissible voltage combinations compared to those of MPTFC scheme, the computation burden is high, especially when the prediction horizon is higher than one [122]. These solutions are theoretically compared in 6.4.

2.4 Chapter Summary

This chapter has presented an overview of the classical DTC techniques, including the basic working principle, the control features, and the main reasons that cause torque performance issues. The remedial strategies for these issues have been briefly described. The review of the voltage vector selection criteria in different DTC methods has been provided in details. These include ST-DTC with modified switching table and on-line tuned hysteresis regulator, duty-ratio regulator-based DTC (DRR-DTC), space-vector modulation-based DTC (SVM-DTC), model predictive torque and flux control (MPTFC), and modulated model predictive control (M2PTFC). These methods are summarized in Table 2.1, accounting for the voltage vector selection technique, the considered torque control issue, and features of each control strategy.

From perspectives of both the steady-state and dynamic control behavior, DRR-DTC and M2PTFC are recommended because they can directly manipulate the converter switching transitions and apply a combination of two or more voltage vectors at every control cycle. Therefore, they provide fast dynamic response and good steady-state control performance without the need for high sampling and switching frequencies. However, an appropriate solution is desired to guarantee selection of the best voltage vector in DDR-DTC to further improve the steady-state torque performance in terms of ripple and steady-state error and omit the need for dynamic hysteresis boundaries. As for the M2PTFC, despite its ability of optimal voltage vector selection, the control implementation needs to be simplified by eliminating the need for a weighting factor, and the computation complexity can be reduced by avoiding the unnecessary torque and flux predictions.

Table 2.1: Summary of existing literature of voltage vector selection techniques in DTC

Control technique	**References**	**Voltage vector selection algorithm**	**Considered control performance issues**								**Features**
			T_e^{rip}	T_{sse}	ψ_s^{rip}	f_{sw}	f_s	DR	SD	CC	
ST-DTC	[50]	2L-HR + ST	□	-	□	□	□	■	□	-	Provide fast dynamic response.
	[85]		■	-	■	■	□	□	□	-	Employ ZVV at one of the switching table states to reduce torque ripple and switching frequency of [50].
	[52]	3L-HR + ST	■	-	-	□	□	■	□	-	Analyse the effect of ZVV inclusion in switching table on torque ripple reduction.
	[84]		■	-	□	□	□	□	□	-	Modify the switching table structure with new sector definition to reduce torque ripple.
	[24][31]	PI + HR + ST	□	■	□	■	□	■	□	■	Eliminate steady-state torque error using on-line tuned hysteresis torque regulator.
	[91]	PI + TWC + HR + ST	■	□	□	■	■	■	□	-	Fix the switching frequency and modify the switching table to avoid dynamic response degradation.
	[94][95][96]	FLC/ANN	■	□	■	□	□	-	□	-	Reduce torque and flux ripples.
SVM-DTC	[38][39]	PI + DB + SVM	■	-	■	□	■	□	-	-	Enhance the overall steady-state control performance using SVM.
	[98]	DB + SVM	■	-	■	□	■	■	-	■	Enhance the dynamic performance based on deadbeat solution.
	[99]		■	-	■	□	■	■	■	□	Use discrete flux observer to improve the robustness of DB against parameters variation.
	[100]		■	-	■	□	■	■	■	■	Derive the reference voltage vector directly from torque error to reduce the computation complexity.

T_e^{rip}: torque ripple, T_{sse}: steady-state torque error, ψ_s^{rip}: flux ripple, f_{sw}: switching frequency, f_s: sampling frequency, DR: dynamic response, SD: Step delay, CC: control complexity, HR: hysteresis regulator, ST: switching table, TWC: triangular wave carrier, "■": considered, "□": not considered, "-": not reported.

Table 2.1: Summary of existing literature of voltage vector selection techniques in DTC (continued)

Control technique	**References**	**Voltage vector selection algorithm**	**Considered control performance issues**								**Features**
			T_e^{rip}	T_{sse}	ψ_s^{rip}	f_{sw}	f_s	DR	SD	CC	
SVM-DTC	[102][103]	SMC + SVM	■	-	■	□	■	□	-	□	Enhance the steady-state control performance.
	[105][106]	HR + ST + DSVM	■	-	■	□	■	□	-	□	Increase number of possible voltage vectors to reduce torque and flux ripples.
DRR-DTC	[107]	HR + ST + DB	■	-	□	■	■	■	□	□	Minimize RMS-torque ripple while maintaining the fast dynamic response of ST-DTC.
	[32]		■	□	■	■	■	■	□	□	Balance torque- and flux-ripple reductions by introducing a weighting factor to duty ratio calculation.
	[37]		■	-	■	□	■	□	□	□	
	[35]	HR + ST + DRR	■	□	■	■	■	□	■	■	Simplify [107] and reduce torque ripple based on the weighted errors of torque and flux.
	[34]		□	■	□	■	■	■	□	■	Consider the impact of speed on torque slopes to reduce steady-state torque error of [35].
	[33]	ST + PI	■	□	■	■	■	□	□	■	Use PI controller to obtain the duty cycle based on rotor speed and torque error to simplify [107].
MPTFC	[112]	MP + CF	■	-	■	■	□	■	-	□	Minimize the switching frequency of the inverter.
	[113]		■	-	■	■	□	■	■	■	Employ fuzzy decision making technique for voltage vector selection to avoid weighting factors tuning.
	[114]		■	-	■	■	□	-	■	□	Optimize the weighting factors based on ANN.
	[40][41]		■	-	□	■	□	■	■	■	Eliminate the need for weighting factor by optimizing separate cost functions sequentially.

T_e^{rip}: torque ripple, T_{sse}: steady-state torque error, ψ_s^{rip}: flux ripple, f_{sw}: switching frequency, f_s: sampling frequency, DR: dynamic response, SD: Step delay, CC: control complexity, HR: hysteresis regulator, ST: switching table, MP: model prediction, CF: cost function, "■": considered, "□": not considered, "-": not reported.

Table 2.1: Summary of existing literature of voltage vector selection techniques in DTC (continued)

Control technique	**References**	**Voltage vector selection algorithm**	**Considered control performance issues**								**Features**
			T_e^{rip}	T_{sse}	ψ_s^{rip}	f_{sw}	f_s	DR	SD	CC	
MPTFC	[42][43][44]	MP + CF	■	-	■	■	□	■	■	■	Balance torque and flux performances of [40] using parallel optimization of cost functions.
	[45][46]	ST + MP + CF	□	-	□	■	□	■	■	■	Reduce the computation complexity via preselection stage for the candidate voltage vectors.
M2PTFC	[116]	MP + CF + DB	■	-	□	■	■	■	■	□	Regulate the duty cycle of optimal voltage vector to reduce torque ripple.
	[117]		■	-	■	■	■	■	□	□	Balance torque- and flux-ripple reductions by introducing a weighting factor to duty ratio calculation.
	[47]		■	□	■	■	■	■	■	□	Simultaneously Optimize the voltage vector the duty cycle calculation for further torque ripple reduction.
	[118][119]		■	-	■	■	■	■	■	□	Enhance the flexibility of [47] by derestricting either the second voltage vector or sampling period.
	[120][121]	MP + CF + ST + DB	■	-	■	□	■	■	■	□	Extend the control set to enhance the steady-state control performance.
	[123][124]	ST + CF + MP + DRR	□	-	□	■	■	■	■	■	Reduce the computation complexity via preselection stage for the candidate voltage vectors.

T_e^{rip}: torque ripple, T_{sse}: steady-state torque error, ψ_s^{rip}: flux ripple, f_{sw}: switching frequency, f_s: sampling frequency, DR: dynamic response, SD: Step delay, CC: control complexity, HR: hysteresis regulator, ST: switching table, MP: model prediction, CF: cost function, "■": considered, "□": not considered, "-": not reported.

Chapter 3

PMSM Drive Modeling and Experimental Setup Description

3.1 Chapter Overview

This chapter describes the simulation model of PMSM drive system and the experimental setup used to investigate and verify the torque performance under different control strategies.

First, the mathematical model of the two-level voltage source inverter (2L-VSI) is introduced. Then, the simplified model of PMSM in both stationary and rotating reference frames is presented, which is utilized for the theoretical analysis of DTC in the following chapters. Since this model ignores non-ideal machine characteristics, such as the saturation and spacial harmonics effects, a high-accuracy model is then introduced for an 80-kW IPMSM prototype to validate the generality of the analysis results in

Chapters 4 and 6. It is built in Matlab/Simulink by extracting the torque and stator-flux linkage data from the finite element analysis (FEA) and storing them in advance using lookup tables. This accurate model is also employed for a case study to suppress the torque ripple of IPMSM based on predictive control technique in Chapter 6. Finally, the test rig of PMSM drive used for experimental verification in Chapters 4, 5, and 6 is described.

3.2 Modeling of PMSM Drive System

3.2.1 Mathematical Model of 2L-VSI

Fig. 3.1 depicts the simplified circuit of a 2L-VSI that includes two switches for each of its three poles. The switching states of the three poles (S_1, S_2, and S_3) defines the on-and off-state of the upper switches as 1 and 0, respectively, while those of the lower switches must be the complements ($\bar{S}_1$, $\bar{S}_2$, and $\bar{S}_3$) to avoid the shoot-through situation.

Based on these switching states and the DC-link voltage (V_{dc}), the voltage applied to the PMSM terminals can be changed to control the output torque and flux, as will be further explained in 4.2. The terminal voltage

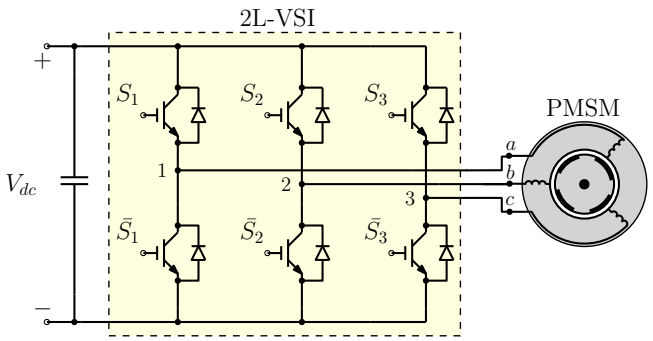

Figure 3.1: Schematic diagram of a 2L-VSI-fed PMSM.

(to the neutral of the machine winding) can be modeled as a function of S_1, S_2, S_3, and V_{dc} using (3.1), assuming that the winding are balanced star connected with a floating neutral [29].

$$\begin{cases} v_a = \frac{V_{dc}}{3}(2S_1 - S_2 - S_3) \\ v_b = \frac{V_{dc}}{3}(2S_2 - S_3 - S_1) \\ v_c = \frac{V_{dc}}{3}(2S_3 - S_1 - S_2). \end{cases} \tag{3.1}$$

3.2.2 Simplified Models of PMSM

The electrical dynamic behavior of the motor can be mainly represented by the voltage and torque equations in either the stationary coordinates (abc or $\alpha\beta$) or the rotating coordinates (dq), considering the following assumptions:

1. The stator-phase windings are identical and their spacial distribution is sinusoidal.
2. The thermal impact on the stator-winding resistance is neglected.
3. The saturation effect on the stator inductances are ignored.
4. The core losses are negligible.

These assumptions simplify the machine model significantly because they allow ignoring the stator flux linkage harmonics and the saturation effects on the machine parameters [4].

3.2.2.1 PMSM model in stationary coordinates

The stator voltage depends on the voltage drop of the stator-winding resistance R_s and the voltage induced by the stator-flux-linkage variation,

which can be expressed in $\alpha\beta$ coordinates as

$$\mathbf{v}_{\alpha\beta} = R_s \mathbf{i}_{\alpha\beta} + \frac{\mathrm{d}\boldsymbol{\psi}_{\alpha\beta}}{\mathrm{d}t}, \tag{3.2}$$

where $\mathbf{v}_{\alpha\beta} = (v_\alpha + jv_\beta)$, $\mathbf{i}_{\alpha\beta} = (i_\alpha + ji_\beta)$, and $\boldsymbol{\psi}_{\alpha\beta} = (\psi_\alpha + j\psi_\beta)$ denote the space vectors of the stator voltage, current, and flux linkages, respectively, which are defined using the Clarke's transformation (see Appendix A) as,

$$\mathbf{f}_{\alpha\beta} = \frac{2}{3}\left[f_a + f_b e^{j\frac{2\pi}{3}} + f_c e^{j\frac{4\pi}{3}}\right], \tag{3.3}$$

where f_a, f_b, and f_c are the instantaneous values of the three-phase stator voltages (v_a, v_b, and v_c), currents (i_a, i_b, and i_c), or flux linkages (ψ_a, ψ_b, and ψ_c).

The stator flux-linkage vector $\boldsymbol{\psi}_{\alpha\beta}$ depends on the stator currents and the permanent magnet flux ψ_{pm}, according to the following expression:

$$\begin{cases} \psi_\alpha = L_\alpha i_\alpha + L_{\alpha\beta} i_\beta + \psi_{pm} \cos\theta_r \\ \psi_\beta = L_{\alpha\beta} i_\alpha + L_\beta i_\beta + \psi_{pm} \sin\theta_r \ , \end{cases} \tag{3.4}$$

where θ_r represents the angular position of the rotor, L_α, L_β, and $L_{\alpha\beta}$ are the equivalent self and mutual inductances that can be represented as,

$$\begin{cases} L_\alpha = \frac{L_d + L_q}{2} + \frac{L_d - L_q}{2} \cos 2\theta_r \\ L_\beta = \frac{L_d + L_q}{2} - \frac{L_d - L_q}{2} \cos 2\theta_r \\ L_{\alpha\beta} = -\frac{L_d - L_q}{2} \sin 2\theta_r \ . \end{cases} \tag{3.5}$$

where L_d and L_q are the stator-winding inductances in dq axis.

The electromagnetic torque (T_e) developed by the machine can be obtained from the cross product of the stator-flux-linkage and -current

vectors, as follows:

$$T_e = \frac{3p}{2}\left(\psi_\alpha i_\beta - \psi_\beta i_\alpha\right), \tag{3.6}$$

where p denotes the number of pole pairs.

3.2.2.2 PMSM model in rotating coordinates

In the rotating coordinates, if the stator-voltage, -current, and -flux-linkage vectors ($\mathbf{v}_{dq} = (v_d + jv_q)$, $\mathbf{i}_{dq} = (i_d + ji_q)$, and $\boldsymbol{\psi}_{dq} = (\psi_d + j\psi_q)$, respectively) are denoted as $\mathbf{f}_{dq}$, they can be determined from (3.3) by employing Park's transform (see Appendix A) as,

$$\mathbf{f}_{dq} = \mathbf{f}_{\alpha\beta}\ e^{-j\theta_r}. \tag{3.7}$$

Substituting into (3.2) and (3.4) yields

$$\mathbf{v}_{dq} = R_s \mathbf{i}_{dq} + \frac{\mathrm{d}\boldsymbol{\psi}_{dq}}{\mathrm{d}t} + j\omega_r \boldsymbol{\psi}_{dq}\ , \tag{3.8}$$

and

$$\begin{cases} \psi_d = L_d i_d + \psi_{pm} \\ \psi_q = L_q i_q\ , \end{cases} \tag{3.9}$$

where ($\omega_r = \mathrm{d}\theta_r/\mathrm{d}t$) is the rotor angular speed. Also, the torque equation given in (3.6) can be rewritten as,

$$T_e = \frac{3p}{2}\left(\psi_d i_q - \psi_q i_d\right). \tag{3.10}$$

As can be noticed from (3.9), the rotor-position-dependent terms of the stator flux linkage are eliminated in dq axis, resulting in a further simplification of PMSM modeling. This model can satisfy acceptable accuracy

of performance prediction for SPMSM due to two reasons [16]:

1. The relatively large air gap between the stator and rotor cores results in insignificant saturation effects.

2. The non-salient rotor allows considering the winding inductances independent of rotor angular position.

Therefore, using SPMSM to analyse the torque control performance in Chapter 4 can be relatively simpler than IPMSM.

However, the simplified model fails in accurate representation of the IPMSM behavior because of the rotor saliency that not only introduces nonlinear torque-current characteristics but also causes a rotor position-dependent variation in the magnetic energy, leading to flux harmonics [18]. Furthermore, this saliency produces cogging torque resulting from the interaction between the rotor magnets and stator slots, which causes torque ripple that cannot be neglected [125]. Hence, an accurate model of an IPMSM prototype is presented in the following section.

3.2.3 High-Accuracy PMSM Model Based on FEA

Of the competing high-accuracy modeling techniques of IPMSM [126–131], the FE-based model in dq coordinates is potentially of the highest computational efficiency while taking into consideration non-ideal physical effects such as the non-sinusoidal flux distribution, cogging torque, and magnetic saturation [18]. The high accuracy of this model is guaranteed by extracting the flux linkage and electromagnetic torque data from FEA at different stator currents and rotor angular positions. Meanwhile, the low computation cost is ensured by sorting the extracted FEA data in advance via

either lookup tables or curve fitting as,

$$\begin{cases} \psi_d = f_1(i_d, i_q, \theta_r) \\ \psi_q = f_2(i_d, i_q, \theta_r) \end{cases} \tag{3.11}$$

$$T_e = f_3(i_d, i_q, \theta_r) \tag{3.12}$$

Hence, (3.11) and (3.12) can be respectively used instead of (3.9) and (3.10) to represent the stator voltage (3.8) and the electromagnetic torque in the FE-based model. However, to avoid the flux differentiation in (3.8), it is rewritten using Laplace transform as,

$$\begin{cases} \psi_d = \frac{1}{s}(v_d - R_s i_d + \omega_r \psi_q) \\ \psi_q = \frac{1}{s}(v_q - R_s i_q - \omega_r \psi_d), \end{cases} \tag{3.13}$$

where i_d and i_q is obtained by inversing the flux maps (3.11), as

$$\begin{cases} i_d = f_1^{-1}(\psi_d, \psi_q, \theta_r) \\ i_q = f_2^{-1}(\psi_d, \psi_q, \theta_r). \end{cases} \tag{3.14}$$

According to (3.12)-(3.14), the schematic diagram of the FE-based PMSM model can be represented, as shown in Fig. 3.2. It should be noted that if the angular position θ_r is set to zero, the model can capture only the effects of magnetic saturation while ignoring that of the spacial harmonics.

The FE-based model is demonstrated for an 80-kW IPMSM prototype with the specifications listed in Table 3.1. This machine has 48 slots and 4 pole pairs with N42UH magnets. Fig. 3.3 shows a complete view of the machine and its cross section.

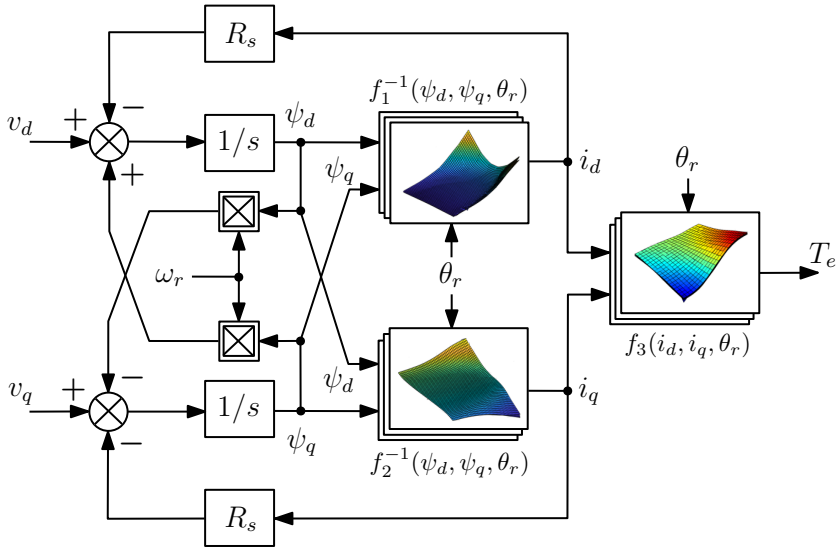

Figure 3.2: Block diagram of the FE-based IPMSM model.

Table 3.1: Specifications of the IPMSM prototype.

Electrical Parameters	**Symbols**	**Values**	**Units**
Stator-phase resistance	R_s	7.5e−3	Ω
Nominal power	P_{rated}	80	kW
Nominal torque	T_{rated}	400	N·m
Base speed	ω_{rn}	3000	r/min
Peak current	I_{peak}	400	A
DC-link voltage	V_{dc}	540	V
Inertia coefficient	J	0.16526	kg·m^2
Permanent-magnet flux	ψ_{pm}	0.1875	Wb
Mechanical Parameters	**Symbols**	**Values**	**Units**
Number of pole pairs	p	4	-
Number of slots	-	48	-
Number of turns per coil	-	12	-
Stator outer diameter	-	290	mm
Rotor outer diameter	-	193	mm
Axial length	-	200	mm
Air gap length	-	1	mm

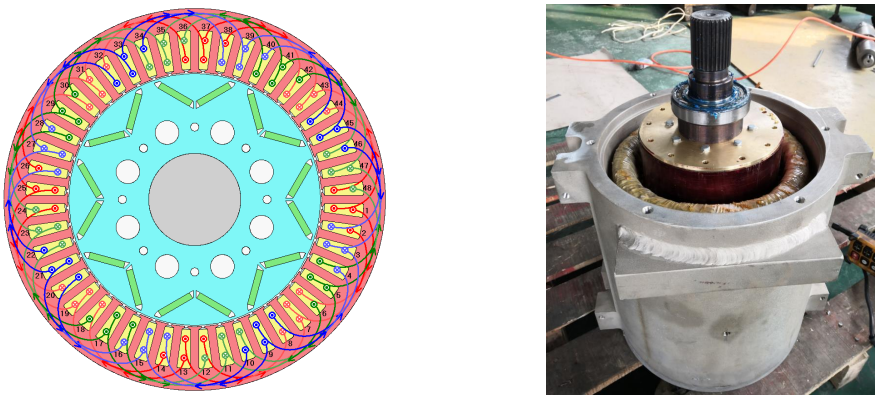

(a) (b)

Figure 3.3: The IPMSM prototype: (a) cross section; (b) complete view.

3.2.3.1 Matlab/Simulink implementation of FE-based IPMSM model

First, the FEA is used to determine the dq-flux linkages and electromagnetic torque at different operating points by varying i_d, i_q, and θ_r in the ranges of $[-400, 400]$ A, and $[0, 30]$ mechanical degrees with steps of 40 A, and 1 degree, respectively. The raw data determined by the FEA is processed using Matlab to generate lookup tables for the d- and q-axis flux linkage and the torque, as shown in Fig. 3.4.

The inverse solution of the flux-linkage maps is obtained using the surface fitting function (Gridfit) in Matlab [132]. This function can estimate the surfaces of $i_d(\psi_d, \psi_q)$ and $i_q(\psi_d, \psi_q)$ based on the scattered data of $\psi_d(i_d, i_q)$ and $\psi_q(i_d, i_q)$ at each rotor position θ_r. Because it requires the data nodes, as arguments, with the complete span, the minimum and maximum values of ψ_d and ψ_q are obtained, and the intervals are arbitrarily subdivided into 50 divisions. Although increasing the number of divisions improves the accuracy of the flux-maps inversion, the storage memory needed for the estimated data increases considerably. The inversed maps of d- and q-axis current versus flux linkages are depicted in Fig. 3.5.

Once the inversion of the flux-linkage maps has been accomplished, a validation is carried out by selecting different sets of i_d, i_q, and θ_r and use the original flux linkage maps to compute ψ_d and ψ_q that are employed to calculate new sets of i_d and i_q using the inversed maps. Fig. 3.6 shows the

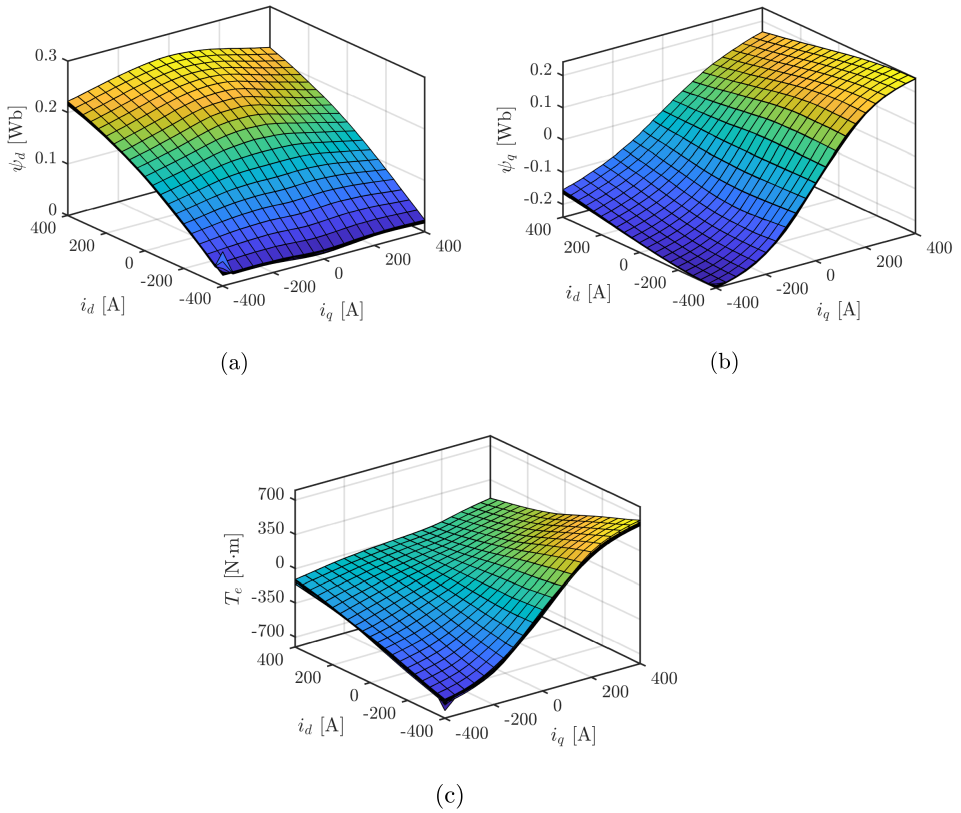

Figure 3.4: Flux linkage and torque maps versus dq-current components. (a) d-axis flux linkage. (b) q-axis flux linkage. (c) torque.

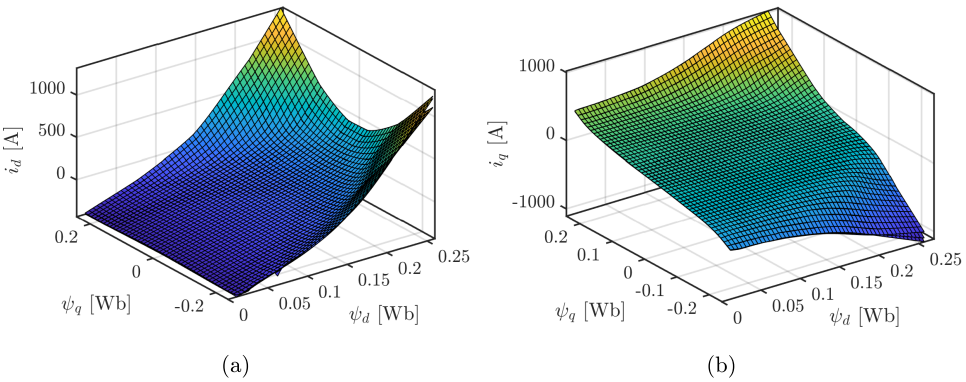

Figure 3.5: Current maps versus d- and q-axis flux linkages. (a) d-axis current. (b) q-axis current.

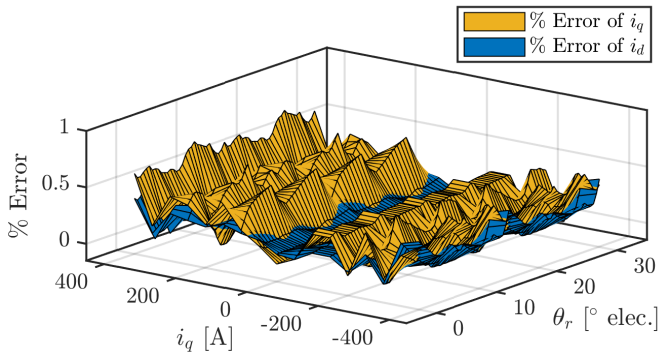

Figure 3.6: Percentage error in i_q prediction due to flux maps inversion at i_d= −100 A and different rotor positions.

percentage error in d- and q-axis currents at $i_d = -100$ A and different rotor positions. It can be noticed that the maximum current error is 0.7%. The error at different values of i_d were also checked, and they show similar magnitudes, verifying the flux maps inversion.

3.2.3.2 Verification of the FE-based simulation model

For verification, the FE-based model of the IPMSM prototype is implemented in Matlab/Simulink, and verified by experimental results. The IPMSM prototype is driven by a dynamometer, and the no-load test is performed to capture the back-EMF waveforms. Fig. 3.7 compares the Simulink-, FEA-, and experiment- line-to-line back EMF at an operating speed of 3000 r/min.

In Fig. 3.7, it can be noticed that the predicted back EMF using the Simulink model matches that of the FEA results, but the measured back EMF has a lower ripple because the rotor of the real machine prototype is skewed to reduce the interaction between the magnets and the stator teeth. The rotor skewing is ignored in the simulation to illustrate how the control method can eliminate the torque ripples caused by these interactions, as will be discussed in a case study of Chapter 6.

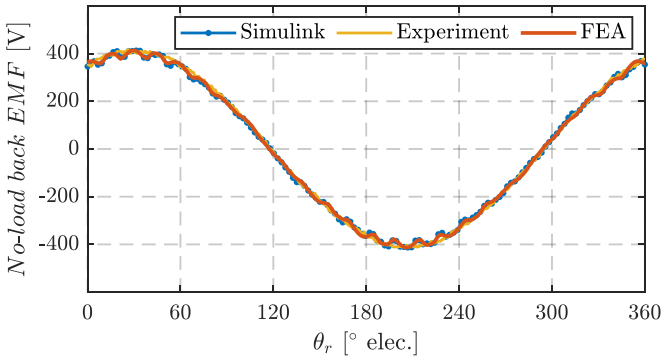

Figure 3.7: Simulink-, FEA-, and measured line-to-line back EMF waveforms at 3000 r/min.

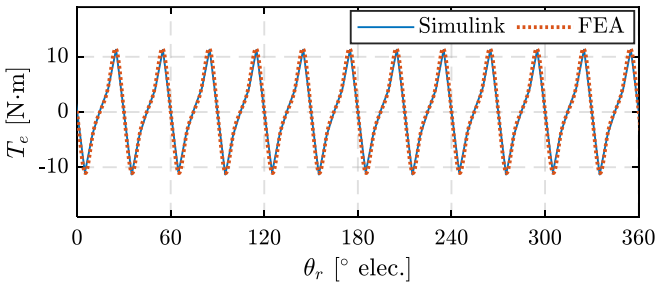

(a)

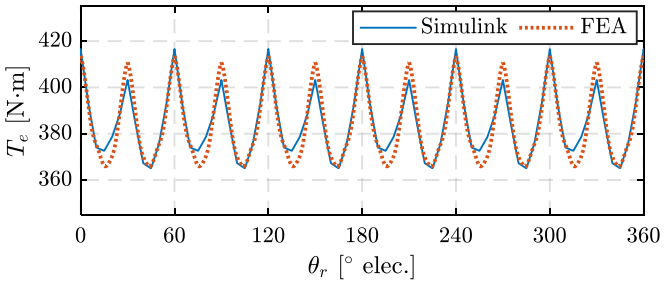

(b)

Figure 3.8: Simulink- and FEA-torque waveforms at (a) $i_d = 0$ A, $i_q = 0$ A, and (b) $i_d = -300$ A, $i_q = 200$ A.

Besides, to verify the torque prediction at different operating points, the currents ($i_d = 0$ A, $i_q = 0$ A) and ($i_d = -300$ A, $i_q = 200$ A) are given to FEA, and the resulting d- and q-axis flux linkages are then fed to the Simulink model to extract the torque waveforms that are compared in Fig. 3.8. It can be noticed that the torque waveforms coincide

at zero currents, while the difference at the other operating point can be neglected. These results validates the Simulink implementation of the FE-based IPMSM model.

3.2.4 Model of Motor-Driven Load

When the electromagnetic torque developed by the motor is applied to the driven load, the load variables, such as rotational speed and position, will be changed. The dynamic behavior of these variables can be mathematically represented by the well-known rotational analogue of the equation of motion expressed as [29]

$$J\frac{\mathrm{d}\omega_r}{\mathrm{d}t} + F\omega_r = p(T_e - T_l), \tag{3.15}$$

where J denotes the total moment of inertia (assumed constant), F is the coefficient of friction, and T_l represents the load torque. By neglecting the coefficient of friction F in (3.15), it can be implied that the load will accelerate when $T_e > T_l$, and it will decelerate if $T_e < T_l$. When $T_e = T_l$, the speed will remain constant.

During acceleration and constant-speed operation, the motor operates in forward or backward motoring mode, where the direction of the electromagnetic torque is the same as that of the rotational speed. On the other hand, braking is achieved by forcing the motor to develop a torque that opposes the direction of rotation. In this case, the motor operates in regenerative braking mode (acting as a generator), where the mechanical energy of the load is converted into electrical energy that can be supplied back to the energy source. These operation modes are summarized in Fig. 3.9 for both directions of rotation.

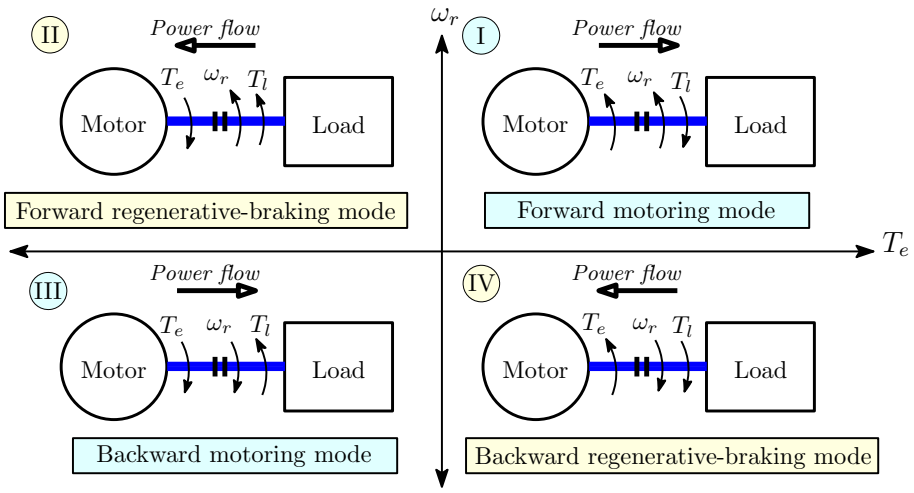

Figure 3.9: Operating modes of the electric drive system.

3.3 Simulation System Configuration

A simulation system of 2L-VSI-fed IPMSM drive has been built based on the FE-based model using Matlab/Simulink to test the torque control algorithms under the non-ideal machine characteristics. In this system, the IPMSM is driven in torque control mode where the operating speed is controlled via a virtual dynamometer, and the rotor angular position θ_r can be indicated based on that speed.

As shown in Fig. 3.10, the machine states (e.g., flux and torque) are given to the control system to decide the stator voltage that forces them to follow a predefined reference signals (i.e., T_e^{ref} and ψ_s^{ref}). According to (3.1), the dq-components of the stator voltage can be obtained by successively substituting into (3.3) and (3.7). This voltage is given to the FE-based model to determine the machine states.

The simulation system shown in Fig. 3.10 is utilized to verify the feasibility and effectiveness of the torque control strategies in Chapters 4 and 6 for IPMSM-based drive.

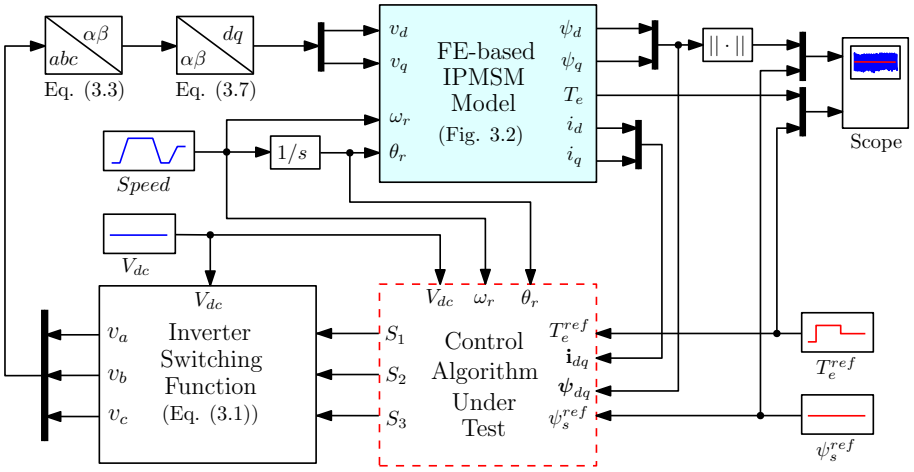

Figure 3.10: Simulation system of IPMSM drive system.

3.4 Experimental System Description

This section describes the experimental system used to investigate the torque control strategies of 2L-VSI-fed PMSM. Fig. 3.11 shows the block diagram of the experimental platform and its corresponding test bench structure.

The hardware of this test bench includes an 0.75-kW SPMSM, with the parameters listed in Table 3.2, that is fed by a 2L-VSI using the SiC-MOSFET power module (CCS050M12CM2) and its gate driver board (CGD15FB45P1). The DC side of the inverter is supplied from a programmable DC pwer source (DSP1050-42WE) and 200 μF voltage stabilizing capacitors (MKP1848S1010JY). A dSPACE DS1202 associated with a host PC is used as a control platform to implement the control algorithms and accomplish the corresponding sampling tasks for the measured states of the drive system. The stator-winding currents and the DC-side voltage are measured by LEM HAIS50-P and LV25-P sensors, respectively, while the rotor angular position is obtained using an incremental encoder with a resolution of 2500 pulse per revolution. Two interface boards are used

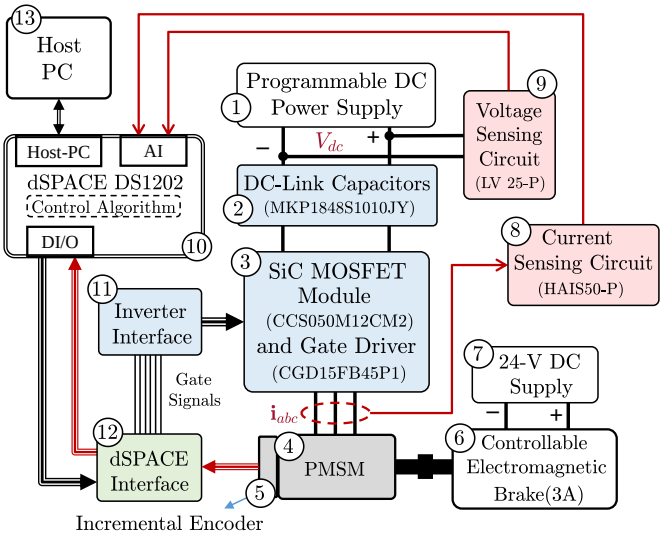

(a)

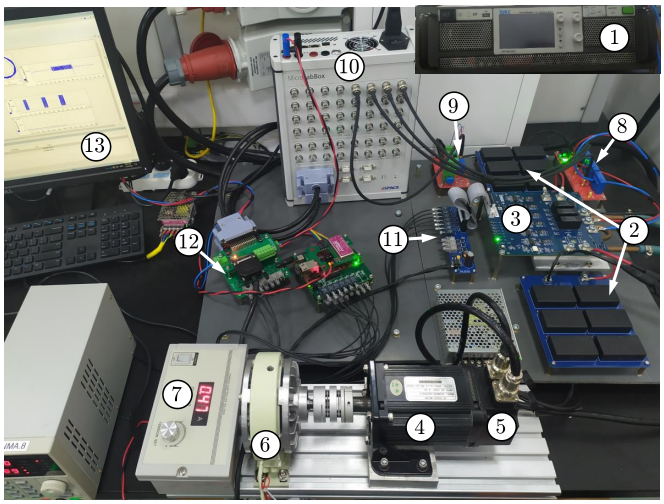

(b)

Figure 3.11: Experimental setup of PMSM drive system. (a) Block diagram. (b) Photo of the test bench.

between dSPACE controller and gate driver for signal isolation. The motor shaft is mechanically coupled to an electromagnetic brake supplied by an 0/24-V variable DC power source to control the load torque.

On the other hand, two softwares are employed to realize the experimental implementation of the control strategies. Before the experiment, Matlab/Simulink is used to establish a model for the control algorithm un-

Table 3.2: List of the SPMSM parameters.

Parameters	**Symbols**	**Values**	**Units**
Stator-phase resistance	R_s	0.901	Ω
dq-axis inductances	$L_d = L_q$	6.552	mH
Nominal power	P_{rated}	0.75	kW
Nominal torque	T_{rated}	2.4	N·m
Base speed	ω_{rn}	3000	r/min
Rated current	I_{rated}	4.2	A
DC-link voltage	V_{dc}	220	V
Moment of Inertia	J_m	1.2e−4	kg·m^2
Permanent-magnet flux	ψ_{pm}	0.09427	Wb

der test and perform the necessary compilation to generate the corresponding control code. Then, dSPACE ControlDesk is utilized to create a visual interface for users to download the code to the controller processing unit and directly change the reference signals and control parameters through the host PC. It can also be used to capture the experimental results for post processing, analysis, and drawing using Matlab. The captured results are used to assess the control performance using indices, such as torque ripple (T_e^{rip}), flux ripple (ψ_s^{rip}), steady-state torque error (T_{sse}), average switching frequency (f_{av}), and total harmonic distortion of stator current (THD$_I$), as defined in Appendix B. In the following chapters, the experimental verification of the relevant control strategies for PMSM drive has utilized such setup, but will not be detailed again.

3.5 Chapter Summary

This chapter has introduced the mathematical modeling for both 2L-VSI and PMSM of the drive system. Both the simplified and high-accuracy

models of PMSM have been discussed. The high-accuracy model of an 80-kW IPMSM prototype is implemented in Matlab/Simulink and verified through comparisons with the data extracted from FEA. The simulation system configuration that depends on the FE-based model has also been depicted. The lab-constructed test bench and the control algorithm implementation environment has been briefly described.

Chapter 4

Performance Analysis and Enhancement for ST-DTC of PMSM Drives

4.1 Chapter Overview

In the DTC schemes of two-level inverter-fed PMSM drives, the number of admissible voltage vectors is limited (only eight voltage vectors). Hence, the proper selection of the voltage vectors plays a significant role in the drive's ability to accurately follow the demanded torque and flux under different operating conditions. This chapter discusses and evaluates the voltage-selection strategy of the conventional ST-DTC implemented by using hysteresis regulators and a switching table. First, the mathematical models of PMSM and inverter, presented in Chapter 3, are used to analyze the impact of each voltage vector on torque and stator flux amplitude to assess the influence of different switching tables on the ST-DTC performance. Then, based on this analysis, the most appropriate voltage vector

at each state of the switching table is identified for both steady-state and dynamic conditions. Finally, an enhanced ST-DTC strategy with a flexible switching table (FST) is proposed, which can change the table structure according to the system operating state to reduce the torque and flux ripples and the average switching frequency while maintaining the main advantages of the conventional ST-DTC, such as the rapid dynamic response. It also eliminates the need for hysteresis regulators, simplifying the control implementation.

Since the theoretical analysis presented in this chapter is based on the simplified PMSM model, ignoring the non-ideal characteristics, the analysis results are validated using a high-accuracy simulation model that is built based on FEA (see Section 3.3). Moreover, the effectiveness and feasibility of the proposed FST are verified through a comparative evaluation with the existing switching tables using experimental results obtained from the 0.75-kW PMSM-drive system.

4.2 Principle of ST-DTC

As mentioned in 3.2.2, the dynamic performance of the PMSM can be represented in different coordinate systems. If the stationary coordinates are adopted with the assumption that $L_d = L_q = L_s$, (3.4) can be rewritten as follows,

$$\boldsymbol{\psi}_{\alpha\beta} = L_s \mathbf{i}_{\alpha\beta} + \psi_{pm} e^{j\theta_r}. \tag{4.1}$$

Substituting (4.1) into the torque equation (3.6) results,

$$T_e = \frac{3p\psi_s\psi_{pm}}{2L_s} \sin\left(\theta_s - \theta_r\right), \tag{4.2}$$

where ψ_s and θ_s are the amplitude and angular position of the stator-flux vector, respectively, which can be expressed as,

$$\begin{cases} \psi_s = \sqrt{{\psi_\alpha}^2 + {\psi_\beta}^2} \\ \theta_s = \arctan\left(\frac{\psi_\beta}{\psi_\alpha}\right). \end{cases} \tag{4.3}$$

Equation (4.2) implies that the motor torque depends on the phase shift between the stator-and rotor-flux vectors ($\theta_s - \theta_r$), assuming that the stator-flux amplitude is constant. This angle can be changed by manipulating the stator-flux vector because the electrical time constant of the machine is normally much smaller than the mechanical time constant [50]. According to the voltage equation (3.2), if the resistance is neglected, the stator-flux vector moves in the direction of the stator-voltage vector. Thus, the torque and the stator-flux amplitude can be controlled by selecting a proper voltage vector among those the two-level inverter admits.

The two-level inverter admits eight voltage vectors (illustrated by Fig. 4.1), the space vectors of which can be represented as [133]

$$\mathbf{V}_i = \frac{2V_{dc}}{3}\left(S_1[i] + S_2[i]e^{j\frac{2\pi}{3}} + S_3[i]e^{j\frac{4\pi}{3}}\right), \tag{4.4}$$

where i is the voltage-vector index and $i \in \{0,\ 1..,\ 7\}$. S_1, S_2, and S_3 are switching states, which are defined in Fig. 4.1(a) for each $\mathbf{V}_i$. Two of these voltage vectors are zero voltage vectors (ZVVs), i.e., $i \in \{0, 7\}$, while the others are active voltage vectors (AVVs).

The effect of the AVVs on the deviation direction (i.e., increase $\uparrow$ or decrease $\downarrow$) of the torque T_e and stator-flux amplitude ψ_s depends on the position of the stator flux vector $\boldsymbol{\psi}_{\alpha\beta}$ in $\alpha\beta$-plane that is divided into six sectors, as shown in Fig. 4.1(a). It can be said that $\boldsymbol{\psi}_{\alpha\beta}$ is located in the

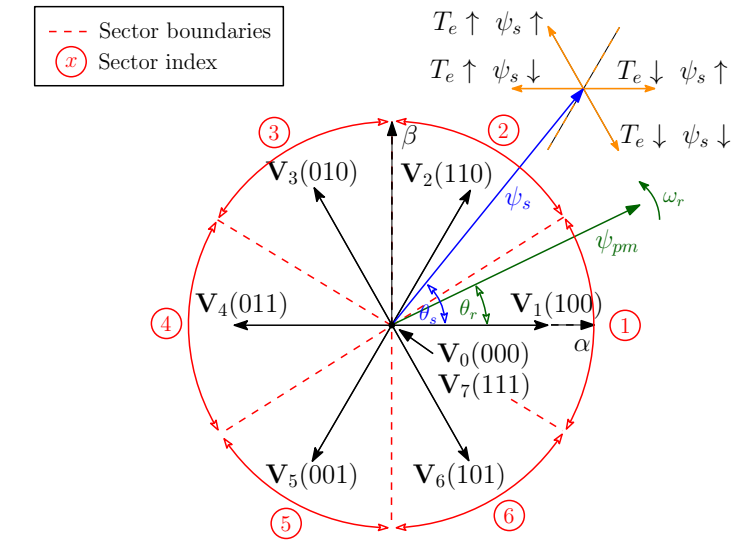

(a)

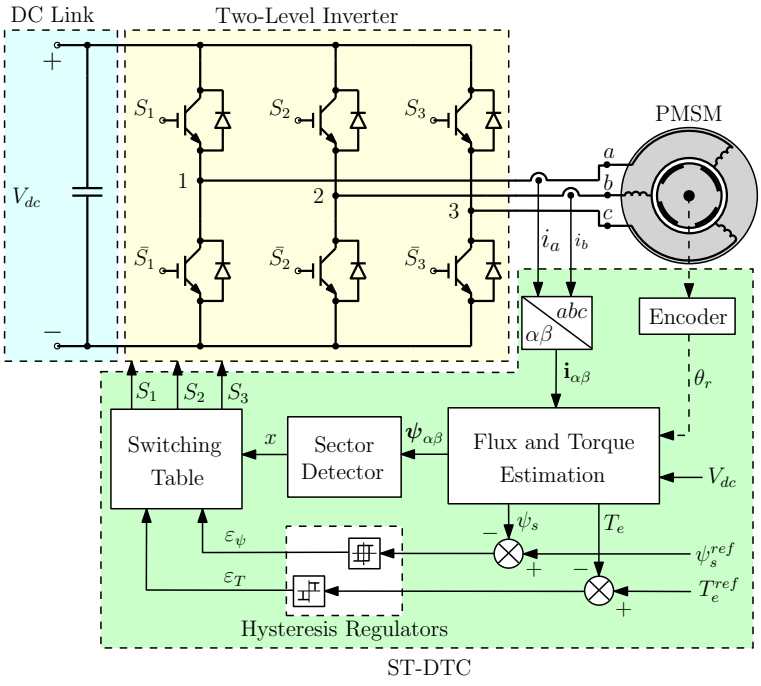

(b)

Figure 4.1: (a) Space-vector representation of the inverter voltage vectors with an example of their impact on the torque and stator-flux amplitude. (b) Schematic of ST-DTC for two-level inverter-fed PMSM.

xth sector, if θ_s satisfies the following condition:

$$\frac{(2x-3)\pi}{6} < \theta_s \leq \frac{(2x-1)\pi}{6} \tag{4.5}$$

where x is the sector number and $x \in \{1, 2, .., 6\}$.

As illustrated by Fig. 4.1(a), when $\boldsymbol{\psi}_{\alpha\beta}$ is situated in the 2nd sector $\pi/6 \leq \theta_s < 3\pi/6$), $\mathbf{V}_3$ increases both torque and stator flux, $\mathbf{V}_1$ decreases torque and increases stator flux, $\mathbf{V}_4$ increases torque and decreases stator flux, and $\mathbf{V}_6$ decreases both the torque and the stator flux. Generally, if $\boldsymbol{\psi}_{\alpha\beta}$ is located in the xth sector, similar control actions can be achieved by $\mathbf{V}_{x+1}$, $\mathbf{V}_{x+5}$, $\mathbf{V}_{x+2}$, and $\mathbf{V}_{x+4}$,[1] respectively. On the other hand, ZVVs are considered to have a negligible effect on the torque.

Consequently, the basic switching table (BST), presented in Table 4.1, is employed to select the voltage vector depending on the sector number (x) and the output states of the torque-and flux-hysteresis regulators (ε_T and ε_ψ), as shown in Fig. 4.1(b). The output of the hysteresis regulators indicate the required deviation direction in the estimated torque T_e and stator-flux amplitude ψ_s to track predefined reference signals (T_e^{ref} and ψ_s^{ref}), such that 1, 0, and -1 respectively represent increasing, maintaining, and decreasing the value of either T_e or ψ_s. BST employs a two-level flux-hysteresis regulator and a three-level torque-hysteresis regulator. As depicted in Fig. 4.2, the output of the flux hysteresis regulator changes

[1] If the voltage index $(x+n) > 6$, then $(x+n) = (x+n-6)$.

Table 4.1: The basic switching table (BST).

x *	$\varepsilon_T = 1$	$\varepsilon_T = 0$	$\varepsilon_T = -1$
$\varepsilon_\psi = 1$	$\mathbf{V}_{x+1}$	ZVV	$\mathbf{V}_{x+5}$
$\varepsilon_\psi = -1$	$\mathbf{V}_{x+2}$	ZVV	$\mathbf{V}_{x+4}$

* The sector index x is detected by using (4.5).

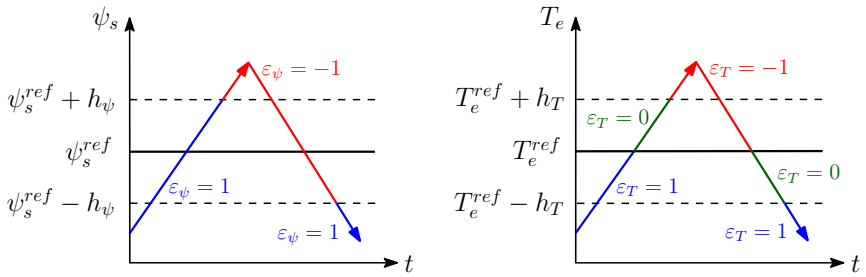

(a) (b)

Figure 4.2: Hysteresis regulators' output with changing torque and flux. (a) Flux regulator. (b) Toruqe regulator.

only when ψ_s crosses the flux-hysteresis limits ($\psi_s^{ref} \pm h_\psi$), while that of the torque regulator changes when T_e hits either the reference T_e^{ref} or the torque-hysteresis limits ($T_e^{ref} \pm h_T$) [28].

4.3 Analysis of Torque and Flux Responses

To identify the factors that affect the torque and flux responses, expressions for the torque and flux deviations are first introduced. The torque can be obtained from the cross product of the stator-flux and -current vectors as,

$$T_e = \frac{3p}{2} \left(\boldsymbol{\psi}_{\alpha\beta} \times \mathbf{i}_{\alpha\beta} \right), \tag{4.6}$$

and the stator-current vector can be determined from (3.4) as,

$$\mathbf{i}_{\alpha\beta} = \frac{1}{L_s} \left(\boldsymbol{\psi}_{\alpha\beta} - \boldsymbol{\psi}_r \right), \tag{4.7}$$

where ($\boldsymbol{\psi}_r = \psi_{pm} e^{j\theta_r}$) denotes the rotor-flux vector. Substituting (4.7) into (4.6), the time derivative of the torque can be written as,

$$\frac{\mathrm{d}T_e}{\mathrm{d}t} = \frac{3p}{2L_s} \left(\boldsymbol{\psi}_r \times \frac{\mathrm{d}\boldsymbol{\psi}_{\alpha\beta}}{\mathrm{d}t} - \boldsymbol{\psi}_{\alpha\beta} \times \frac{\mathrm{d}\boldsymbol{\psi}_r}{\mathrm{d}t} \right). \tag{4.8}$$

Based on (3.2) and (4.7), the stator-flux time derivative ($\mathrm{d}\boldsymbol{\psi}_{\alpha\beta}/\mathrm{d}t$) in (4.8) can be replaced by ($\mathbf{v}_{\alpha\beta} - R_s\left(\boldsymbol{\psi}_{\alpha\beta} - \boldsymbol{\psi}_r\right)/L_s$), yielding

$$\frac{\mathrm{d}T_e}{\mathrm{d}t} = \frac{3p}{2L_s}\left[\boldsymbol{\psi}_r \times \mathbf{v}_{\alpha\beta} - \frac{R_s}{L_s}\left(\boldsymbol{\psi}_r \times \boldsymbol{\psi}_{\alpha\beta}\right) - \boldsymbol{\psi}_{\alpha\beta} \times j\omega_r\boldsymbol{\psi}_r\right]. \tag{4.9}$$

By discretizing (4.9), the torque deviation (ΔT_e) in one sampling period (T_s) can be represented as,

$$\Delta T_e = \frac{3p\psi_{pm}T_s}{2L_s}\left[v_\beta\cos\theta_r - v_\alpha\sin\theta_r - \psi_s\left(\frac{R_s}{L_s}\sin\delta + \omega_r\cos\delta\right)\right], \tag{4.10}$$

where ($\delta = \theta_s - \theta_r$) represents the load angle.

On the other hand, the variation rate of the stator-flux-vector amplitude can be written as,

$$\frac{\mathrm{d}\psi_s}{\mathrm{d}t} = \frac{1}{\psi_s}\left(\boldsymbol{\psi}_{\alpha\beta} \cdot \frac{\mathrm{d}\boldsymbol{\psi}_{\alpha\beta}}{\mathrm{d}t}\right). \tag{4.11}$$

Substituting (3.2) and (4.7) into (4.11), results

$$\frac{\mathrm{d}\psi_s}{\mathrm{d}t} = \frac{1}{\psi_s}\left[\boldsymbol{\psi}_{\alpha\beta} \cdot \mathbf{v}_{\alpha\beta} - \frac{R_s}{L_s}\left({\psi_s}^2 - \boldsymbol{\psi}_{\alpha\beta} \cdot \boldsymbol{\psi}_r\right)\right]. \tag{4.12}$$

By discretizing (4.12), the flux deviation ($\Delta\psi_s$) in one sampling period can be expressed as,

$$\Delta\psi_s = \frac{T_s}{\psi_s}\left(v_\alpha\psi_\alpha + v_\beta\psi_\beta\right) + \frac{R_sT_s}{L_s}\left(\psi_{pm}\cos\delta - \psi_s\right). \tag{4.13}$$

It is revealed by (4.10) and (4.13) that the torque and flux-amplitude deviations depend on:

1. The applied stator voltage $\mathbf{v}_{\alpha\beta}$ and its corresponding duty ratio.
2. The operating-speed and loading conditions (i.e., ω_r and δ).

3. The angular position of the stator-flux vector θ_s.

The applied stator voltage ($\mathbf{v}_{\alpha\beta} = v_\alpha + jv_\beta$) is the voltage vector selected from the switching table, which depends on the DC-link voltage (V_{dc}), as shown in Table 4.2. Since the AVVs are shifted from each other by an angle of $\pi/3$ rad, their impact on the torque and stator flux repeats when θ_s changes by that angle value. For example, if $\theta_s = 2\pi/3$ rad, the vectors $\mathbf{V}_4$, $\mathbf{V}_5$, and $\mathbf{V}_6$ will produce similar torque and flux-amplitude deviations to those generated by $\mathbf{V}_5$, $\mathbf{V}_6$, and $\mathbf{V}_1$, respectively, when $\theta_s = \pi$ rad. Hence, the AVV index can be expressed according to the sector identifier (x), as follows:

$$\mathbf{V}_i = \begin{cases} \mathbf{V}_{x+n}, & \text{if } (x+n) \leq 6 \\ \mathbf{V}_{x+n-6}, & \text{otherwise} \end{cases}, \; n \in \{0, 1, .., 5\} \tag{4.14}$$

Accordingly, the torque and flux deviations produced by each voltage vector (if applied for the entire sampling period) are calculated for the machine under test at different loading conditions and operating speeds when θ_s varies within the spatial range of sector x, as shown in Figs. 4.3 and 4.4.

Table 4.2: The feasible voltage vectors of the 2L-VSI.

$\mathbf{V}_i$		Switching states			Voltage vector
		S_1	S_2	S_3	$\mathbf{v}_{\alpha\beta} = v_\alpha + jv_\beta$
ZVVs	$\mathbf{V}_0$	0	0	0	0
	$\mathbf{V}_7$	1	1	1	0
AVVs	$\mathbf{V}_1$	1	0	0	$2V_{dc}/3$
	$\mathbf{V}_2$	1	1	0	$V_{dc}/3 + j\sqrt{3}V_{dc}/3$
	$\mathbf{V}_3$	0	1	0	$-V_{dc}/3 + j\sqrt{3}V_{dc}/3$
	$\mathbf{V}_4$	0	1	1	$-2V_{dc}/3$
	$\mathbf{V}_5$	0	0	1	$-V_{dc}/3 - j\sqrt{3}V_{dc}/3$
	$\mathbf{V}_6$	1	0	1	$V_{dc}/3 - j\sqrt{3}V_{dc}/3$

For these calculations, the sampling period is arbitrarily set to 50 μs, and the SPMSM parameters (given in Table 3.2) are substituted into (4.10) and (4.13). In these equations, the stator-flux amplitude ψ_s can be obtained based on the torque demand using the maximum torque per ampere (MTPA) principle as,

$$\psi_s = \sqrt{{\psi_{pm}}^2 + \left(\frac{2L_sT_e}{3p\psi_{pm}}\right)^2}, \tag{4.15}$$

while the load angle δ is determined using (4.2), as follows:

$$\delta = \arcsin\left(\frac{2L_sT_e}{3p\psi_{pm}\psi_s}\right). \tag{4.16}$$

From (4.16), the rotor angle θ_r can be calculated as,

$$\theta_r = \theta_s - \delta. \tag{4.17}$$

In Figs. 4.3, the values of torque deviation are illustrated by different colors. It can be noticed that the operating speed has a great impact on the torque deviations compared to that of the load torque.

From Figs. 4.3(a) and 4.3(b), it can be noted that $\mathbf{V}_{x+1}$ and $\mathbf{V}_{x+5}$ produce reversed torque deviations. $\mathbf{V}_{x+1}$ always gives positive torque deviations that weaken and strengthen with the increase of positive and negative speed, respectively. Conversely, $\mathbf{V}_{x+5}$ always produces negative torque deviations that increase and decay with the rise of positive and negative velocity, respectively. The same can be stated for $\mathbf{V}_{x+2}$ and $\mathbf{V}_{x+4}$, but their torque deviations change the direction under high-speed and loading conditions, as shown in Figs. 4.3(c) and 4.3(d). The vectors $\mathbf{V}_x$ and $\mathbf{V}_{x+3}$ have ambiguous impact on the torque within each sector, as can be seen in Figs. 4.3(e) and 4.3(f). Consequently, they are not employed in the

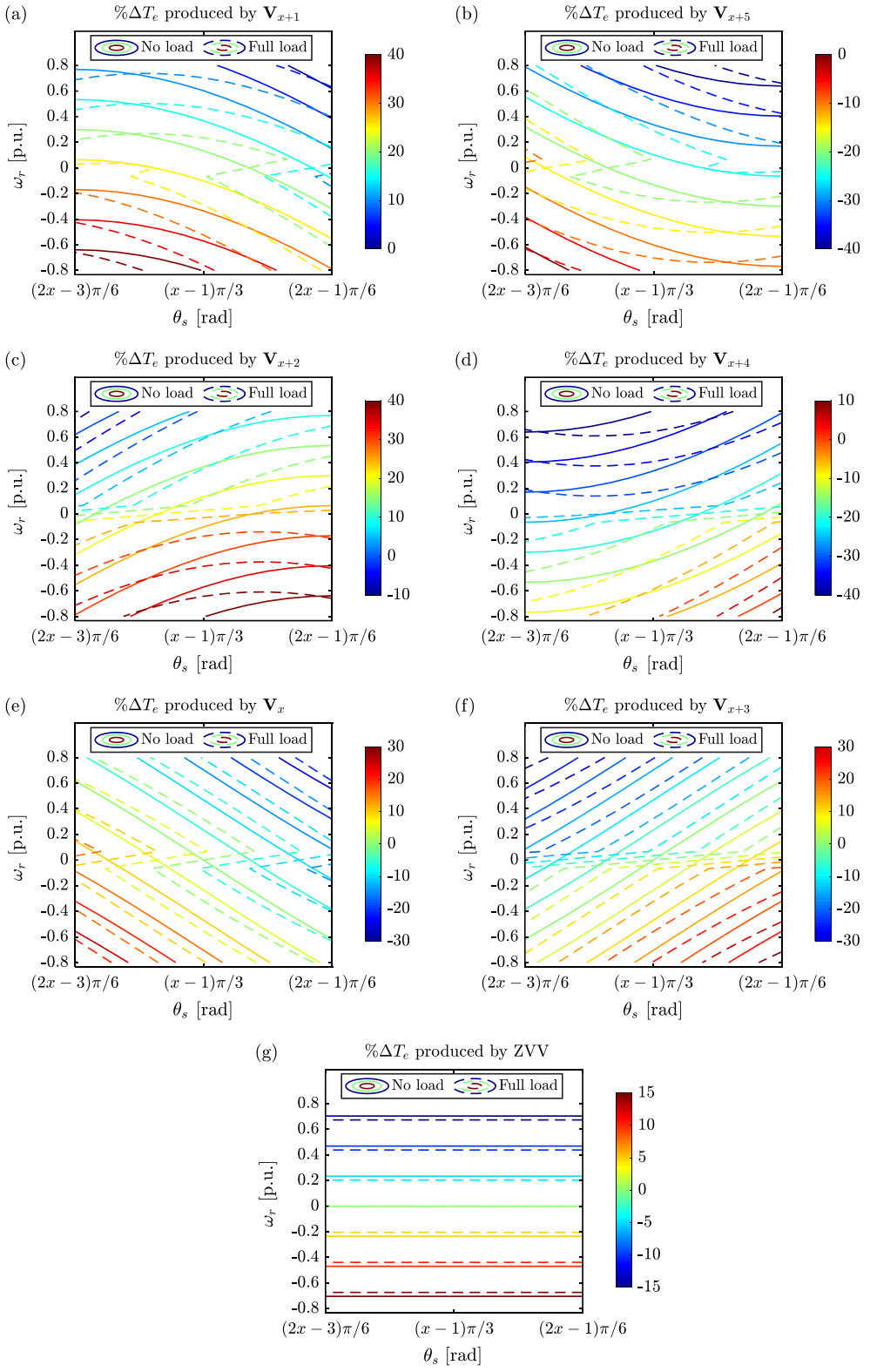

Figure 4.3: Percentage torque deviations produced by each voltage vector at different operating conditions and sampling period of 50 μs when θ_s is varied by the spatial range of sector x. (a) $\mathbf{V}_{x+1}$. (b) $\mathbf{V}_{x+5}$. (c) $\mathbf{V}_{x+2}$. (d) $\mathbf{V}_{x+4}$. (e) $\mathbf{V}_{x}$. (f) $\mathbf{V}_{x+3}$. (g) ZVV.

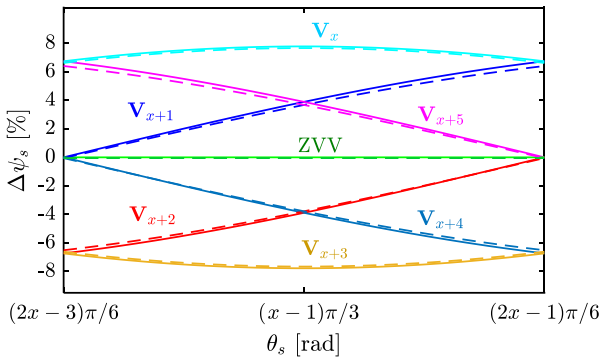

Figure 4.4: Percentage stator-flux deviations produced by each voltage vector at different loading conditions and sampling period of 50 μs when θ_s is varied by the spatial range of sector x. [solid line: no load; dashed line: full load].

conventional switching table (Table 4.1). On the other hand, as shown in Fig. 4.3(g), the ZVVs always decrease the absolute value of the torque with lower rates than those produced by $\mathbf{V}_{x+4}$ and $\mathbf{V}_{x+5}$ for positive speed and $\mathbf{V}_{x+1}$ and $\mathbf{V}_{x+2}$ for negative speed.

Because the stator-flux deviation is independent of the operating speed, according to (4.13), Fig. 4.4 illustrates how it is affected by the applied voltage vectors under different loading conditions. It can be noticed that increasing the load torque hardly changes the flux deviations for all voltage vectors. According to the previous discussion, the impact of the voltage vector selection strategies of different switching tables on the ST-DTC performance will be assessed in the following section to reveal the pros and cons of each switching table.

4.4 Switching Tables Assessment

4.4.1 Description of Modified Switching Tables

Different switching tables are utilized in ST-DTC of PMSM, which vary in terms of the definition of the sector boundaries, the number of levels of the

Table 4.3: The modified basic switching table (MBST).

x †	$\varepsilon_T = 1$	$\varepsilon_T = 0$	$\varepsilon_T = -1$
$\varepsilon_\psi = 1$	$\mathbf{V}_{x+1}$	ZVV	$\mathbf{V}_x$
$\varepsilon_\psi = -1$	$\mathbf{V}_{x+3}$	ZVV	$\mathbf{V}_{x+4}$

† The sector index x is detected by (4.18).

torque hysteresis controller, and the inclusion of ZVVs.

For the aim of torque-ripple reduction, the modified basic switching table (MBST), presented in Table 4.3, was developed in [84]. It follows the same conditions of BST, but the AVVs are selected based on modified sector boundaries that become on the six AVVs themselves, instead of the traditional boundaries shown in Fig. 4.1(a). The modified sectors can be defined as,

$$Sector\ x: \quad \frac{(2x-2)\,\pi}{6} < \theta_s \leq \frac{2x\pi}{6}. \tag{4.18}$$

Hence, the voltage vectors $\mathbf{V}_{x+5}$ and $\mathbf{V}_{x+2}$ used in BST at the table states "$\varepsilon_\psi = 1,\ \varepsilon_T = -1$" and "$\varepsilon_\psi = -1,\ \varepsilon_T = 1$" are replaced in MBST by $\mathbf{V}_x$ and $\mathbf{V}_{x+3}$, respectively, to avoid their ambiguous effect on the stator-flux amplitude.

Other studies, such as [50], show that ST-DTC of PMSM can work well only when the ZVVs are removed from the switching table by replacing the three-level hysteresis torque regulator with a two-level regulator, resulting in the switching table AST that only includes the AVVs, as presented in Table 4.4. The reason for that is the reduction of ψ_s due to the stator resistance drop when a ZVV is applied, according to (3.2). As a result, the stator flux will behave in a way that contradicts what is practically needed at the state "$\varepsilon_T = 0,\ \varepsilon_\psi = 1$" of either BST or MBST.

In contrast to the previous viewpoint, the rule of ZVVs in ST-DTC of

Table 4.4: The switching table with AVVs only (AST).

x ‡	$\varepsilon_T = 1$	$\varepsilon_T = -1$
$\varepsilon_\psi = 1$	$\mathbf{V}_{x+1}$	$\mathbf{V}_{x+5}$
$\varepsilon_\psi = -1$	$\mathbf{V}_{x+2}$	$\mathbf{V}_{x+4}$

‡ The sector index x is detected by (4.5).

Table 4.5: The switching table with a ZVV (ZST).

x ▲	$\varepsilon_T = 1$	$\varepsilon_T = -1$
$\varepsilon_\psi = 1$	$\mathbf{V}_{x+1}$	$\mathbf{V}_{x+5}$
$\varepsilon_\psi = -1$	$\mathbf{V}_{x+2}$	ZVV

▲ The sector index x is detected by (4.5).

PMSM has been investigated in [52], showing that the inclusion of ZVVs in the switching table can improve the steady-state control performance. Consequently, the switching table ZST (Table 4.5) was proposed in [85], where the torque needs a two-level hysteresis controller, and a ZVV is employed when both the torque and stator-flux amplitude are required to decrease (i.e., $\varepsilon_T = -1$ and $\varepsilon_\psi = -1$).

Owing to the inconsistent viewpoints for the voltage-vector selection employed in above mentioned switching tables, a comparative evaluation for them can be useful to identify their main features and drawbacks.

4.4.2 Evaluation of Voltage-Vector Selection Criteria

Because the selected voltage vector is applied for the entire control period in ST-DTC, the lower the torque and stator flux deviations produced by the selected voltage vector, the better the steady-state behavior and the slower the dynamic response that the system can achieve and vice versa. To assess the voltage-vector selection of each switching table, the values of the torque and stator-flux deviations within the sector x (presented in

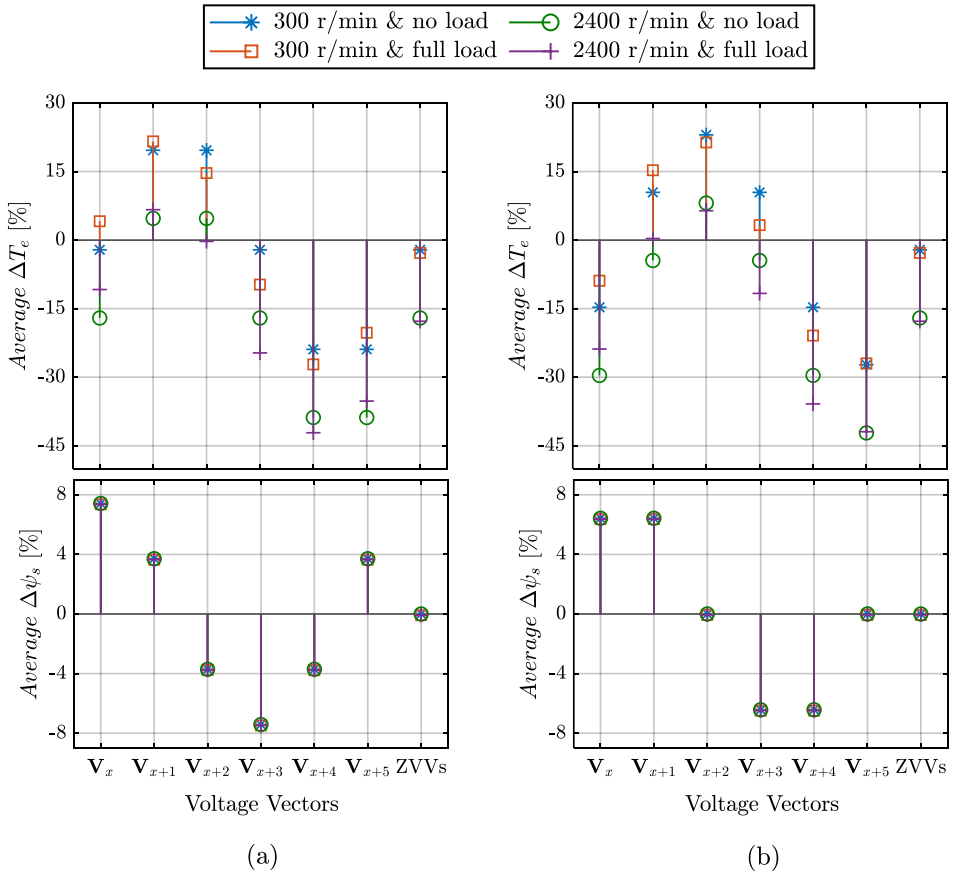

Figure 4.5: Average torque and stator flux deviations, in percentage of the rated values, produced by each voltage vector at different operating conditions, forward-rotation direction, and sampling period of 50 μs. (a) with the traditional sector boundaries. (b) with the modified boundaries.

Figs. 4.3 and 4.4) for each voltage vector are averaged at four different operating conditions, as illustrated by Fig. 4.5. Fig. 4.5(a) represents the averaged deviations within the traditional sector defined by (4.5), while Fig. 4.5(b) depicts them for the modified sector definition (4.18) utilized in MBST.

It can be observed in Fig. 4.5(a) that $\mathbf{V}_{x+1}$ and $\mathbf{V}_{x+2}$ are the only available options to increase the torque in sector x under all operating conditions. Therefore, employing $\mathbf{V}_{x+1}$ for the state "$\varepsilon_T = 1,\ \varepsilon_\psi = 1$" and $\mathbf{V}_{x+2}$ for the state "$\varepsilon_T = 1,\ \varepsilon_\psi = -1$" are the optimal solutions for BST, AST, and ZST. Moreover, both $\mathbf{V}_x$ and $\mathbf{V}_{x+5}$ can provide negative

torque deviation and positive stator-flux variation, but the latter is a better choice because of the conflicting torque behavior caused by $\mathbf{V}_x$, especially at low-speed and high-loading conditions. Thus, selecting $\mathbf{V}_{x+5}$ for the state "$\varepsilon_T = -1,\ \varepsilon_\psi = 1$" in BST, AST, and ZST is a feasible option.

Because ZVVs produce negligible deviations in the stator flux, they are acceptable to be used at the states where $\varepsilon_T = 0$ in BST and MBST. However, they are more efficiently employed in ZST for the state "$\varepsilon_T = -1,\ \varepsilon_\psi = -1$" because of their negative torque deviations. Additionally, utilizing ZVVs at this state, instead of $\mathbf{V}_{x+4}$ (utilized in BST and AST), can reduce the steady-state ripples, because ZVVs cause lower torque and stator flux deviations than $\mathbf{V}_{x+4}$, as shown in Fig. 4.5(a). On the other hand, for the same reason, this will impair the dynamic response when ZST is employed in ST-DTC if a torque decrease is demanded. Furthermore, during speed reversal, the torque-deviation rate of ZVVs becomes positive, as discussed in Section 4.3. Thus, selecting a ZVV when $\varepsilon_T = -1$ in ZST while reversing the direction of rotation will cause system instability. Instead, ZVV and $\mathbf{V}_{x+4}$ are superior choices to be employed during speed reversal at the states "$\varepsilon_T = 1,\ \varepsilon_\psi = 1$" and "$\varepsilon_T = -1,\ \varepsilon_\psi = -1$", respectively.

With the modified sector boundaries, it can be noted from Fig. 4.5(b) that all AVVs employed in MBST, i.e., $\mathbf{V}_{x+1}$, $\mathbf{V}_x$, $\mathbf{V}_{x+3}$, and $\mathbf{V}_{x+4}$, provide lower torque deviations and higher stator-flux deviations compared with those used in BST, i.e., $\mathbf{V}_{x+1}$, $\mathbf{V}_{x+5}$, $\mathbf{V}_{x+2}$, and $\mathbf{V}_{x+4}$, respectively (see Fig. 4.5(a)). As a result, MBST can provide lower torque ripple at low speed (300 r/min), and higher stator-flux ripple than BST. Additionally, both $\mathbf{V}_{x+3}$ and $\mathbf{V}_{x+1}$ fail to increase the torque, especially at high speed (2400 r/min), which weakens the effectiveness of voltage-vector selection based on the modified sector boundaries.

According to the analysis mentioned above, the voltage vectors are more efficiently selected in ZST for steady-state operation, but it does not allow reversing the rotational direction. On the other hand, employing AST will be more efficient during system transients. Hence, a flexible switching table is proposed in the following section to select the most feasible voltage vector according to the operating conditions.

4.5 Performance Enhancement of ST-DTC Based on a Flexible Switching Table

In this section, a flexible-switching table (FST) for DTC of PMSM is proposed to reduce the torque and flux ripples, while maintaining the fast dynamic response and ease of implementation of the conventional method. It uses a simple algorithm to adaptively select a proper voltage vector for different states of the switching table based on the system operating condition. To verify the feasibility and effectiveness of the proposed approach, the ST-DTC performances using FST and the switching tables analysed in 4.4.2 are compared by means of simulation and experimental results.

4.5.1 Basic Principle of FST

As discussed in 4.3, the voltage vectors included in the switching table produce different rates of torque and flux deviations that depend not only on the angular position of the stator-flux vector but also operating conditions, such as the direction of rotation. Hence, selecting the voltage vector using a switching table that changes the structure flexibly based on these conditions is a desired feature from the point of view of steady-state and

dynamic performances.

From the analysis presented in 4.4.2, when the motor speed is positive, applying a ZVV at the states where "$\varepsilon_T = -1$" instead of the AVVs ($\mathbf{V}_{x+4}$ or $\mathbf{V}_{x+5}$) can improve the steady-state performance in terms of the torque and flux ripples for two reasons:

1. ZVVs produce lower negative torque deviations than $\mathbf{V}_{x+4}$ and $\mathbf{V}_{x+5}$.
2. the impact of ZVVs on the flux is negligible.

When the machine runs in the reverse direction, ZVVs produce positive deviations in the torque, the values of which is lower than those generated by $\mathbf{V}_{x+1}$ and $\mathbf{V}_{x+2}$ (see Fig. 4.3). Therefore, to maintain the steady-state-performance improvement in the backward direction of rotation, ZVVs are employed at the states where "$\varepsilon_T = 1$" instead of the AVVs ($\mathbf{V}_{x+1}$ or $\mathbf{V}_{x+2}$). However, these will cause two issues for the dynamic performance of ST-DTC, which can be listed as follows:

1. slow torque response when a torque reduction is commanded.
2. instability during speed reversal because the direction of the torque deviation produced by ZVV depends on the rotation direction, as can be noticed in Fig. 4.3(g).

To avoid these two issues, the FST employs AVVs at all the table states (as in AST) during system dynamics.

Table 4.6 presents the proposed FST, where the voltage vectors can be selected based on the following factors:

- The sign of the error signal of torque and stator-flux amplitude (T_{err} and ψ_{err}).
- The system operating state (steady state or dynamic).

Table 4.6: Proposed flexible switching table (FST).

Error Signals of Torque and Flux		**Steady State**		**Dynamic State**
T_{err}	ψ_{err}	↻	↺	
$T_{err} \geq 0$	$\psi_{err} \geq 0$	$\mathbf{V}_{x+1}$	ZVV	$\mathbf{V}_{x+1}$
	$\psi_{err} < 0$	$\mathbf{V}_{x+2}$	ZVV	$\mathbf{V}_{x+2}$
$T_{err} < 0$	$\psi_{err} \geq 0$	ZVV	$\mathbf{V}_{x+5}$	$\mathbf{V}_{x+5}$
	$\psi_{err} < 0$	ZVV	$\mathbf{V}_{x+4}$	$\mathbf{V}_{x+4}$

- The direction of rotation (forward ↻ or backward ↺).

In the proposed FST, the sign of the error signals (T_{err} and ψ_{err}) can be used instead of the hysteresis regulators (ε_T and ε_ψ) for voltage-vector selection, simplifying the control implementation. Additionally, the voltage vector is artificially selected according to the operating state and the direction of rotation to guarantee employing the one that produces low torque deviation during steady state to minimize the torque ripple. Meanwhile, FST allows selection of the AVV with high torque deviation under system dynamics to ensure fast transient response.

4.5.2 Reduction of Stator-Flux Ripple and Average Switching Frequency

According to FST, one of two AVVs will be applied under steady-state conditions depending on the rotation direction ($\mathbf{V}_{x+1}$ or $\mathbf{V}_{x+2}$ for clockwise, and $\mathbf{V}_{x+5}$ or $\mathbf{V}_{x+4}$ for anticlockwise). From Fig. 4.4, when θ_s is in the range of $[\frac{(2x-3)\pi}{6}, \frac{(2x-3)\pi}{6} + \frac{\pi}{12})$, the absolute flux deviations produced by $\mathbf{V}_{x+2}$ and $\mathbf{V}_{x+5}$ are relatively higher than those generated by $\mathbf{V}_{x+1}$ and $\mathbf{V}_{x+4}$, respectively. Conversely, $\mathbf{V}_{x+1}$ and $\mathbf{V}_{x+4}$ give higher absolute flux

deviations when θ_s is in the range of $(\frac{(2x-1)\pi}{6} - \frac{\pi}{12}, \frac{(2x-1)\pi}{6}]$. Hence, a voltage-replacement strategy is proposed to avoid the large flux deviations and reduce the flux ripple.

In the voltage-replacement strategy, the position of the stator-flux vector within sector x is first checked using the following subsector definition:

$$\begin{cases} \textit{Subsector I}: \ \frac{(2x-3)\pi}{6} < \theta_s \leq \frac{(2x-3)\pi}{6} + \sigma \\ \textit{Subsector II}: \ \frac{(2x-1)\pi}{6} - \sigma < \theta_s \leq \frac{(2x-1)\pi}{6}, \end{cases} \tag{4.19}$$

where $\sigma \in \left[0, \frac{\pi}{12}\right]$ is the angular range of the subsector. Then, the voltage vector selected from FST is replaced according to the following conditions:

$$\textbf{If} \ \ \theta_s \in \textit{Subsector I}, \ \textbf{then} \begin{cases} \text{Replace } \mathbf{V}_{x+2} \text{ with } \mathbf{V}_{x+1} \\ \text{Replace } \mathbf{V}_{x+5} \text{ with } \mathbf{V}_{x+4} \end{cases} \tag{4.20}$$

$$\textbf{If} \ \ \theta_s \in \textit{Subsector II}, \ \textbf{then} \begin{cases} \text{Replace } \mathbf{V}_{x+1} \text{ with } \mathbf{V}_{x+2} \\ \text{Replace } \mathbf{V}_{x+4} \text{ with } \mathbf{V}_{x+5} \end{cases} \tag{4.21}$$

For further steady-state performance improvement, the switching frequency can be reduced by carrying out a trade-off between employing $\mathbf{V}_0$ or $\mathbf{V}_7$ when a ZVV is selected by the proposed FST. This is fulfilled by checking the selected voltage vector at the previous sampling instant; if it is either $\mathbf{V}_0$, $\mathbf{V}_1$, $\mathbf{V}_3$ or $\mathbf{V}_5$, the ZVV "$\mathbf{V}_0$" will be employed, while $\mathbf{V}_7$ will follow the other voltage vectors to minimize the number of switching jumps.

In this way, the voltage-vector-selection criteria of the proposed FST is more flexible than those of the conventional switching tables. In other words, FST takes changing forms according to the working conditions of the ST-DTC system. Hence, it can more efficiently exploit the benefits of

employing both AVVs and ZVVs in the ST-DTC compared to the switching tables analyzed in 4.4.2. Additionally, selection of the voltage vector based on the error signals of torque and flux simplifies the control implementation by omitting the need for hysteresis regulators and the corresponding tedious tuning of their boundaries.

4.5.3 Implementation Steps of the FST-based DTC Method

As shown in Table 4.6, the voltage vectors at different states of FST need to be flexibly selected depending on the system operating condition and the direction of rotation. These can be achieved using a simple voltage selection strategy, the flowchart of which is illustrated in Fig 4.6.

As illustrated by the flowchart in Fig. 4.6, the system operating state can be detected by the reference torque transition ($\Delta T_e^{ref}[k] = T_e^{ref} - T_e^{ref}[k-1]$) to avoid the usage of torque sensor that will increase the system cost and complexity. If any change in the demanded torque is detected ($\Delta T_e^{ref}[k] \neq 0$), AVVs will be activated for all states of the switching table to achieve fast torque response. This activation has to be kept until the estimated torque crosses the reference signal (i.e., $\text{sign}(T_{err}^k) \neq \text{sign}(T_{err}^{k-1})$), and the direction of rotation becomes the same as that of the reference torque ($T_e^{ref} \cdot \omega_r^k \geq 0$) to allow regenerative braking and speed reversal if required. Thus, maintaining the AVVs activation is ensured via a "$flag$" that will reset only when both of the aforementioned conditions are satisfied. On the other hand, if there is no torque transition detected ($\Delta T_e^{ref}[k] = 0$), which means that the system works under steady state, ZVVs will be activated at either the states where "$T_{err} \geq 0$" or "$T_{err} < 0$" based on the direction of rotation that can be detected by the position sensor.

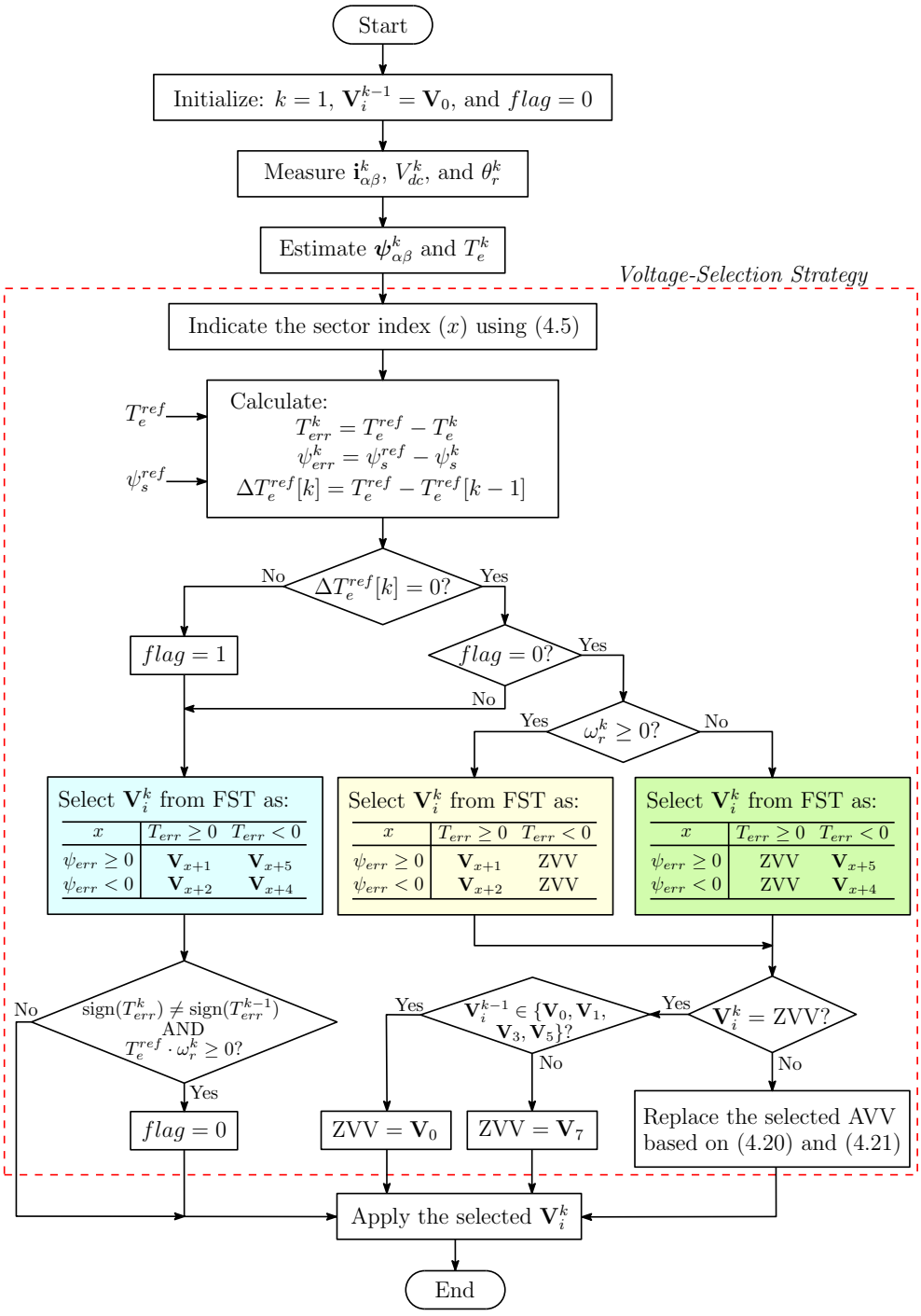

Figure 4.6: Flowchart of the proposed FST-based DTC method.

If the selected voltage vector from FST is a ZVV, either $\mathbf{V}_0$ or $\mathbf{V}_7$ is applied based on the vector chosen in the previous control cycle to reduce the average switching frequency. Otherwise, the selected AVV will be replaced only if the stator-flux vector is located in one of the subsectors defined by (4.19) to reduce the flux ripple. The effectiveness of the proposed FST and the voltage-selection strategy will be verified by the simulation and experimental results in Section 4.6.

4.6 Simulation and Experimental Results

The proposed FST-based DTC strategy has been validated through simulations and experimental tests on an IPMSM and SPMSM, respectively. Its overall performance has been compared with the conventional ST-DTC approaches that utilize BST, MBST, AST, and ZST. The control parameters for ST-DTC tests are given in Table 4.7.

4.6.1 Simulation Results

The steady-state performance of the ST-DTC strategies using different switching tables is tested and compared under different speed and load conditions. In Figs. 4.7 and 4.8, the demanded torque is set to 0 N·m and 400 N·m, respectively, and the speed is stepped up every 0.5 s.

Table 4.7: Control parameters of the ST-DTC approaches

Control parameters	**Values**	**Units**
Sampling frequency (f_s)	20	kHz
Torque-hysteresis band (h_T)	$\pm 2\%$ of T_{rated}	N·m
Flux-hysteresis band (h_ψ)	$\pm 2\%$ of ψ_{pm}	Wb

As can be noticed in these figures, the steady-state performance of the proposed FST-based DTC approach outperforms those of the other strategies in terms of the torque and flux ripples. From Fig. 4.7, AST-based DTC produces the largest torque ripple because it uses the AVVs only, showing the importance of the ZVV inclusion in the switching table. On the other hand, by modifying the sector boundaries, MBST can produce lower torque ripple than BST at the cost of increased flux ripple. Moreover, MBST causes unstable operation of the drive system at 3000 r/min speed due to the failure of both vectors $\mathbf{V}_{x+1}$ and $\mathbf{V}_{x+3}$ to increase the torque at high speeds (see Fig. 4.5). As for ZST-based DTC, the torque ripple is larger than that produced by BST-based DTC because the ZVV is less frequent used, while the flux ripple is slightly decreased. At rated torque (400 N·m), similar behavior can be noticed, but the ZST-based DTC generates lower torque ripple compared to BST, as shown in Fig. 4.8.

A detailed quantitative comparison in terms of the torque ripple (T_e^{rip}), flux ripple (ψ_s^{rip}), and average switching frequency (f_{av}) is given in Fig. 4.9. These performance indices presented in Figs. 4.9(a) and 4.9(b) are obtained from the simulated ST-DTC strategies at 0 N·m and 400 N·m, respectively, under different operating speeds.

According to Fig. 4.9(a), the proposed FST-DTC approach achieves the lowest torque ripple that is 17%, 3%, 52%, and 39% less than those of BST, MBST, AST, and ZST, respectively. Although its torque-ripple reduction is insignificant compared to MBST, the flux ripple is dramatically reduced by an average of 36% with 15% lower average commutation frequency. From Fig. 4.9(b), this torque-ripple reduction increases to 38%, on average, at full load with a significant decrease in the average switching frequency by an average of 56%. Moreover, compared to BST-, AST-, and ZST-based DTC methods, the proposed strategy provides the highest

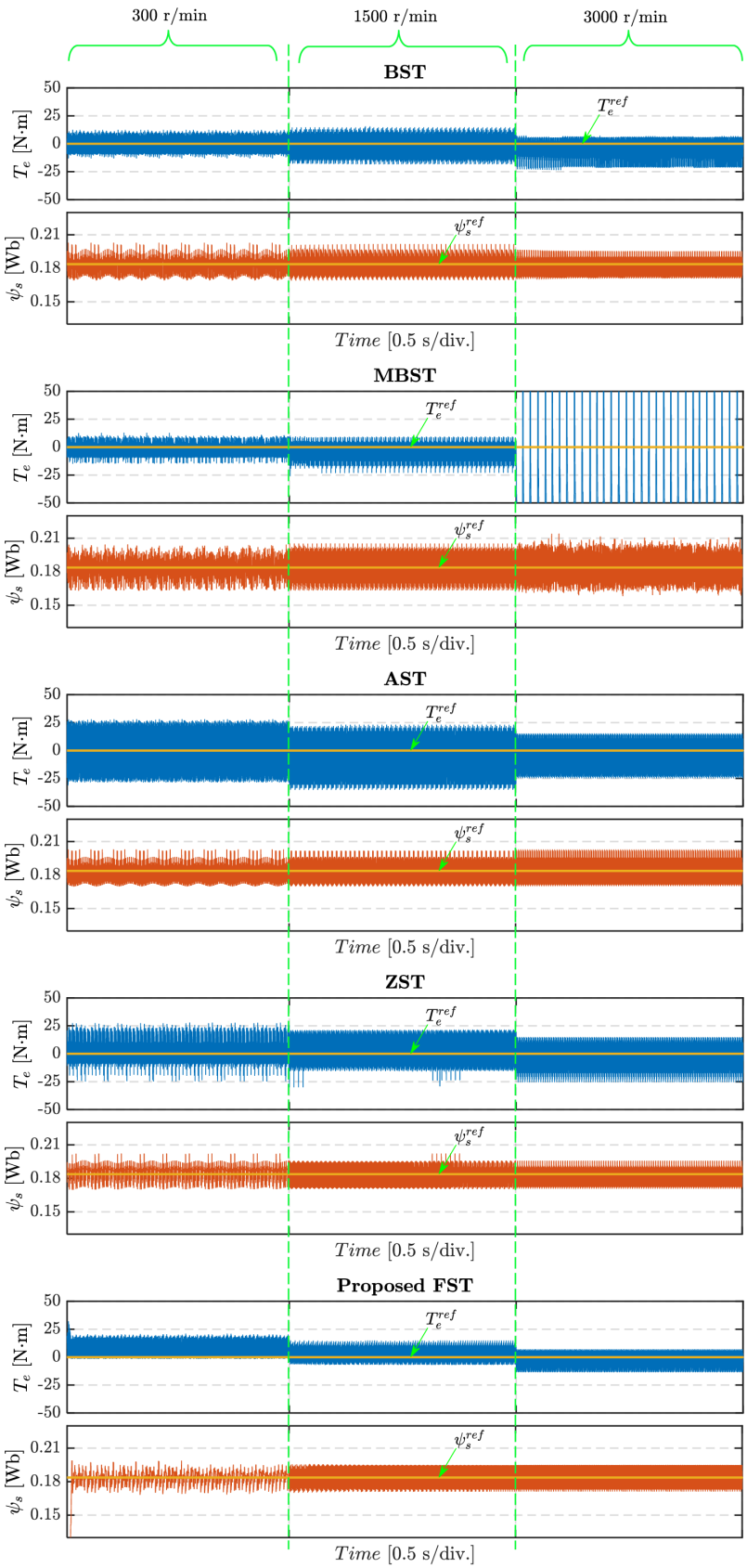

Figure 4.7: Simulation results of the torque and flux steady-state performances for ST-DTC strategies under no load and different operating speeds.

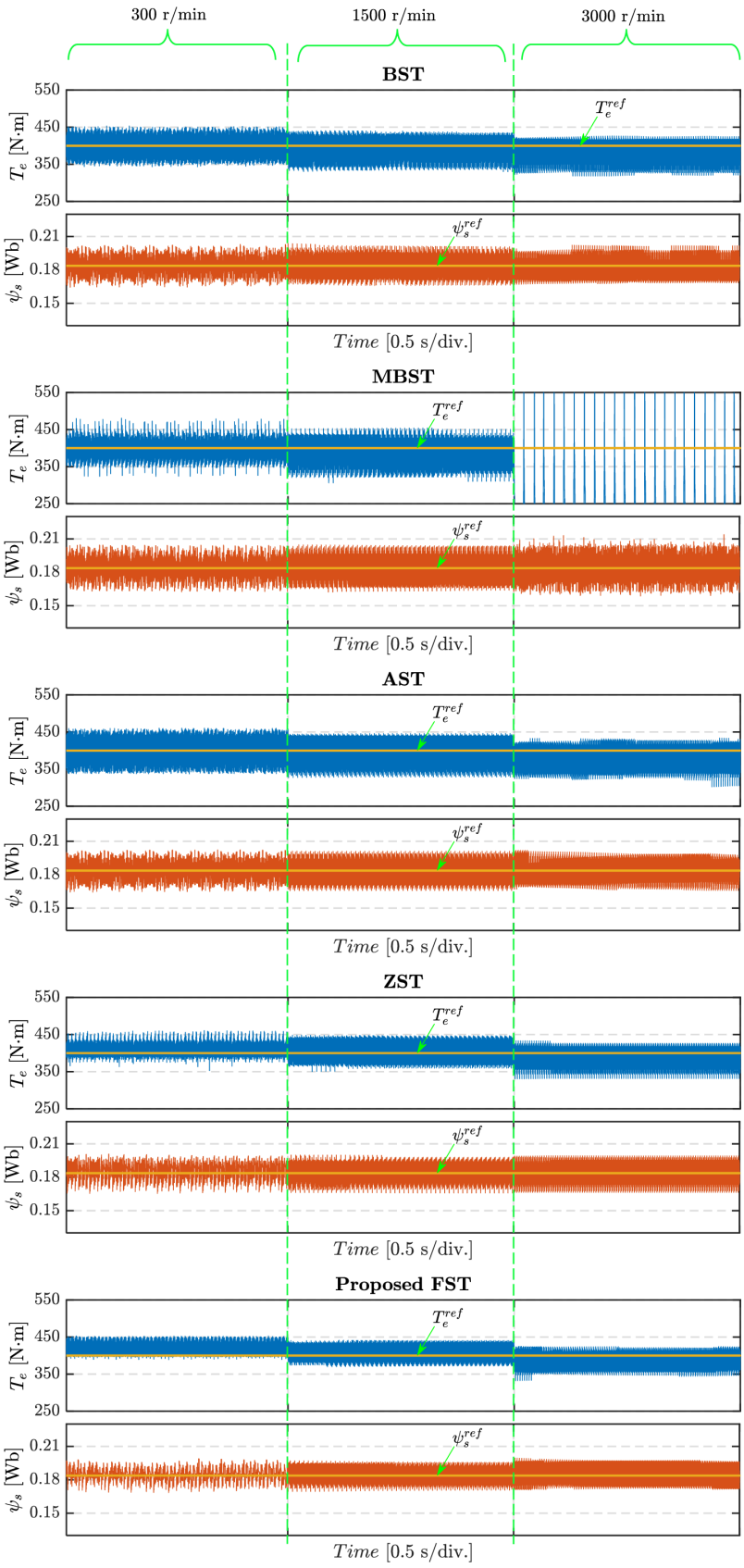

Figure 4.8: Simulation results of the torque and flux steady-state performances for ST-DTC strategies under full load and different operating speeds.

reduction in T_e^{rip}, ψ_s^{rip}, and f_{av} with an average of 30%, 18%, and 29%, respectively. These results verify the effectiveness of the proposed FST-based approach to improve the steady-state torque and flux performances of ST-DTC, while reducing the average switching frequency.

Apart from the steady-state performance, the dynamic response of the ST-DTC strategies is also investigated. Figs. 4.10(a) and 4.10(b) show the simulation results of the dynamic performance when the demanded torque is stepped up from 0 to 400 N·m and down from 400 to 0 N·m under different rotor speeds, 500 r/min and 3000 r/min. When the torque is

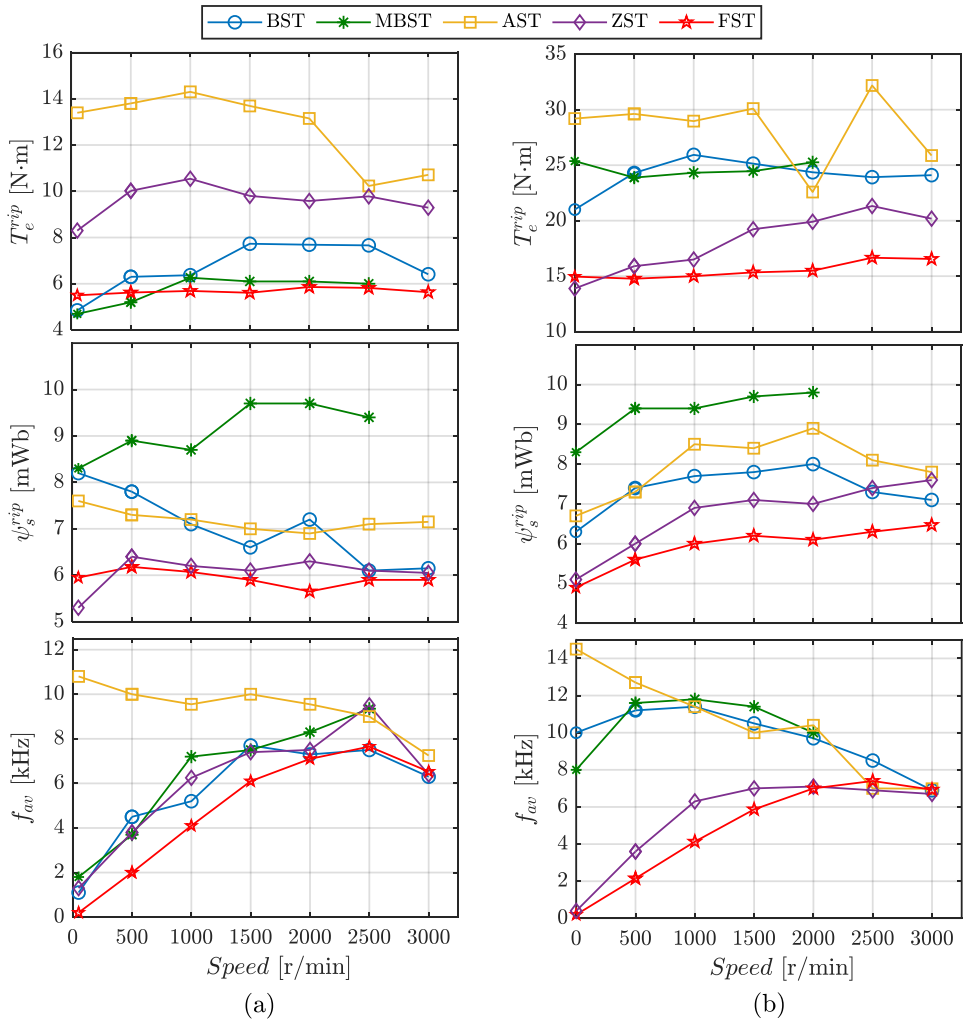

Figure 4.9: Quantitative comparison of the steady-state torque and flux performances for ST-DTC strategies at different operating speeds. (a) No load. (b) Full load. [Simulation results]

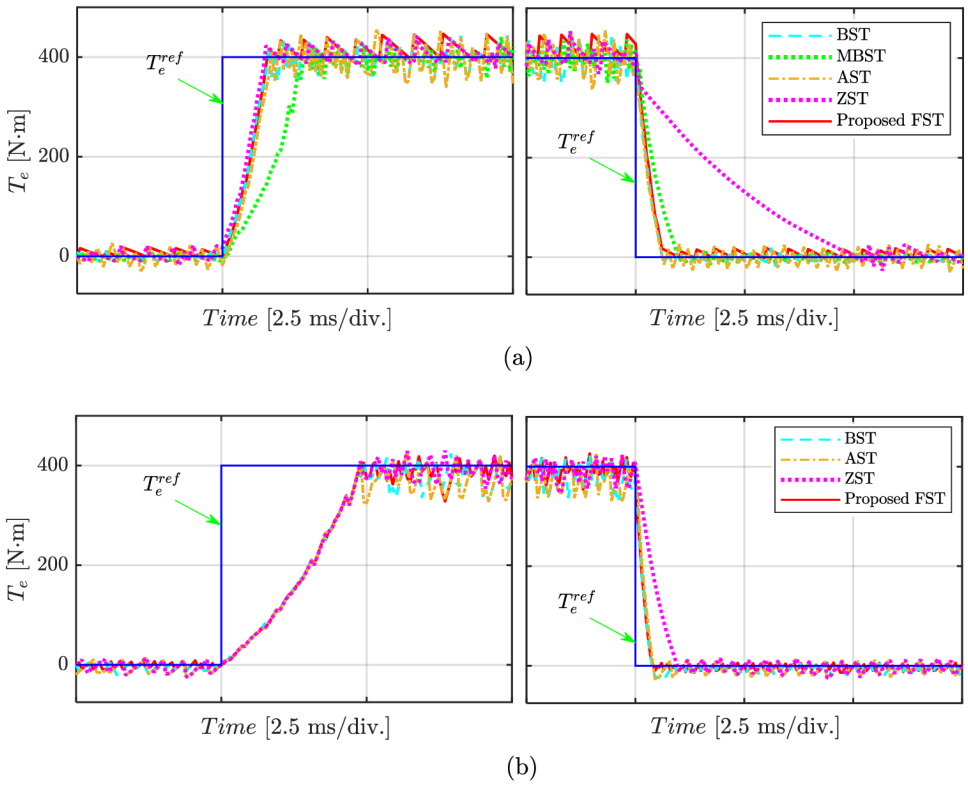

Figure 4.10: Simulation results of the torque dynamic response of ST-DTC strategies with 400 N·m step at different operating speeds. (a) 500 r/min. (b) 3000 r/min.

stepped up, it can be noticed that all the switching tables allow similar torque responses, excluding MBST that causes slower response. As can be inferred by Fig. 4.5, the reason of this slower response is that the AVVs employed by MBST to increase the torque (i.e., $\mathbf{V}_{x+1}$ and $\mathbf{V}_{x+3}$) produce lower torque deviation than $\mathbf{V}_{x+1}$ and $\mathbf{V}_{x+2}$ that are utilized in the other switching tables. It should be noted that the dynamic response of MBST-DTC is not depicted in Fig. 4.10(b) because of the unstable operation under high-speed condition. When the torque is stepped down, the dynamic response of ZST-DTC degrades significantly because of employing ZVV to decrease the torque. This issue is overcome in FST thanks to the proposed voltage-selection strategy that applies AVVs during transient conditions.

Furthermore, from Fig. 4.10, it can be seen that the torque response is faster during stepping down than that for stepping up as the $-$ve deviations

in torque is larger than the +ve deviations when ω_r is positive (see Fig. 4.3). Also, by comparing Fig. 4.10(a) with Fig. 4.10(b), it can be noted that the rising time increases with the speed increase, while the falling time decays because the +ve and −ve torque deviations produced by AVVs weaken and strengthen, respectively, with the speed rise. These simulation results conform the theoretical assessment of the switching tables presented in 4.4.2 and validates the effectiveness of the proposed FST-based approach to maintain the fast dynamic response of the conventional ST-DTC.

4.6.2 Experimental Results

Several experiments have been carried out on a laboratory prototype of a 0.75-kW SPMSM using dSPACE as a control platform (see Section 3.4). The DC-link voltage is set to 220 V, and the sampling frequency is maintained at 20 kHz, for consistency with the theoretical analysis in Section 4.3. For the sake of accuracy, the one-step delay due to digital implementation is compensated for all the ST-DTC strategies by selecting the voltage vector based on the predicted torque and flux (i.e., T_e^{k+1} and ψ_s^{k+1}) [93].

4.6.2.1 Steady-state performance comparison of the ST-DTC strategies

Figs. 4.11 and 4.12 show the experimental waveforms of electromagnetic torque, stator-flux amplitude, phase current, and index of the selected voltage vector for ST-DTC under different switching tables at 750 r/min and 2250 r/min, respectively. The load torque is set to around 1.8 N·m. The reference torque is generated using an outer PI-speed loop with gains of $K_P = 0.006843$ and $K_I = 0.78046$ to maintain the speed constant while

capturing the experimental waveforms by the ControlDesk. The reference stator-flux amplitude is obtained from the demanded torque based on the MTPA principle (4.15) to increase the system efficiency [82].

From Figs. 4.11 and 4.12, it can be observed that the application of BST and AST gives almost the same steady-state performance, and MBST causes lower torque ripple than them, while its flux ripple is higher. ZST improves both the torque and flux ripple of BST, AST, and MBST because of the more frequently employed ZVV, as can be seen in the vector-index waveform. Compared to ZST, the proposed FST-DTC method provides a significant torque-ripple reduction because it avoids selecting the AVVs that produce high torque deviations. Also, it reduces flux ripple by applying the voltage replacement strategy (i.e., when $\sigma = \pi/12$ rad).

Fig. 4.13 gives quantitative evaluation for the steady-state performances of the different ST-DTC strategies in terms of torque ripple, flux ripple, average switching frequency, and total harmonic distortion of the phase current. It can be noticed that the proposed FST-DTC method achieves the best overall steady-state performance.

According to Fig. 4.13, the application of MBST reduces the torque ripple only at low speed (750 r/min) compared to BST by about 6% with lower average switching frequency, but the stator flux ripple and the current distortion increase by 24% and 4%, respectively. The torque ripple of the proposed method is significantly lower than that of BST, MBST, AST, and ZST by averages of 46%, 44%, 48%, and 41%, respectively. As can be seen in Fig. 4.13(b), the proposed FST without voltage replacement can cause high flux ripple at lower average switching frequency. However, with the voltage replacement ($\sigma = \pi/12$ rad), the flux ripple can be notably reduced with further reduction in both the current distortions and the

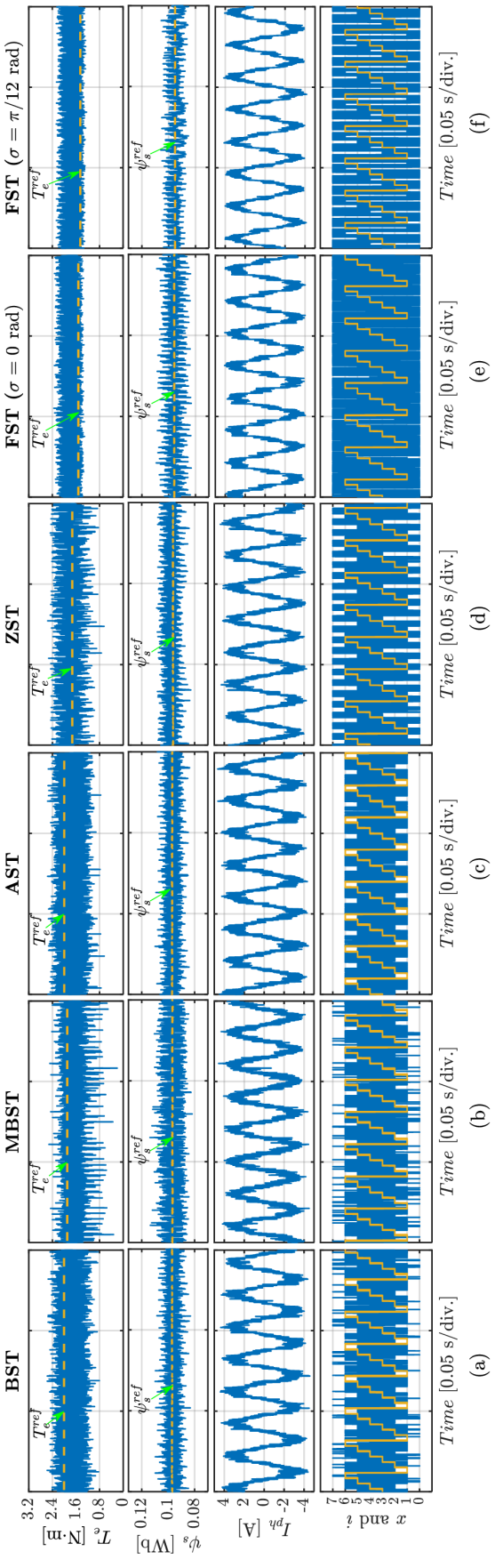

Figure 4.11: Experimental results of the steady-state performance for ST-DTC strategies under 1.8 N·m load and 750 r/min speed. (a) BST. (b) MBST. (c) AST. (d) ZST. (e) FST at $\sigma = 0$ rad. (f) FST at $\sigma = \pi/12$ rad. [The waveforms are (from top to bottom): torque, stator-flux amplitude, phase current, and the selected voltage vector index (i)]

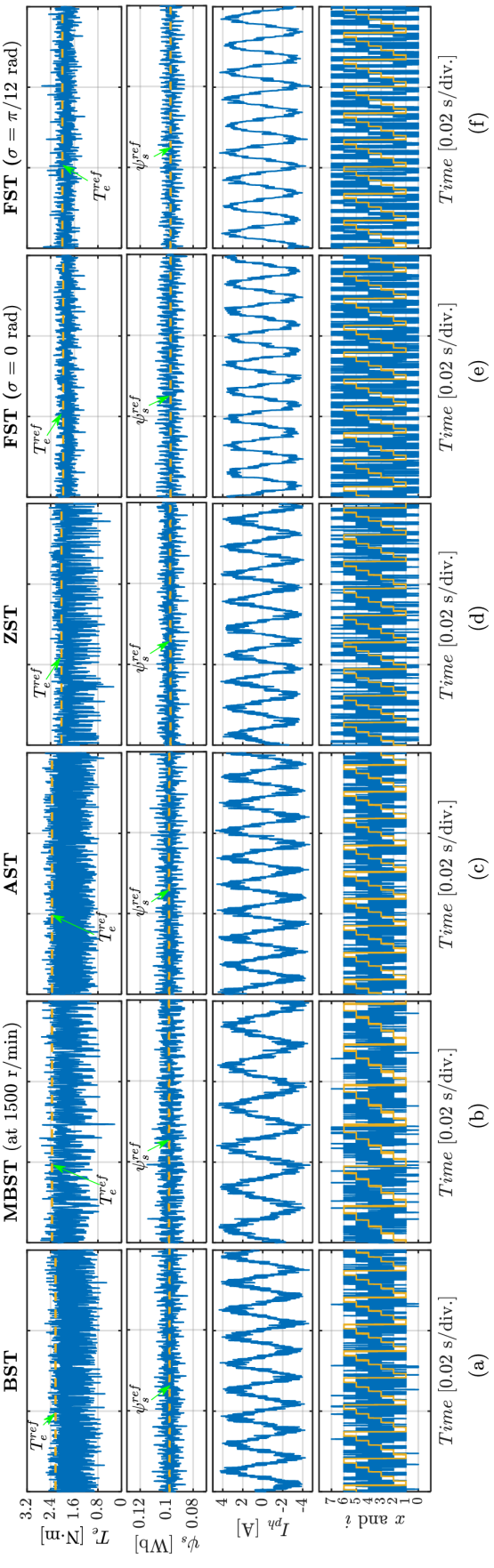

Figure 4.12: Experimental results of the steady-state performance for ST-DTC strategies under 1.8 N·m load and 2250 r/min speed. (a) BST. (b) MBST (at 1500 r/min). (c) AST. (d) ZST. (e) FST at $\sigma = 0$ rad. (f) FST at $\sigma = \pi/12$ rad. [The waveforms are (from top to bottom): torque, stator-flux amplitude, phase current, and the selected voltage vector index (i)]

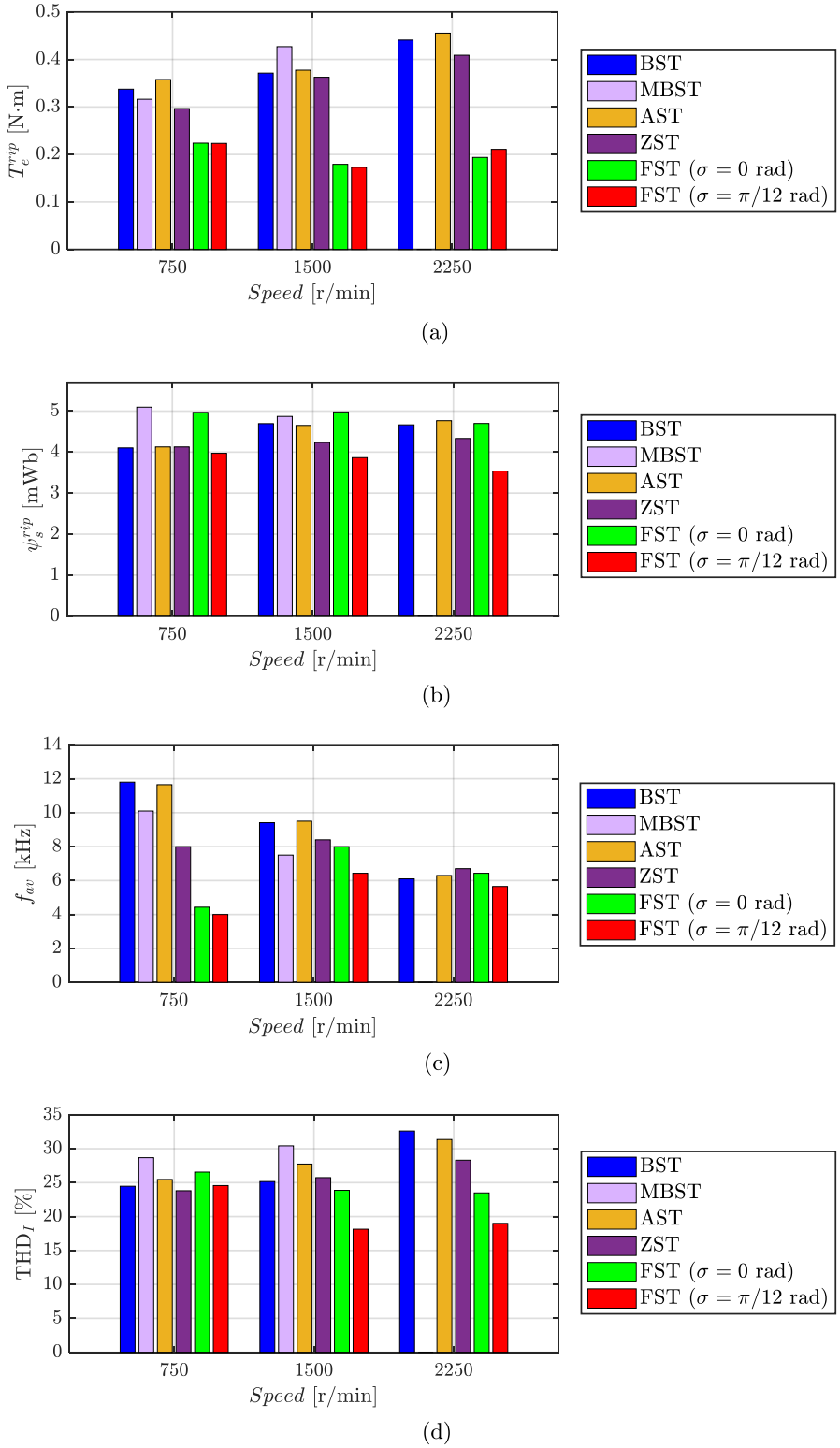

Figure 4.13: Quantitative evaluation of the steady-state performances for ST-DTC strategies under 1.8 N·m-load torque at different operating speeds. (a) Torque ripple. (b) Flux ripple. (c) Average switching frequency. (d) Total harmonic distortion of phase stator current. [Experimental results]

average switching frequency. The proposed FST-DTC achieves the lowest flux ripple, current distortions, and the average switching frequency that are respectively reduced by 16%, 19%, and, 37%, on average, compared with the other methods.

4.6.2.2 Dynamic performance comparison of the ST-DTC strategies

Apart from the steady-state performance experiments, the torque dynamic performances of the DTC system using the different tables have been also tested and compared in Fig. 4.14. In this experiment, the load torque is set to 1.6 Nm and the reference torque was stepped up from 0 to 2 N·m to test the torque response during start-up. Then, it was stepped down from 2 to −2 N·m once the speed reaches 1500 r/min to confirm the torque response at different operation modes, i.e., forward regenerative braking and backward motoring [see Fig. 3.9]. The corresponding speed response and phase current of the machine for that test scenario are presented to the bottom of the torque response. The zoomed zones ① and ② in Fig. 4.14 show the rise and fall time of the torque responses.

In Fig. 4.14, it can be seen that there are insignificant diferences between the torque rising time provided by BST, AST, ZST, and the proposed FST (about 0.2 ms). However, it is slightly longer in case of MBST (almost 0.27 ms) because the AVVs produce lower torque deviation with the modified sector boundaries than that with the traditional sector boundaries. When the reference torque decreased from 2 to −2 N·m, all the switching tables achieve almost the same torque falling time (0.27 ms) except ZST, the torque response of which took nearly 0.55 ms to reach the reference value. Additionally, the DTC that employs ZST causes system instability

when the speed dropped to zero during speed reversal, as can be noticed in Fig. 4.14(d), because the torque deviation provided by ZVVs reverses as mentioned in Section 4.3. Conversely, FST allows faster torque drop with slight increase in torque ripple during regenerative braking, as it employs

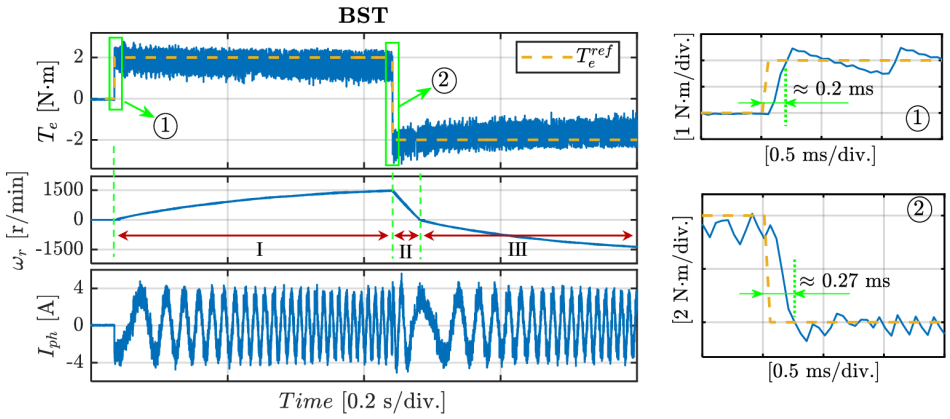

(a)

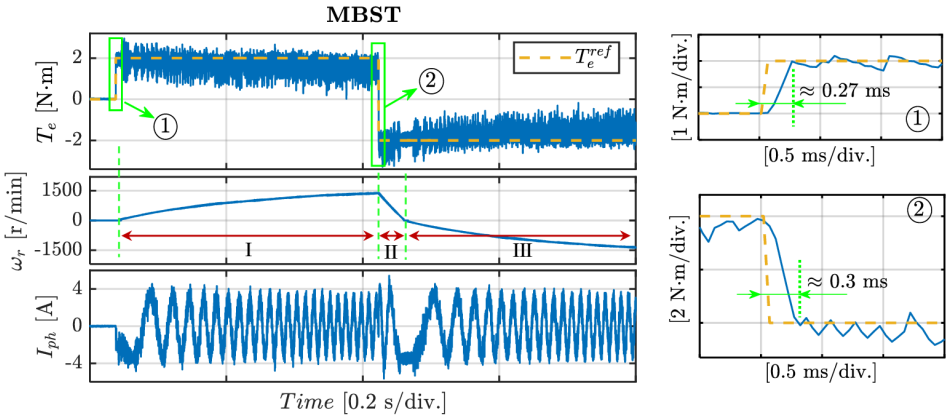

(b)

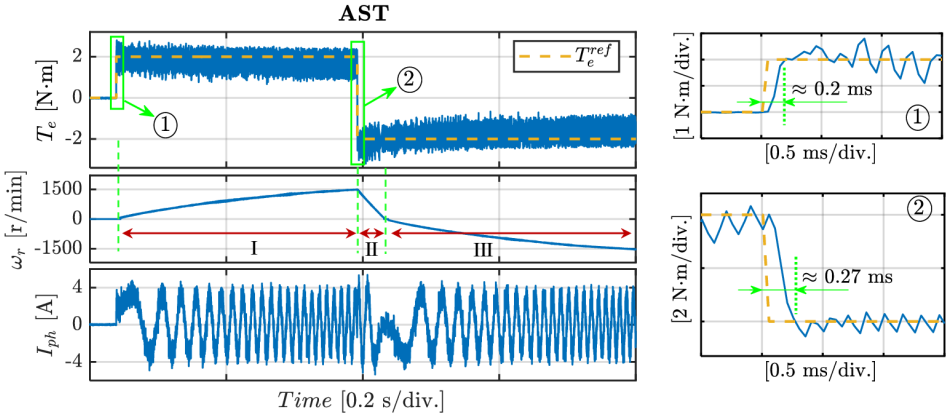

(c)

Figure 4.14: *Cont.*

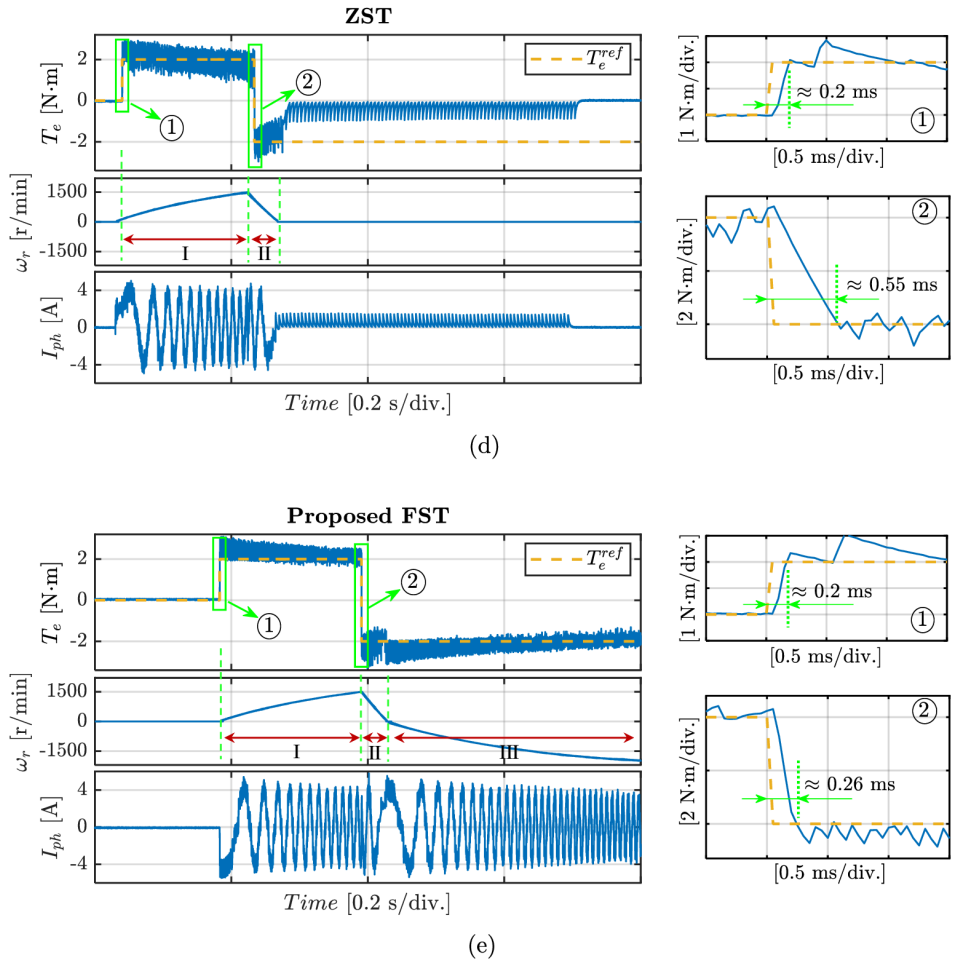

Figure 4.14: Experimental results of the torque dynamic performance for ST-DTC strategies when the torque is stepped up from 0 to 2 N·m and down from 2 to −2 N·m. (a) BST. (b) MBST. (c) AST. (d) ZST. (e) FST. [The waveforms are (from top to bottom): electromagnetic torque, rotor speed, and phase current. The operation modes: I) forward motoring, II) forward regenerative braking, III) backward motoring]

only the AVVs during the dynamic state to ensure smooth speed reversal (i.e., smooth transition from the forward regenerative braking to the backward motoring mode), as can be seen in Fig. 4.14(e). After speed reversal (i.e., under backward motoring operation), ZVVs are activated at two state of FST to achieve a steady-state performance similar to that of the forward motoring mode. The experimental results confirm that the proposed FST provides the lowest steady-state ripples in torque and stator flux while reducing the average switching frequency and enhancing the torque response and system stability during speed reversal.

4.7 Chapter Summary

This chapter presented a generalized investigation of how the ST-DTC performance of the three-phase PMSM drive system is affected by the torque and flux deviations produced by each voltage vector that the 2L-VSI admits. Based on that, different existing switching tables in the literature are theoretically assessed and compared to identify the best voltage vector at each table state. Moreover, a flexible switching table (FST)-based strategy is proposed to improve the overall performance of the ST-DTC for PMSM. Unlike the conventional switching tables, FST changes its structure according to the operating conditions, which requires information only about the reference torque and the rotation direction. In this strategy, the voltage vectors that produce relatively low deviations in torque and flux are employed during steady-state operation to minimize the torque and flux ripples. On the other hand, those of them that give high deviations are applied during system dynamics to maintain the fast response of the conventional scheme.

Simulation and experimental results have been presented to verify the feasibility and effectiveness of the proposed strategy. Compared with the existing switching tables, the main features achieved by employing FST in the ST-DTC system of PMSM can be summarized as follows:

1. Reduced torque and flux ripples by averages of 44% and 16%.
2. Reduced average switching frequency by 37%, on average, while improving the current distortion by 19%, approximately.
3. Ease of implementation as the FST-based DTC method does not require hysteresis regulators.
4. Enhanced torque dynamic performance with smooth speed reversal.

However, similar to the conventional ST-DTC method, the proposed strategy cannot guarantee the optimal voltage vector selection and applies the selected voltage vector for the entire sampling period, limiting the torque ripple reduction. Also, it cannot recognize the magnitude of the torque error, resulting in poor torque tracking performance during steady-state operation. To overcome these problems, the proposed FST is extended and used in other DTC approaches, such as the DRR-based DTC for further torque-performance improvement, as will be discussed in the next chapter.

Chapter 5

Torque-Performance Improvement of Direct Torque Controlled PMSM Based on Duty-Ratio Regulation

5.1 Chapter Overview

The conventional DTC (CDTC) schemes, discussed in the previous chapter, neglect the torque-error magnitude and apply the selected voltage vector for the whole control cycle, which, despite providing a fast dynamic response, results in unavoidable steady-state torque error and high torque ripple if the sampling period is not short enough. Therefore, a new duty-ratio regulation-based strategy is proposed in this chapter to improve the torque performance of the DTC for three-phase PMSMs. It employs a duty-ratio regulator (DRR) to incorporate AVV and ZVV at every control sample and avoid triggering the AVVs that produce high torque deviations

during steady-state operation. This DRR considers the contrary change in the positive and negative torque deviations of the voltage vectors with the rotational speed variations to minimize the torque ripple and uses a virtual reference signal to eliminate the steady-state torque error.

The proposed method provides enhanced torque control performance meanwhile maintaining the main advantages of the CDTC technique, including simple structure, fast transient response, and good robustness. The feasibility and effectiveness of the proposed strategy are verified through a detailed comparative assessment with the CDTC scheme and two existing duty regulation-based DTC methods using experimental results obtained from the 0.75-kW PMSM drive system.

The rest of this chapter is organized as follows. In Section 5.2, the torque-control performance issues of the CDTC is further discussed. Then, the proposed method is described in Section 5.3, including an improved DRR to reduce the torque ripple and compensate for the steady-state torque error using a virtual reference generator. In Section 5.5, the proposed DTC strategy is theoretically compared with the CDTC and prior DRR-based strategies. This comparison is experimentally verified in Section 5.6 to confirm the feasibility and effectiveness of the proposed strategy. Finally, the conclusion is drawn in Section 5.7.

5.2 Torque Performance Issues of the ST-DTC approaches

As discussed in Section 4.3, the AVVs produce a relatively large deviations in torque when applied for the entire control cycle, resulting in high torque

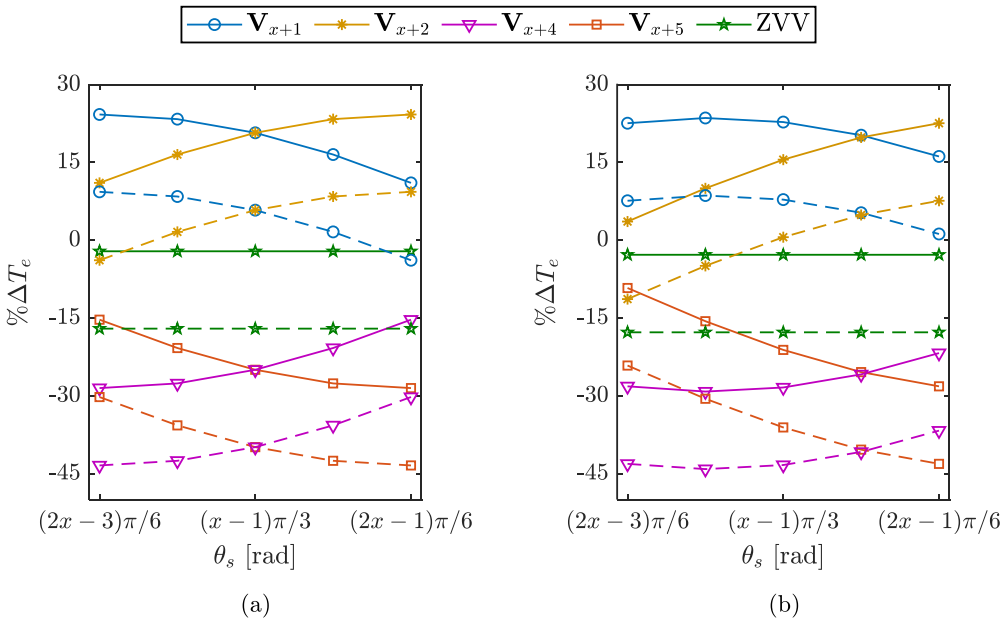

Figure 5.1: Percentage torque deviations produced by each voltage vector at different operating conditions and sampling period of 50 μs when θ_s is varied by the spatial range of sector x. (a) at no load (b) at full load. [solid line: at 10% of rated speed; dashed line: at 80% of rated speed]

ripple. Also, the positive and negative torque deviations varies contradictorily with the variations of operating speed. For better illustration of these contrasting behaviors, the torque deviations shown in Fig. 4.3 are redrawn in Fig. 5.1 for each voltage vector, assuming that the motor runs in forward direction.

As can be noticed from Fig. 5.1, the operating speed has a great impact on the torque deviations compared to that of the load torque. At low speed, the positive torque deviations of $\mathbf{V}_{x+1}$ and $\mathbf{V}_{x+2}$ are almost the same as the negative torque deviations of $\mathbf{V}_{x+4}$ and $\mathbf{V}_{x+5}$. With the speed increase, the positive torque deviations weaken while the negative torque deviations strengthen, which means that the selected AVVs can force the motor torque to increase slowly and decrease rapidly. As this selected AVV is applied for the entire control cycle, the average torque produced by the machine is inevitably lower than the reference signal, leading to the steady-state

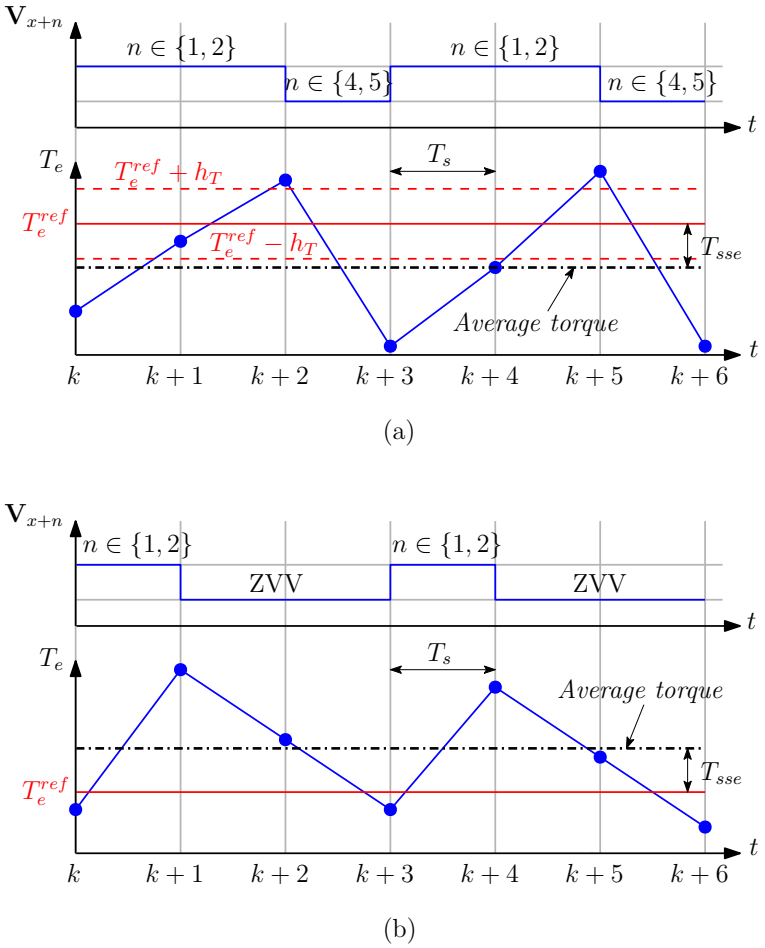

Figure 5.2: Illustration of the steady-state torque error due to the difference between the positive and negative torque deviations produced by the voltage vectors employed in (a) BST at high speeds, and (b) FST at low speeds.

torque error (T_{sse}), as illustrated by Fig. 5.2(a). This torque error can be noticed in Fig. 4.14, which is calculated as the difference between the average value of the estimated torque and the reference signal for the speed range between 100 and 1500 r/min, as shown in Fig. 5.3. According to Fig. 5.3, the maximum absolute value of the torque error produced by the ST-DTC methods is around 20% of the rated torque. This value occurs at the highest speed in case of employing BST, MBST, and AST, while it is produced at the lowest speed by utilizing the proposed FST. Thus, it can be stated that the steady-state torque error can be reduced at high speeds by increasing the frequency of ZVV selection, as the FST allows.

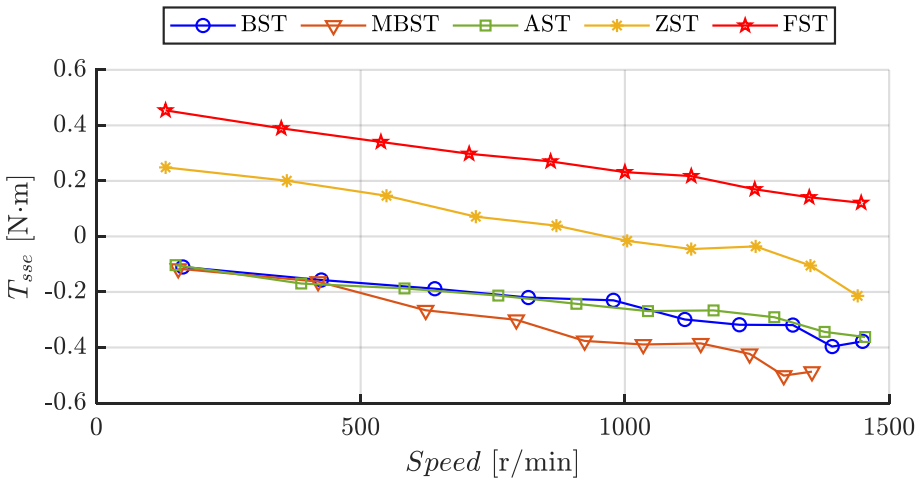

Figure 5.3: Steady-state torque error of the ST-DTC strategies obtained from the experimental results presented in Fig. 4.14 for the positive speed range between 100 and 1500 r/min.

However, this error will increase at low speed because of the high difference between the torque deviations produced by AVVs and ZVVs, as depicted in Fig. 5.2(b).

Although the torque performance of the CDTC (using BST) depends on the hysteresis bounds of torque regulator (i.e., $\pm h_T$), as it manipulates the voltage vector selection [134], the steady-state torque error is still an issue. For instance, making h_T very small will cause easy activation for the state "$\varepsilon_T = -1$" that requires applying either $\mathbf{V}_{x+4}$ or $\mathbf{V}_{x+5}$, depending on the flux regulator state [see Table 4.1]. By increasing the value of h_T, the state "$\varepsilon_T = 0$" that employs the ZVV, will be triggered more frequently. As a consequence, a torque ripple reduction can be achieved. However, excessive h_T forces the torque to decay too much to switch from the state "$\varepsilon_T = 0$" to "$\varepsilon_T = 1$", causing large steady-state torque error, and deteriorates dynamic response when a torque drop is demanded.

According to the aforementioned discussion, the maximum allowable torque ripple reduction can be achieved in the ST-DTC if zero hysteresis bounds are used, and the ZVV is applied at either the state where "$\varepsilon_T =$

-1" or "$\varepsilon_T = 1$" depending on the rotation direction. However, the AVVs are better options at these table states during system dynamics, as they force the torque to change faster than the ZVVs. Hence, information about the system operating state is required to switch between AVVs and ZVVs, as presented in Chapter 4. Although this can simplify the implementation owing to the hysteresis bounds elimination, the torque ripple reduction is limited, and the steady-state torque error is unavoidable. Hence, the duty-ratio regulation concept is utilized in this chapter to avoid employing the AVVs that produce high torque deviation, and inherently increases the frequency of applying the ZVV for further torque ripple reduction.

5.3 Torque Performance-Enhanced DTC with Multiobjective DRR

5.3.1 Concept of the Proposed DRR

The proposed DTC strategy uses a DRR to employ one AVV for a working duration of DT_s, where D is the duty ratio, then switches it to a ZVV for the remaining time of the control cycle. The AVV is selected based on the error signs of torque and stator flux amplitude, as follows:

$$\mathbf{V}_{x+n} = \begin{cases} \mathbf{V}_{x+1}, \text{ if } T_{err} \geq 0 \text{ and } \psi_{err} \geq 0 \\ \mathbf{V}_{x+2}, \text{ if } T_{err} \geq 0 \text{ and } \psi_{err} < 0 \\ \mathbf{V}_{x+4}, \text{ if } T_{err} < 0 \text{ and } \psi_{err} < 0 \\ \mathbf{V}_{x+5}, \text{ if } T_{err} < 0 \text{ and } \psi_{err} \geq 0 \end{cases} \tag{5.1}$$

The proposed DRR aims to apply that AVV for a duration that only allows the torque to reach the reference value, as shown in Fig. 5.4. And

hence, the duty ratio can be determined using the following expression:

$$D_{x+n} = \frac{T_{err}}{\Delta T_e[x+n]} \tag{5.2}$$

This DRR guarantees that the absolute value of the torque at each sampling instant is always less than or equal to that of the reference signal during steady-state operation. Consequently, the condition "$T_{err} < 0$" will never be satisfied when the machine rotates in the forward direction, which eliminates the high torque deviations produced by $\mathbf{V}_{x+4}$ and $\mathbf{V}_{x+5}$. Similarly, when the speed is reversed, the high torque deviations of $\mathbf{V}_{x+1}$ and $\mathbf{V}_{x+2}$ are eliminated by avoiding triggering the state "$T_{err} \geq 0$." On the other hand, under dynamic conditions, these AVVs are allowed to be applied for a duration proportional to the torque error, ensuring a dynamic response as fast as that of the ST-DTC.

Although this method can reduce the torque ripple considerably, it makes the system more parameter dependent due to the required calculation of the torque deviation ΔT_e using (5.2). It also introduces a steady-state torque error because the average value of the produced torque will be smaller than the reference torque, as inferred by Fig. 5.4. The compensation for these issues is presented in the following subsections.

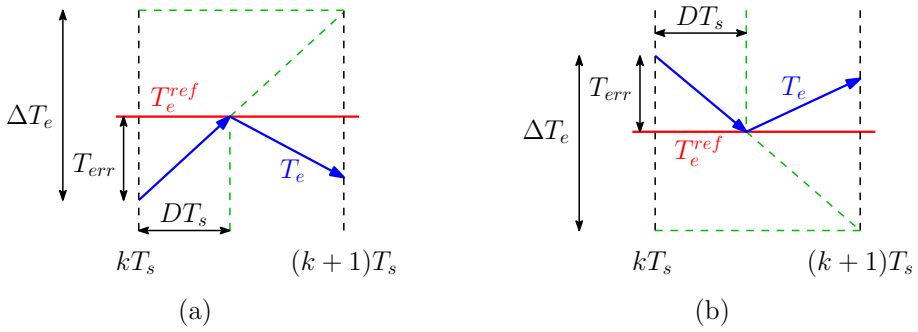

Figure 5.4: Duty-ratio determination for different operation modes (motoring or regenerative braking). (a) Forward, (b) Backward.

5.3.2 Compensation of Steady-State Torque Error

A virtual-reference generator is proposed to compensate for the steady-state torque error due to the duty-ratio regulation method. Fig. 5.5 illustrates the principle of the proposed steady-state error compensation. It can be noticed that the DRR constrains the produced torque T_e between the reference signal (T_e^{ref}) and the minimum torque (T_e^{min}) that represents the estimated torque at every control sample. If the reference torque is increased to a virtual value (i.e., $T_e^{v\_ref}$), represented by the red dashed line in Fig. 5.5, it will not affect the voltage vector selection, and hence, the slope of the torque remains the same with and without compensation. Moreover, the selected AVV will be employed for a longer duration (i.e., $\bar{D}T_s > DT_s$), according to (5.2). In consequence, the ZVV will decrease the torque to a smaller absolute value, which means that T_e^{min} will increase, as depicted by the green dashed line in Fig. 5.5. Thus, it can be assumed that the steady-state torque error will be eliminated if the following condition is achieved, i.e.,

$$T_e^{v\_ref} - T_e^{ref} = T_e^{ref} - T_e^{min}. \tag{5.3}$$

According to (5.3), the virtual reference signal $T_e^{v\_ref}$ can be generated by adding a correction value (γ) to the original reference torque depending

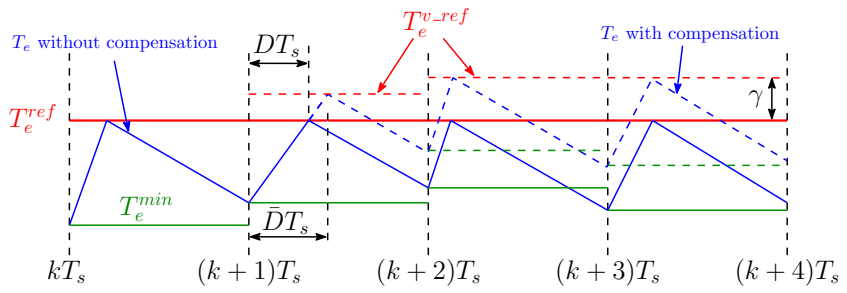

Figure 5.5: Principle of the proposed compensation for steady-state torque error.

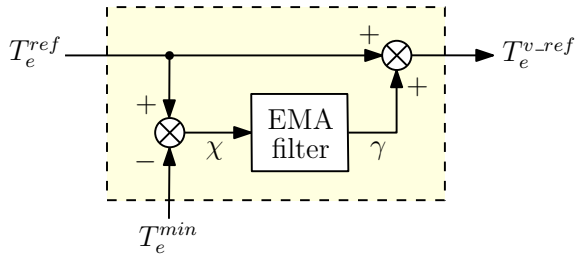

Figure 5.6: Virtual-reference generator.

on the difference between T_e^{ref} and T_e^{min}, as shown in Fig. 5.6. Since this difference changes randomly every control sample, the reference correction is obtained using a simple filter, such as the exponential moving average (EMA) filter [135].

The EMA filter provides a smoother means of averaging compared with the traditional moving average, especially during sudden changes in the input signal. This smooth averaging is because the EMA applies weights that decline successively with the age of the input signal samples, while the other employs equal weights according to the length of a particular observation window, resulting in undesired pulsations [136]. Given a signal χ to be filtered (i.e., $T_e^{ref} - T_e^{min}$), then the moving average-filtered output $\gamma[k]$ is obtained using the current input $\chi[k]$ and the previous output $\gamma[k-1]$, according to the following difference equation:

$$\gamma\,[k] = \lambda\ \chi[k] + (1-\lambda)\ \gamma[k-1], \tag{5.4}$$

where λ is the smoothing factor that could be in the range $0 < \lambda < 1$. The closer the value of λ to 0, the less frequent the filter output changes, and the smaller the cutoff frequency (f_c) will be. Based on (5.4), the relationship between λ and f_c can be obtained as [36]

$$f_c = \frac{f_s}{2\pi}\ \cos^{-1}\left(\frac{\lambda^2 + 2\lambda - 2}{2\lambda - 2}\right), \tag{5.5}$$

where $f_s = 1/T_s$ is the sampling frequency. The cutoff frequency of the filter should be selected in such a way as to achieve a stable reference correction under steady-state operation and avoid pulsation during transients. Hence, it should be restricted to a small fraction of the control bandwidth, e.g., below 1/20. For the machine under test, the maximum available bandwidth can be up to around 1/3 of the sampling frequency, as can be inferred by the torque deviations shown in Fig. 5.1. Therefore, with a sampling period of 100 μs, the filter's cutoff frequency is chosen as 50 Hz, and the smoothing factor is calculated as 0.03 using (5.5).

5.3.3 Mitigation of the Parameter Dependence

To improve the robustness of the proposed DRR against parameter variations, a simple method is proposed to obtain the torque deviation due to the AVV (ΔT_e). For simplicity, the effect of the load torque on the torque deviations can be neglected compared to that of the operating speed, as shown in Fig. 5.1.

From Fig. 5.1, it can be noticed that the torque deviation of the AVV varies sinusoidally with the angular position θ_s of the stator flux vector. Additionally, it shifts down with a constant value equals to the torque deviation of the ZVV, depending on the rotational speed. Therefore, the torque deviation of the AVV that increases the torque ($\Delta T_e^+ \geq 0$), i.e., $\mathbf{V}_{x+1}$ or $\mathbf{V}_{x+2}$ can be approximated as

$$\Delta T_e^+ = \begin{cases} A\left|\sin\left(\theta_s + \frac{2\pi x}{3}\right)\right| - \frac{B\omega_r}{\omega_{rn}}, & \text{for } \mathbf{V}_{x+1} \\ A\left|\sin\left(\theta_s + \frac{\pi(2x-1)}{3}\right)\right| - \frac{B\omega_r}{\omega_{rn}}, & \text{for } \mathbf{V}_{x+2} \end{cases} \tag{5.6}$$

where A is the absolute value of the maximum torque deviation of the AVV at zero speed ($\omega_r = 0$), and B is the absolute value of the torque deviation of the ZVV at rated speed (ω_{rn}). Similarly, the torque deviation of the AVV that decreases the torque ($\Delta T_e^- \leq 0$), i.e., $\mathbf{V}_{x+4}$ or $\mathbf{V}_{x+5}$, can be determined as follows:

$$\Delta T_e^- = \begin{cases} -A\left|\sin\left(\theta_s + \frac{2\pi x}{3}\right)\right| - \frac{B\omega_r}{\omega_{rn}}, & \text{for } \mathbf{V}_{x+4} \\ -A\left|\sin\left(\theta_s + \frac{\pi(2x-1)}{3}\right)\right| - \frac{B\omega_r}{\omega_{rn}}, & \text{for } \mathbf{V}_{x+5}. \end{cases} \tag{5.7}$$

From (5.6) and (5.7), it is obvious that ΔT_e^+ and ΔT_e^- will have equal absolute values at zero speed. When the speed increases, the absolute value of ΔT_e^- will be larger than that of ΔT_e^+. Conversely, if the rotation direction reverses (i.e., ω_r is negative), the absolute value of ΔT_e^- will be less than that of ΔT_e^+, which conform to the results obtained by (4.10), and reveal that both (5.6) and (5.7) can be used with both rotation directions. Thus, the duty ratio represented by (5.2) can be rewritten as

$$D_{x+n} = \begin{cases} \frac{T_e^{v\_ref} - T_e}{\Delta T_e^+}, & \text{if } T_e^{v\_ref} \geq T_e \\ \frac{T_e^{v\_ref} - T_e}{\Delta T_e^-}, & \text{if } T_e^{v\_ref} < T_e. \end{cases} \tag{5.8}$$

From (5.8), if proper positive values are set for A and B, the duty-ratio calculation will be simplified, and the dependence on the parameters will be mitigated while considering the operating speed impact on the torque deviations. According to the definition, A can be determined from (4.10) using the given parameters with $\omega_r = 0$ and $T_e = 0$, as

$$A = \frac{pV_{dc}\psi_{pm}T_s}{L_s}. \tag{5.9}$$

And an approximate value for B can be obtained with zero voltage, $\omega_r = \omega_{rn}$, and $T_e = 0$, as

$$B = \frac{3p\omega_{rn}{\psi_{pm}}^2 T_s}{2L_s}. \tag{5.10}$$

Although (5.9) and (5.10) are obtained using the machine parameters, ψ_{pm} and L_s, the torque deviation range will not change much with the parameter variation whose impact on the overall control performance can be neglected, as the experimental results will confirm.

5.3.4 Duty-Ratio Optimization

As mentioned in 4.3, the speed increase weakens the torque deviation produced by AVVs that increase the absolute value of torque, while it strengths that generated by ZVVs. As a result, the duty cycle saturates (i.e., $D_{x+n} \approx 1$), especially at high-speed and loading conditions. This saturation causes high torque pulsations due to applying ZVV once the torque signal hits the virtual reference torque ($T_e^{v\_ref} = T_e^{ref} + \gamma$), as illustrated by the example given in Fig. 5.7,resulting in less effective duty-ratio regu-

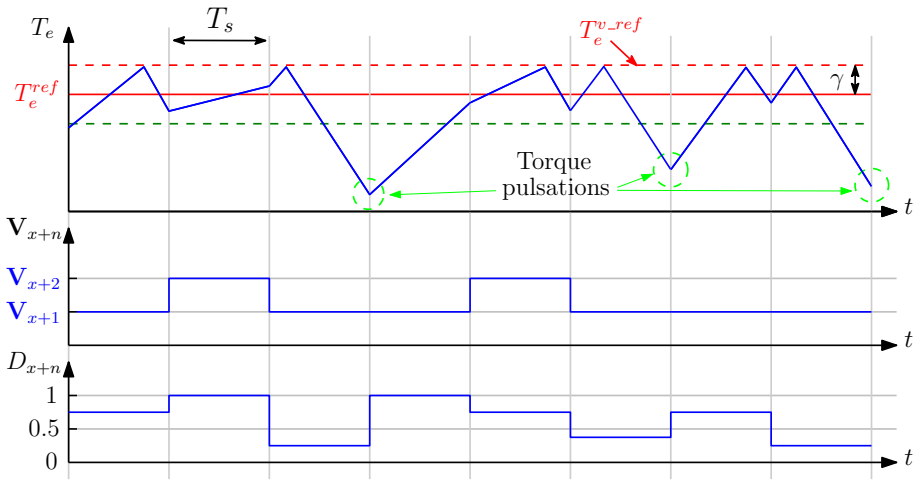

Figure 5.7: An example of the torque pulsation issue caused by the non-optimized duty-ratio regulation, assuming that the rotor speed is high positive value.

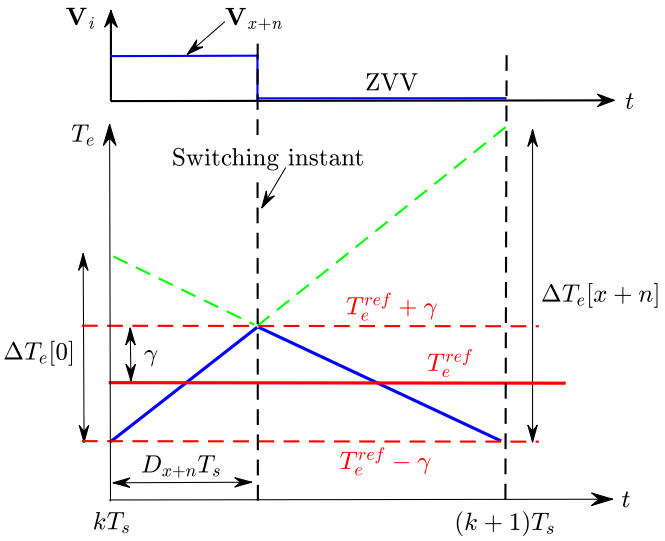

Figure 5.8: Optimized duty-ratio regulation.

lation. To avoid this issue, the duty ratio D_{x+n} expressed by (5.8) needs to be further optimized.

To minimize the torque ripple, the duty cycle should be regulated so that the torque is maintained within the boundaries $T_e^{ref} \pm \gamma$, as shown in Fig. 5.8. Hence, the torque at the end of the sampling period should equal the lower boundary ($T_e^{ref} - \gamma = T_e^{v\_ref} - 2\gamma$), such that

$$T_e^k + D_{x+n}\Delta T_e[x+n] + (1 - D_{x+n})\Delta T_e[0] = T_e^{v\_ref} - 2\gamma \tag{5.11}$$

where $\Delta T_e[x+n]$ and $\Delta T_e[0]$ are the torque deviations produced by the AVV and ZVV, respectively, when applied for the entire control cycle. Also, to guarantee that the torque T_e will not exceed the upper boundary (i.e., the virtual reference signal $T_e^{ref} + \gamma$), the relationship between $\Delta T_e[0]$ and γ has to satisfy the following condition [137]

$$\Delta T_e[0] = C\ \gamma, \tag{5.12}$$

where $C = 2(\Delta T_e[0] - \Delta T_e[x+n])/\Delta T_e[x+n]$ is a speed-dependent vari-

able that can be obtained by averaging (5.6) and (5.7) as,

$$C = \frac{2\sqrt{3}A\omega_{rn}}{2B|\omega_r| - \sqrt{3}A\omega_{rn}}. \tag{5.13}$$

Substituting (5.12) into (5.11), the optimized form of the duty-cycle (5.8) can be expressed as follows:

$$D_{x+n} = \begin{cases} \frac{T_e^{v\_ref} - T_e - (2+C)\gamma}{\Delta T_e^{+} - C\gamma}, & \text{if } T_e^{v\_ref} \geq T_e \\ \\ \frac{T_e^{v\_ref} - T_e - (2+C)\gamma}{\Delta T_e^{-} - C\gamma}, & \text{if } T_e^{v\_ref} < T_e \ . \end{cases} \tag{5.14}$$

5.3.5 Impact of the Voltage Vector Selection on Flux Control Performance

According to the discussion in 4.5.2, assuming that the machine runs in the forward direction, if either the voltage vector $\mathbf{V}_{x+2}$ or $\mathbf{V}_{x+1}$ is triggered in *Subsector* I or *Subsector* II, respectively, during the transition of the stator flux vector from one sector to another, a large deviation in the flux amplitude occurs, causing high flux ripple and current distortion.

To illustrate, an example is given in Fig. 5.9, where the stator flux amplitude is initially larger than the reference signal, and the stator flux position angle is slightly below -30 electrical degrees (i.e., $T_{err} > 0$, $\psi_{err} < 0$, and $x = 6$). Thus, the voltage vector ($\mathbf{V}_{x+2} = \mathbf{V}_2$) is employed with a small duty cycle, and the stator flux amplitude decays slowly, as shown in Fig. 5.9(a) (as $\mathbf{V}_{x+2}$ provides high torque deviation and low negative flux deviation in *Subsector* II). Once the stator flux vector enters the first sector (i.e., $x = 1$), the voltage vector ($\mathbf{V}_{x+2} = \mathbf{V}_3$) is employed with a large duty ratio because $\mathbf{V}_{x+2}$ provides low torque deviation in *Subsector* I, resulting

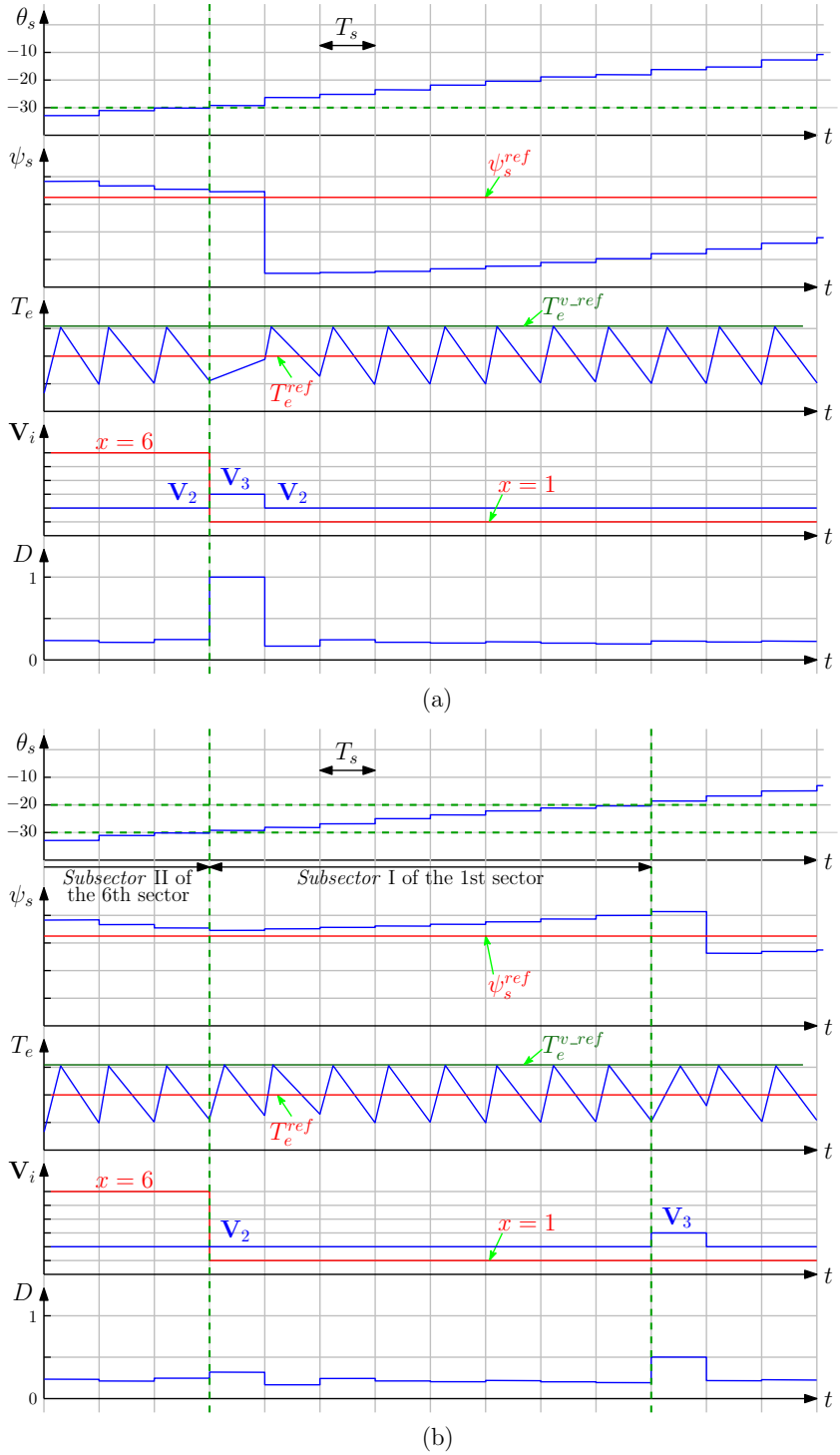

Figure 5.9: Illustration of the voltage selection impact on the flux control performance. (a) without voltage replacement. (b) with voltage replacement.

in a large dip in the flux amplitude as $\mathbf{V}_{x+2}$ produces high negative flux deviation in that subsector. This situation is frequently repeated in the proposed method due to the large difference between the flux deviations produced by the two active voltage vectors that can be employed during

steady-state operation, leading to the increase of the stator flux ripple. To avoid this issue, one condition need to be added to the control algorithm to replace the AVV selected from (5.1) when the stator flux vector is located within the spacial range of either *Subsector* I or II, according to the voltage replacement strategy expressed by (4.20) and (4.21).

The benefit of the voltage replacement can be noticed in Fig. 5.9(b). As shown in this figure, $\mathbf{V}_{x+1}$ replaced $\mathbf{V}_{x+2}$ when the stator flux vector enters the 1st sector (i.e., *Subsector* I, if the angle σ is set to 10 electrical degrees). Although the flux needs to be decreased to follow the reference signal, and $\mathbf{V}_{x+1}$ produces positive flux deviation at that position, this flux deviation is very small in *Subsector* I and the small duty ratio makes the flux almost constant. Once the stator flux position exceeds -20 electrical degree, the voltage vector $\mathbf{V}_{x+2}$ is normally triggered (as $\sigma = 10$ degrees), according to (5.1), which decreases the flux amplitude with a smaller deviation compared with that of Fig. 5.9(a), considering that the duty ratio will be smaller as well. Therefore, the flux-performance degradation can be avoided by using the voltage replacement strategy when the absolute error of the stator flux amplitude is less than half of the maximum flux deviation ($\Delta\psi_s^{max}$) produced by $\mathbf{V}_{x+n}$ and roughly obtained from (4.13) as $\sqrt{3}V_{dc}T_s/3$.

5.4 A Case Study for the Proposed DRR-DTC Implementation

Fig. 5.10 shows the overall control structure of the proposed method. Unlike CDTC, the proposed method utilizes the error between the reference signals and the estimated values of torque and stator flux amplitude, instead of the hysteresis regulators, to select the AVV using (5.1) and the corresponding

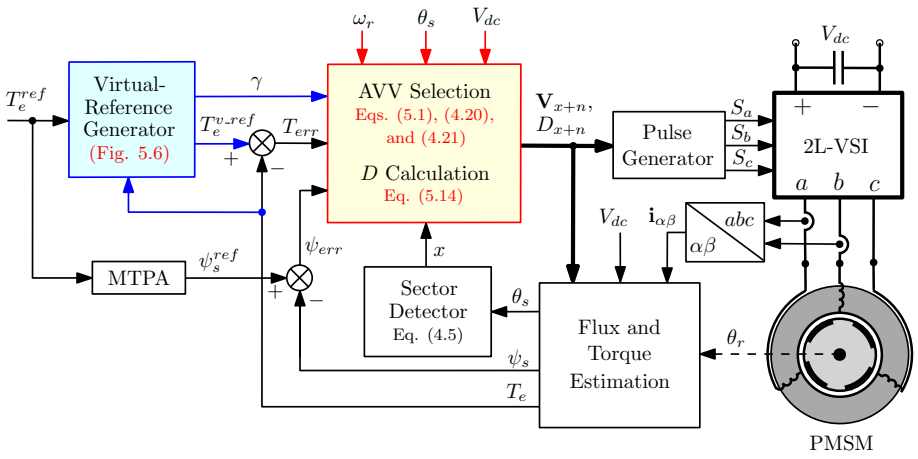

Figure 5.10: Overall control structure of the proposed DRR-based DTC strategy.

duty ratio is calculated using (5.14). Then, the selected AVV is switched to a proper ZVV such that $\mathbf{V}_1$, $\mathbf{V}_3$, and $\mathbf{V}_5$ are changed to $\mathbf{V}_0$, while other AVVs are followed by $\mathbf{V}_7$ to minimize the switching frequency. The torque demand is modified by the virtual reference generator, shown in Fig. 5.6, for steady-state error compensation. Additionally, it is used to obtain the reference stator flux amplitude based on MTPA principle, using (4.15). Because this study aims to improve the torque control performance, the MTPA strategy is used with the assumption that it is insensitive to parameters variation as this issue is comprehensively studied in [82].

The implementation of the proposed DRR-based DTC method can be divided into three steps, as shown in Fig. 5.11. Firstly, the flux and torque are estimated using (4.1) and (4.2), respectively. Considering the one-step delay due to digital implementation, its effect can be avoided by selecting the voltage vector based on the predicted values of T_e and ψ_s at the $(k+1)$th-sampling instant. Since the ZVV influence on the stator flux is negligible [see Fig. 4.4], $\boldsymbol{\psi}_{\alpha\beta}$ at $(k+1)T_s$ instant can be determined using the discretized form of (3.2), as

$$\boldsymbol{\psi}_{\alpha\beta}^{k+1} = \boldsymbol{\psi}_{\alpha\beta}^{k} + T_s\left(D^k\mathbf{V}_i^k - R_s\mathbf{i}_{\alpha\beta}^k\right) = \psi_s^{k+1}e^{j\theta_s}. \tag{5.15}$$

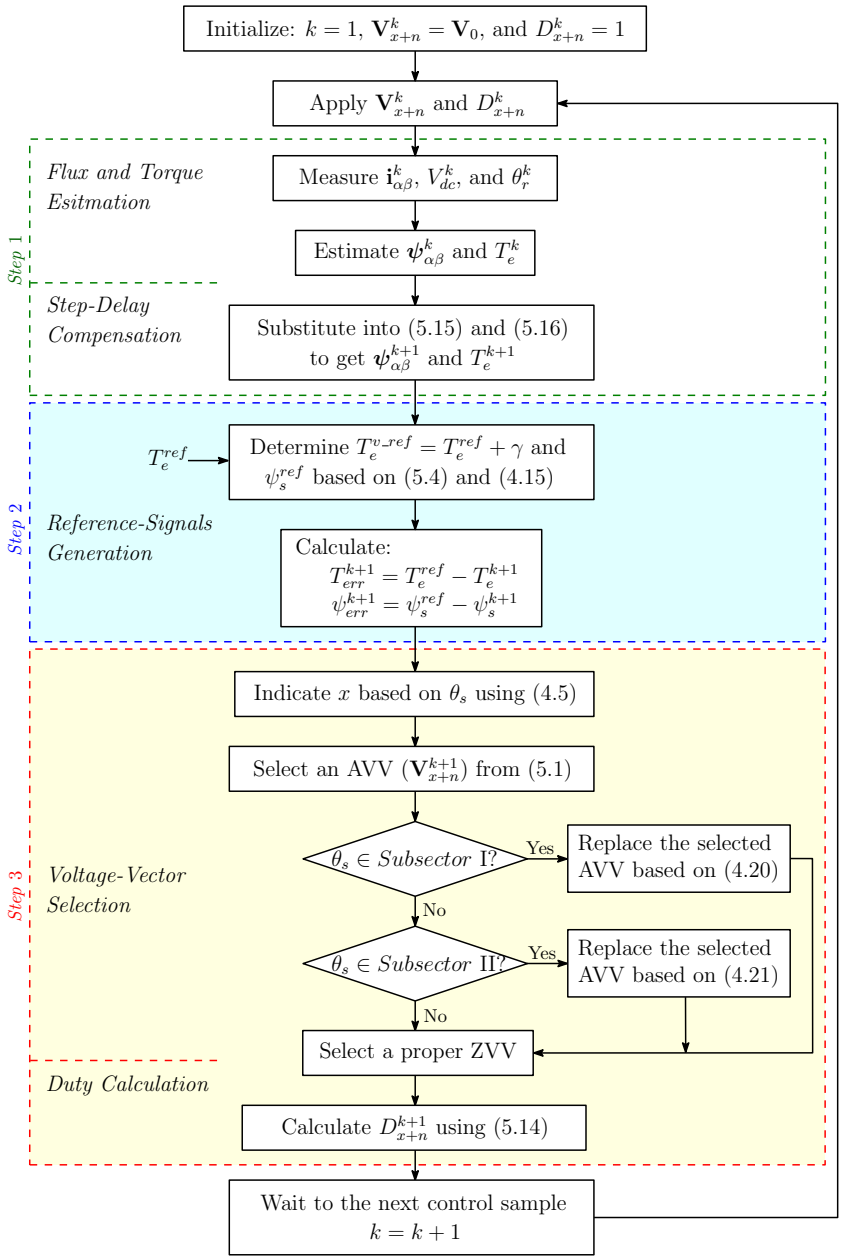

Figure 5.11: Flowchart of the proposed DRR-based DTC strategy.

Whereas the torque at $(k+1)T_s$ instant can be obtained as

$$T_e^{k+1} = T_e^k + D^k \Delta T_e^k - \left(1 - D^k\right) \frac{B\omega_r}{\omega_{rn}}, \tag{5.16}$$

where the second and third terms represent the impact of the AVV and ZVV, respectively, on the torque. Secondly, the reference torque is cor-

rected by a value of γ obtained from (5.4), and it is used to generate the reference flux amplitude based on (4.15). These reference and predicted values are used to determine the sign of the error in torque and flux amplitude needed for the AVV selection via (5.1) after indicating x by using (4.5). To avoid deterioration of flux control performance, the selected AVV is replaced according to (4.20) or (4.21) if the stator-flux vector is located in either *Subsector* I or II. Finally, the duty ratio of the AVV is calculated according to (5.14), which will be applied at the beginning of the future control interval.

5.5 Theoretical Comparison with Existing DRR-based DTC Approaches

The duty-ratio modulation techniques are introduced in DTC to reduce the torque ripple by combining an AVV with a ZVV at every control cycle. In [32], the AVV is first selected from the AST, then the corresponding duty cycle is obtained to minimize the root mean square (RMS) or the final value of torque error over the control period, using the following expressions:

$$D_{RMS} = \frac{2T_{err} - \Delta T_e[0]}{2\Delta T_e[x+n] - \Delta T_e[0]} \tag{5.17}$$

$$D_f = \frac{T_{err} - \Delta T_e[0]}{\Delta T_e[x+n] - \Delta T_e[0]}, \tag{5.18}$$

Since these expression requires calculation of the torque deviations using (4.10), the complexity and reliance on the machine parameters can be considered as limitations [30]. Additionally, they cannot avoid selection of the voltage vectors that produce high torque deviations.

A robust simple DRR-based method has been proposed in [35], where the need for torque-deviation calculations are eliminated, and both the torque- and flux-ripple reductions are considered. This method determines the duty ratio using the following formula,

$$D_{s1} = \left|\frac{T_{err}}{C_T}\right| + \left|\frac{\psi_{err}}{C_\psi}\right|, \tag{5.19}$$

where C_T and C_ψ are two positive constants of torque and flux control. Because the torque deviation is replaced with the constant C_T (i.e., D_s is directly proportional to T_{err}), this method ensures that T_{err} under steady-state operation will be always positive in forward rotation direction and vice versa. Hence, according to AST, it allows selection of the AVVs that produce low torque deviations, reducing the torque ripple. However, the two constants of (5.19) have no solution to get their optimal values and ignore the impact of operating speed on the torque deviations, leading to a considerable steady-state torque error. To clarify, as the torque deviations produced by $\mathbf{V}_{x+1}$ and $\mathbf{V}_{x+2}$ weaken with the positive-speed increase, the duty cycle needs to be increased. As a result, the steady-state torque error is unavoidable because the denominator of (5.19) is constant, which increases with the rotor-speed rise.

Two alternative methods have been proposed in [33] and [34] to overcome this issue. In [33], a proportional-integral (PI)-based DRR has been proposed to obtain the duty cycle, as follows

$$D_{PI} = \left|\frac{3|\omega_r|\psi_{pm}}{2V_{dc}} + T_{err}\left(K_P + \frac{K_I}{s}\right)\right|, \tag{5.20}$$

where K_P and K_I are proportional and integral gains. Despite the simplicity of this method, the dynamic performance of DTC system depends on tuning of the PI-regulator gains. On the other hand, in [34], the torque de-

viation needed for duty-ratio calculation is considered directly proportional to the machine angular speed, as

$$D_{s2} = \begin{cases} \frac{2T_{err}+K_b\omega_r}{K_a-K_b\omega_r}, & \text{if } T_{err} \geq 0 \\ \\ \frac{2T_{err}+K_b\omega_r}{-K_a-K_b\omega_r}, & \text{if } T_{err} < 0. \end{cases} \tag{5.21}$$

where K_a and K_b are two positive constants that depend on the machine parameters and the ratio between the torque deviation at rated speed and that at zero speed. Although this strategy can provide lower steady-state torque error compared with D_{s1} (5.19), it allows employing the AVVs that produce high torque deviations, resulting in higher torque ripple.

Unlike the existing DRR-based approaches, the proposed method uses the duty regulator not only to control the working duration of the AVVs but also to give the highest priority for selecting those of them that cause low torque deviations under the steady-state conditions, hence achieving further torque-ripple reduction. Meanwhile, it can guarantee fast dynamic response, even during speed reversal, as the AVV is employed for a duration proportional to the torque error. Moreover, the virtual reference generator can modify the original reference torque, which effectively mitigates the small torque offset caused by DRR and optimizes the duty ratio to avoid the torque pulsations.

5.6 Experimental Verification

In this section, the experimental setup presented in 3.4 is used to verify the torque-tracking performance of the proposed strategy under speed reversal conditions. Then, the proposed approach is comparatively evaluated with

Table 5.1: Control parameters of the four DTC methods

Methods	**Control parameters**
CDTC	$h_T = \pm$ 2% T_{rated}, $h_\psi = \pm$ 2% ψ_{pm}
D1	C_T = 1.2 N·m, C_ψ = 0.09427 Wb
D2	K_a = 2 N·m, K_b = 6e−4 N·m/(r/min)
Proposed	A = 1.27 N·m, B = 1.02 N·m

the CDTC and two existing DRR-based methods that are specified in this section as D1 [35], and D2 [34]. For the sake of accuracy, the single-step delay due to digital implementation is compensated for all control techniques. The control parameters of the four approaches are listed in Table 5.1. Because the DRR-based strategies (i.e., D1, D2, and proposed) can employ two voltage vectors in one control cycle, their average switching frequency will be higher than that of the CDTC at the same sampling frequency. Thus, for fair comparisons, they are tested at 10 kHz sampling frequency, i.e., half that of the CDTC approach.

5.6.1 Torque-Tracking Performance Assessment

Fig. 5.12 shows the waveforms of the torque, speed, stator phase current, selected AVV, and the corresponding duty ratio for the proposed method. In this experiment, the load torque is set to 1.8 N·m, and the reference torque is stepped up from 0 to 2 N·m until the rotor speed reaches 75% of the rated value, then it is stepped down to −2 N·m to reverse the rotation direction. It can be noticed that T_e and ψ_s follow their reference signals accurately with smooth speed reversal. Also, the higher the speed is, the larger the duty ratio will be because of the reduction of the AVV's torque deviation with the speed increase. From Fig. 5.12, the virtual reference

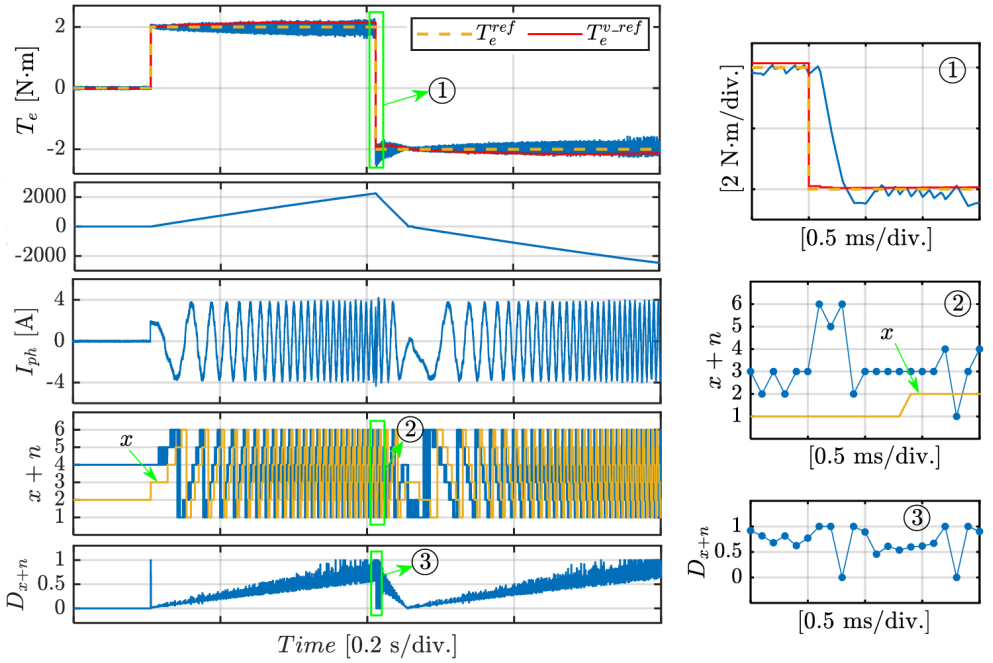

Figure 5.12: Experimental waveforms of torque, speed, stator phase current, selected AVV, and the corresponding duty ratio for the proposed approach.

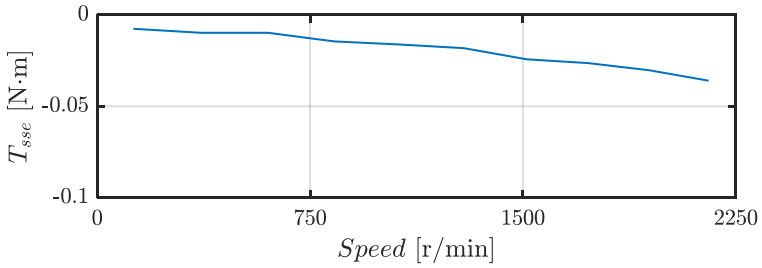

Figure 5.13: Steady-state torque error of proposed DRR-based strategy obtained from the experimental results presented in Fig. 5.12 for the positive speed range between 100 and 2250 r/min.

torque $T_e^{v\_ref}$ can effectively eliminate the steady-state error for both rotation directions. The steady-state torque error is presented in Fig. 5.13 for the speed range between 100 to 2250 r/min, which is negligible compared to those resulted from the CDTC schemes shown in Fig. 5.3.

In Fig. 5.12, the zoomed zone ①, shows the dynamic response of torque when the reference signal is stepped down from 2 to −2 N·m, which confirms that the proposed approach maintains the fast dynamic performance of

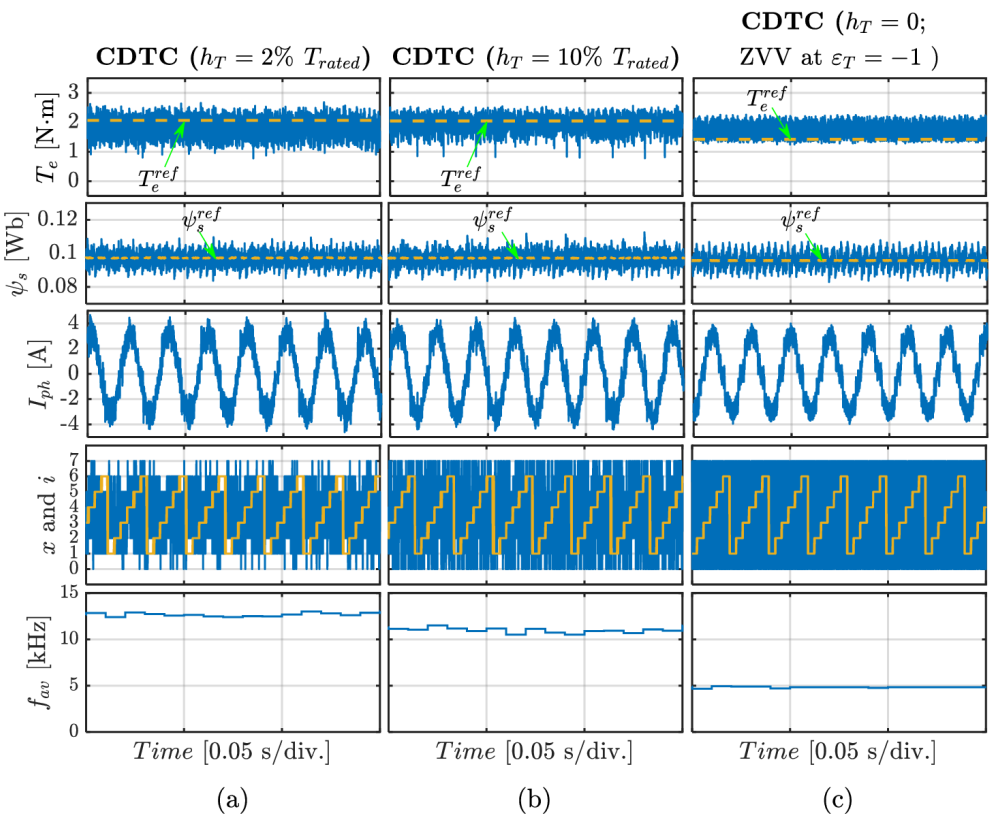

Figure 5.14: Experimental waveforms of the torque, flux amplitude, phase current, and index of the selected voltage vector for the CDTC at 750 r/min under different hysteresis bounds: (a) $h_T = 2\%\ T_{rated}$; (b) $h_T = 10\%\ T_{rated}$; and (c) $h_T = 0$ and ZVV is employed at $\varepsilon_T = -1$.

CDTC. This is achieved because the proposed method can employ either $\mathbf{V}_{x+4}$ or $\mathbf{V}_{x+5}$ with long duty periods ($D_{x+n} \approx 1$), as can be seen in the zoomed zones ② and ③ of Fig. 5.12.

5.6.2 Comparative Evaluation

The steady-state performance of the CDTC is tested under different values of h_T, as shown in Fig. 5.14. In this test, the load torque is set to 1.8 N·m, and the reference torque is increased to a value that maintains the speed around 750 r/min. It can be seen in Fig. 5.14 that increasing the value of h_T from 2% to 10% of the rated torque T_{rated} increases the frequency of employing ZVV ($\mathbf{V}_0$ or $\mathbf{V}_7$), resulting in reduction of torque ripple and

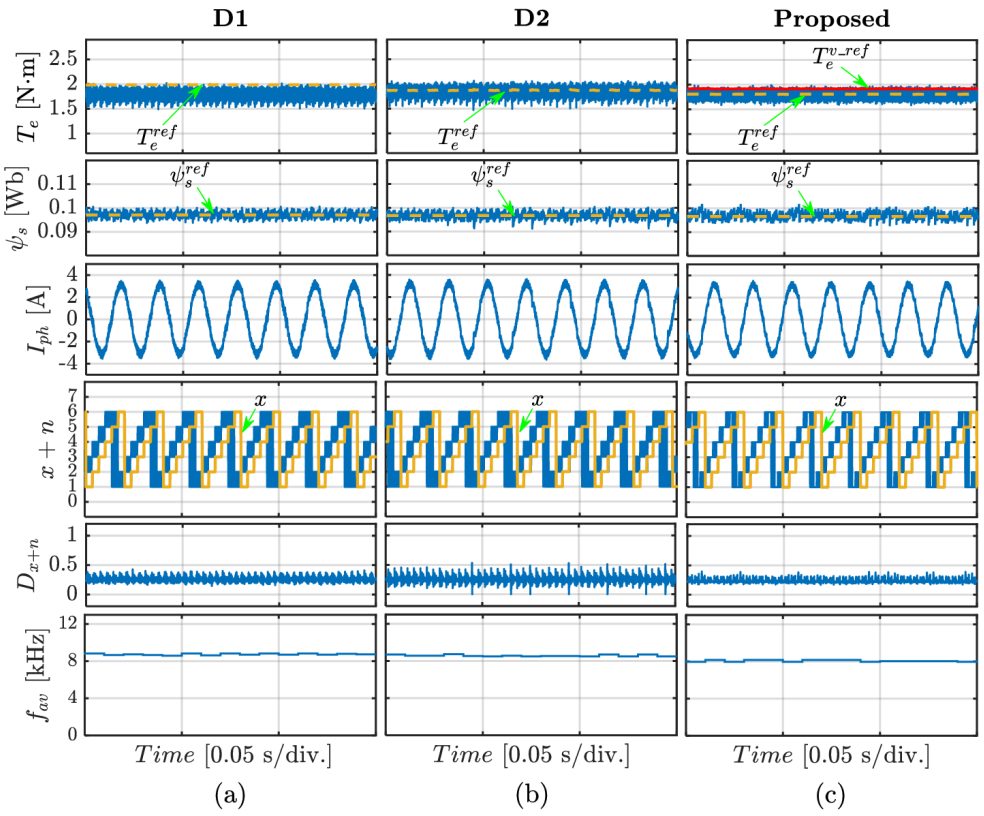

Figure 5.15: Experimental waveforms of the torque, flux amplitude, phase current, index of selected AVV, and duty ratio at 750 r/min and 1.8 N·m load for (a) D1. (b) D2. (c) proposed method.

average switching frequency. The highest reduction of these performance indices is achieved by setting $h_T = 0$ and applying ZVV at the BST's state ($\varepsilon_T = -1$) instead of AVV, as used before in one of the FST modes presented in 4.5. However, the steady-state torque error increases notably, as can be noticed from Fig. 5.14(c). The results agree well with the theoretical analysis presented in 5.2.

Figs. 5.15 and 5.16 illustrate the results of the previous test when repeated for the DDR-based DTC methods at different rotation speeds (around 10% and 75% of the rated speed) and a constant load of 1.8 N·m. Comparing these figures with Fig. 5.14, it is obvious that the duty-ratio regulation can effectively reduce the torque and flux ripples and the stator current distortion of the DTC system regardless of the operating point.

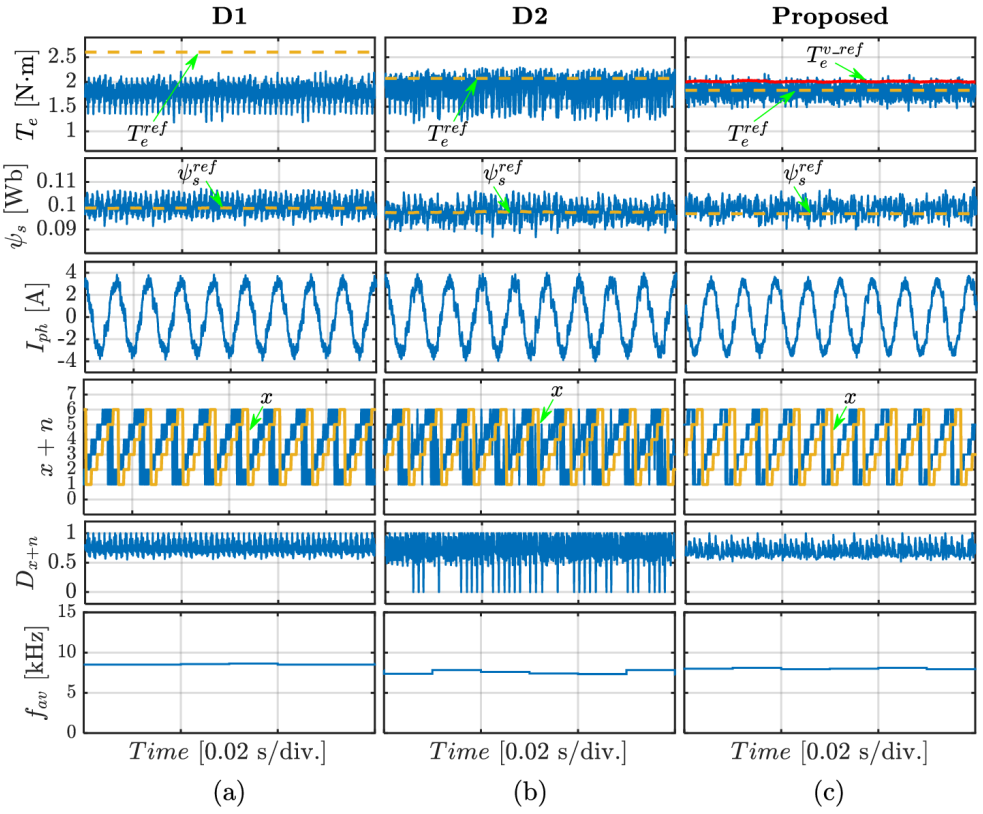

Figure 5.16: Experimental waveforms of the torque, flux amplitude, phase current, index of selected AVV, and duty ratio at 2250 r/min and 1.8 N·m load for (a) D1. (b) D2. (c) proposed method.

According to Fig. 5.15, both D2 and proposed method can mitigates the steady-state torque error of D1, and the proposed scheme achieves the highest torque ripple reduction with a slightly lower average switching frequency. Also, there is insignificant difference between D1, D2, and the proposed method in terms of the flux ripple and current distortion.

On the other hand, the impact of increasing speed to 2250 r/min on the steady-state performance of D1, D2, and the proposed method can be noticed when Fig. 5.16 is compared with Fig. 5.15. Although the steady-state performance deteriorates at high speed, it is still better than that of the CDTC. Compared with D1 and D2, the proposed method achieves the lowest torque ripple and eliminates the steady-state torque error. As shown in Fig. 5.16, both D1 and the proposed method guarantee employing only

$\mathbf{V}_{x+1}$ and $\mathbf{V}_{x+2}$ during steady-state operation, but D2 sometimes utilizes $\mathbf{V}_{x+4}$ and $\mathbf{V}_{x+5}$ instead. As mentioned in 4.3, with the speed increase, the absolute value of the torque deviation of either $\mathbf{V}_{x+1}$ or $\mathbf{V}_{x+2}$ is lower than that of the ZVV, while both $\mathbf{V}_{x+4}$ and $\mathbf{V}_{x+5}$ produce a larger negative torque deviation than the ZVV. Therefore, D1 and the proposed method will apply $\mathbf{V}_{x+1}$ or $\mathbf{V}_{x+2}$ for longer working durations, while D2 will set the duty ratio to zero and employ ZVV for the entire control cycle. Since the ZVV produces large torque deviation at high speed, the torque pulsation in D2 will be higher than those of D1 and the proposed method.

The deterioration of the torque performance with the speed increase is unavoidable because of the increasing differences between the negative and positive torque deviations of ZVV, and $\mathbf{V}_{x+1}$ or $\mathbf{V}_{x+2}$, respectively. Also, $\mathbf{V}_{x+2}$ produces negative torque deviations at high speed and loading conditions in *Subsector* I (see Fig. 5.1), opposing its function in the DTC system. Since the voltage vector replacement strategy can replace $\mathbf{V}_{x+2}$ with $\mathbf{V}_{x+1}$, further torque ripple reduction is provided.

Fig. 5.17 gives the quantitative evaluation of the torque ripple, steady-state torque error, stator flux ripple, average switching frequency, and the total harmonic distortion of the stator current at different speeds and a constant load of 1.8 N·m. According to Fig. 5.17, the CDTC with $h_T = 10\%\ T_{rated}$ achieves 15%, 35%, and 4%, on average, less torque ripple, steady-state torque error, and current distortion than that with $h_T = 2\%\ T_{rated}$. Compared with CDTC, the proposed method achieves ripple reduction with an average of 65% for torque and 42% for stator flux at all speed ranges. The torque ripple reduction of the proposed method is the highest, which is 15% and 41%, on average, compared to D1 and D2, respectively. Also, the flux ripple reduction is higher than that of D2 by an average of 13%. In terms of the steady-state torque error, the pro-

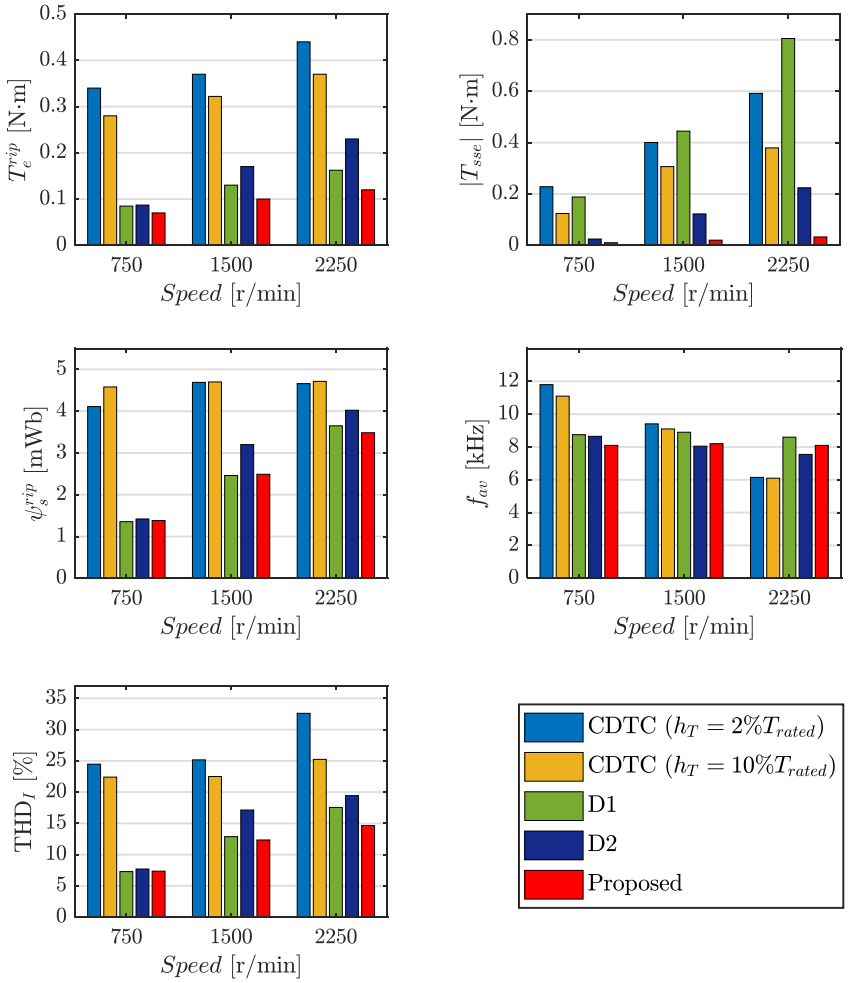

Figure 5.17: Quantitative evaluations for different DTC methods at different speeds and 1.8 N·m load.

posed method provides less error than CDTC, D1, and D2 by around 92%, 95%, and 76%, respectively. These results verify the effectiveness of the proposed method for torque performance improvement without degrading the flux ripple or the current quality.

5.6.3 Sensitivity to Control Parameters Variation

Since the proposed DTC method uses two coefficients, A and B that depend on the machine parameters, its robustness against the parameter drift is tested. Fig. 5.18 presents the torque waveform for the proposed strategy

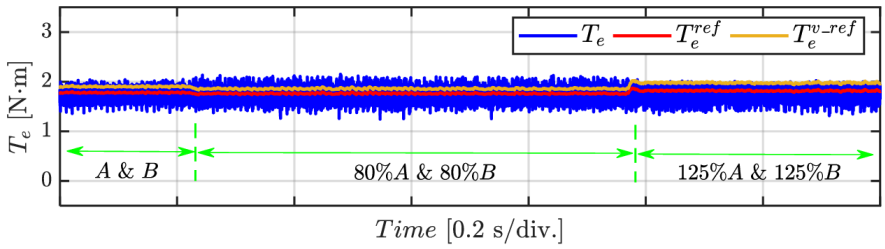

Figure 5.18: Torque steady-state performance of the proposed strategy under different values of the parameters A and B.

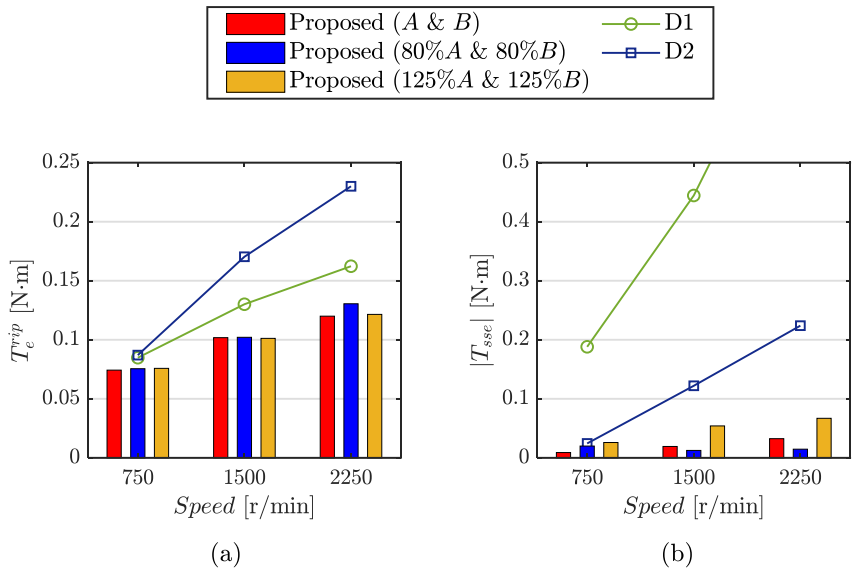

Figure 5.19: Quantitative evaluations of the torque performance for the proposed DTC method at different control parameters (A and B). (a) torque ripple. (b) steady-state torque error.

at different values of A and B when the machine runs at 2250-r/min speed and a load of 1.8 N·m. For comparison, the torque ripple and steady-state error are numerically evaluated under different operating speeds, as shown in Fig. 5.19.

In Fig. 5.19, it can be noticed that decreasing both A and B by 20% increases the torque ripple slightly by an average of 5%. However, this causes an 11% less steady-state torque error than that with the accurate values of A and B. When theses control coefficients are increased to 125% of their original rates, both the ripple and steady-state error of torque rises,

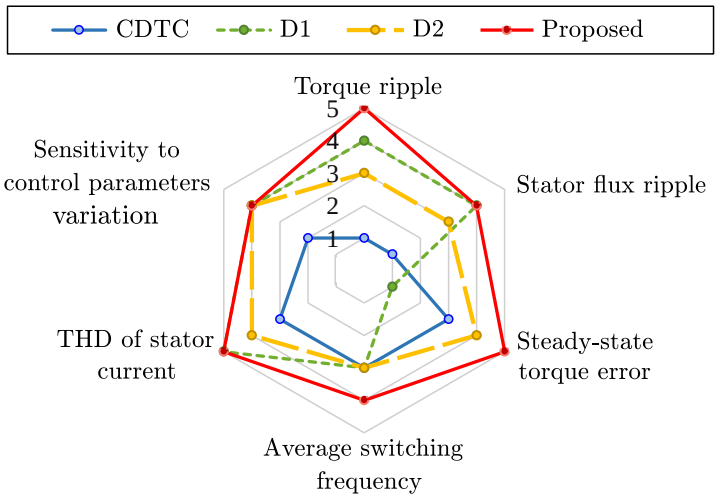

Figure 5.20: Summary of the comparative investigation of different direct torque control methods.

which are less than those of both D1 and D2, as shown in Fig. 5.19. Thus, it can be stated that the proposed method is robust for a wide range of the control parameters.

A summary of the comparative evaluation for the four DTC approaches in terms of different performance indices is presented in Fig. 5.20. The superiority of a particular method for a particular performance index is ranked on a scale of 1 to 5. Point 5 indicates the highest superiority, whereas 1 shows the least superiority. This comparison is indicated and measured in relative based on the experimental results presented in this chapter.

5.7 Chapter Summary

This chapter presented an advanced DRR-based DTC strategy for a three-phase PMSM-based drive system to improve the torque performance in terms of ripple and steady-state error. Unlike the existing DRR-based DTC approaches, the proposed method uses the duty-ratio regulation not

only to control the working duration of the AVVs but also to give the highest priority for selecting those of them that cause low torque deviations under the steady-state conditions, achieving further torque ripple reduction. Meanwhile, it guarantees a fast dynamic response, even during speed reversal, as it allows the selection of the AVVs that produce high torque deviations with a duty period proportional to the absolute value of the torque error.

Moreover, a virtual reference generator is employed to modify the original reference torque and optimize the duty-ratio calculation, which effectively mitigates the small torque offset caused by the duty regulator and minimizes the torque ripple. The effectiveness of the proposed strategy is confirmed through a detailed comparative evaluation with the CDTC and two existing DRR-based DTC approaches. The proposed method shows a higher reduction of both torque ripple and torque steady-state error than that of the traditional DRR-based DTC strategies while reserving the simplicity and robustness of the CDTC method.

However, the proposed scheme replaces the selected AVV according to the angular position of the stator flux to avoid degradation of the flux ripple and current distortion. As a result, the optimal voltage vector selection cannot be guaranteed from the viewpoint of the flux control performance. To overcome this issue, the cost function optimization of the M2PTFC can be a feasible solution if the proposed strategy is extended to reduce the computational complexity and eliminate the need for the weighting factor, as will be discussed in Chapter 6.

Chapter 6

Complexity Reduction for Model Predictive Torque and Flux Control of PMSM Drives

6.1 Chapter Overview

In this chapter, a low-complexity modulated model predictive torque and flux control (M2PTFC) technique is proposed to guarantee the selection of the optimal voltage vector that considers both the torque and flux control performances of 2L-VSI-fed PMSM. The proposed strategy aims to achieve that while reducing the computation burden and simplifying the control implementation of the conventional M2PTFC scheme by reducing the number of candidate voltage vectors at every control sample to the minimum (i.e., only two candidates) and eliminating the weighting factor of the cost function and its corresponding tuning procedures. For these purposes, the proposed method devotes different control objectives to the duty-modulation and the cost-function-evaluation processes while execut-

ing them sequentially. First, aiming at the torque-ripple reduction, a duty modulation strategy is proposed based on the analysis of the torque deviations produced by different voltage vectors, which ensures proper selection of the two candidates and restricts the active voltage vectors that cause high deviations. Then, these candidates are evaluated based on a cost function assigned to achieve the stator-flux control objective. The proposed method can be used to mitigate the torque ripple of the IPMSM drives when employed with a high-accuracy prediction model. The effectiveness of the proposed control scheme is verified through a comparative assessment with the conventional M2PTFC and two existing simplified methods by means of simulation and experimental results.

The rest of this chapter is structured as follows. Section 6.2 discusses the control set effects on the control variables and how it can be reduced. Section 6.3 presents an explanation for the proposed M2PTFC method. In Section 6.4, the proposed approach is theoretically compared with several MPTFC schemes reported in the literature. The simulation results and experimental verification are presented in Sections 6.5 and 6.6, respectively. Finally, the chapter summary is presented in Section 6.7.

6.2 Control Set Effects on Torque and Flux

The computation burden of the MPTFC algorithm is greatly affected by the number of voltage vectors included in the control set. Hence, for control-set reduction, the impact of different voltage vectors on the torque and the stator-flux amplitude will be analyzed in this section.

According to the discussion presented in the previous chapters, the lower the torque deviation is, the lower the torque ripple will be. There-

fore, a set of three voltage vectors for each rotation direction can be used to control T_e with minimum ripple during steady-state operation [45], as follows:

$$\begin{cases} \text{Set I} : \{\mathbf{V}_{x+1}, \mathbf{V}_{x+2}, \text{ZVV}\} & \text{for forward rotation} \\ \text{Set II} : \{\mathbf{V}_{x+5}, \mathbf{V}_{x+4}, \text{ZVV}\} & \text{for backward rotation,} \end{cases} \tag{6.1}$$

which can also satisfy the stator-flux control because the AVVs included in each set can produce either positive or negative deviations in ψ_s, as shown in Fig. 4.4.

It should be noted that $\mathbf{V}_x$ and $\mathbf{V}_{x+3}$ show ambiguous impact on the torque within each sector, as shown in Figs. 4.3(e) and 4.3(f). It can be observed that $\mathbf{V}_x$ produces +ve torque deviations within a specific range of θ_s, and vice versa for $\mathbf{V}_{x+3}$. Thus, there is a possibility to include $\mathbf{V}_x$ in Set I and $\mathbf{V}_{x+3}$ in Set II (6.1). However, this is unnecessary because $\mathbf{V}_{x+1}$ and $\mathbf{V}_{x+4}$ can provide the required performance. To clarify, the torque deviations produced by $\mathbf{V}_x$ and $\mathbf{V}_{x+1}$ are compared at different operating conditions, as shown in Fig. 6.1. Unlike $\mathbf{V}_{x+1}$, $\mathbf{V}_x$ can produce low $+\Delta T_e$ only at low speed within a small range of θ_s. Also, because ΔT_e produced

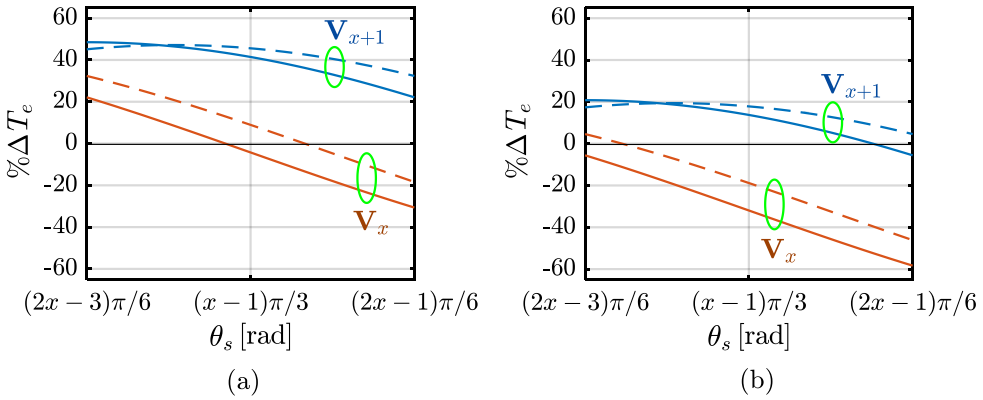

Figure 6.1: Percentage torque deviation produced by $\mathbf{V}_x$ and $\mathbf{V}_{x+1}$. (a) at 10% of rated speed and (b) at 75% of rated speed. [solid line: no load, dashed line: full load]

by $\mathbf{V}_x$ is lower than that of $\mathbf{V}_{x+1}$, the former need to be applied for longer working period. Since $\mathbf{V}_x$ produces the highest flux deviations, as shown in Fig. 4.4, $\mathbf{V}_{x+1}$ always has higher priority to be selected in the conventional M2PTFC than $\mathbf{V}_x$ under either steady or transient states. Therefore, it can be concluded that discarding both $\mathbf{V}_x$ and $\mathbf{V}_{x+3}$ from the feasible set of voltage vectors will affect neither the steady-state nor the dynamic performances of the conventional method, as will be confirmed by the results presented in Sections 6.5 and 6.6.

As a result, the number of voltage vectors included in the control set is reduced from eight to three. This number can be further decreased to only two voltage vectors with a further torque-ripple reduction if a ZVV is combined with an AVV during the control sample using a duty-ratio modulator (DRM). However, to maintain the fast dynamic response of the conventional M2PTFC, the AVVs that produce high torque deviations have to be employed. In other words, during system dynamics, $\mathbf{V}_{x+4}$ and $\mathbf{V}_{x+5}$ are better choices to decrease the torque faster than the ZVVs in +ve speed, and similarly for $\mathbf{V}_{x+1}$ and $\mathbf{V}_{x+2}$ in the other rotation direction. Therefore, this work proposes a modified M2PTFC strategy based on DRM that can inherently employ a proper ZVV with an AVV selected among only two candidates at every control sample, ensuring computation-burden reduction with the minimum steady-state torque ripple while maintaining rapid dynamic response.

6.3 A Low-Complexity M2PTFC Method

The control structure of the proposed M2PTFC is presented in Fig. 6.2, which consists of two main processes: DRM with control-set reduction

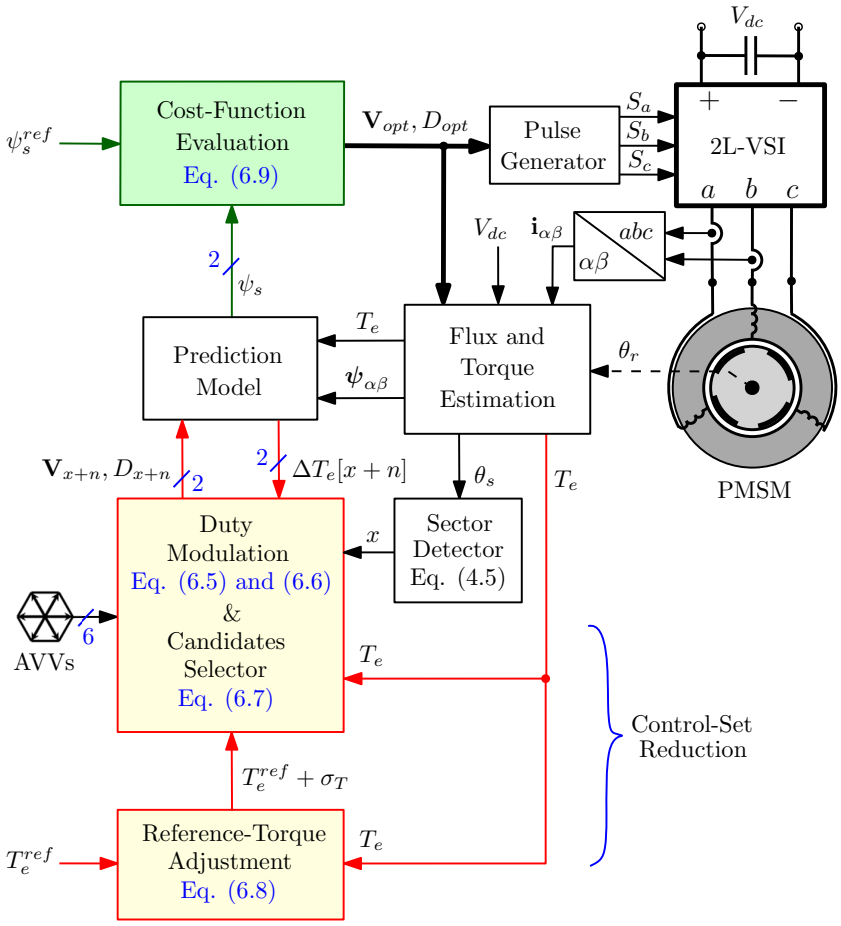

Figure 6.2: Control block diagram of the proposed M2PTFC scheme.

and cost-function evaluation. It dedicates each process to satisfy a single control objective. The DRM considers torque-ripple minimization, while the cost-function evaluation considers the stator-flux control.

6.3.1 Duty-Ratio Modulation

The proposed method combines an AVV and ZVV at every control cycle. When the AVV is applied for a time period DT_s then switched to a ZVV, the torque response will be as shown in Fig. 6.3. It can be deduced from Fig. 6.3 that the duty cycle D_{x+n}^k that maintains the torque ripple within

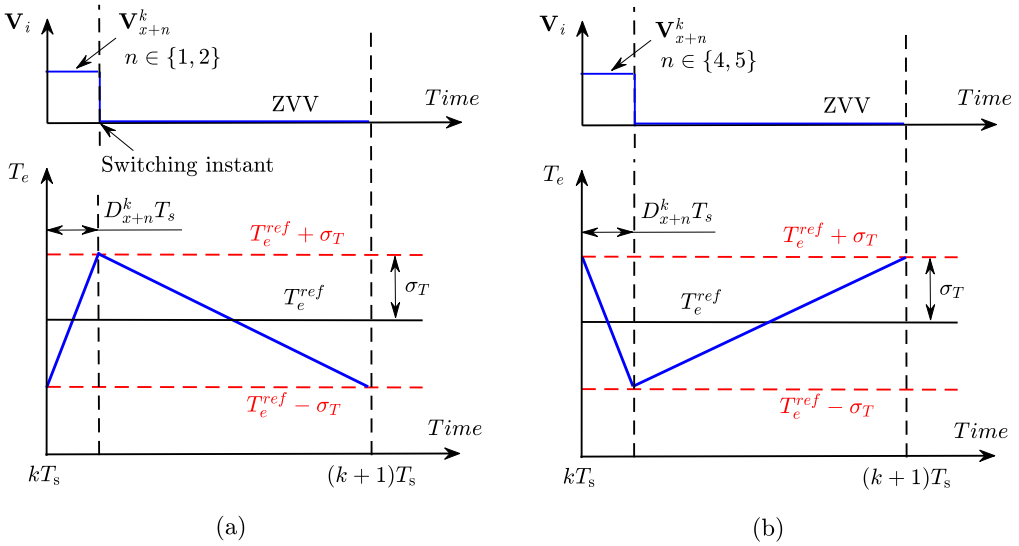

Figure 6.3: Principle of the duty-ratio modulation for the different operation modes. (a) Forward, (b) Backward.

the boundaries $T_e^{ref} \pm \sigma_T$ is defined as [137]:

$$D^k_{x+n} = \frac{T_e^{ref} - \sigma_T - T_e^k - \Delta T_e^k\,[0]}{\Delta T_e^k\,[x+n] - T_e^k\,[0]}, \quad D^k_{x+n} \in [0,1], \tag{6.2}$$

To simplify (6.2), the required prediction of $\Delta T_e^k\,[0]$ needs to be omitted. Thus, the relation between ΔT_e^k and σ_T is obtained as:

$$\Delta T_e^k\,[0] = \frac{-2\sigma_T^k \cdot \Delta T_e^k\,[x+n]}{\Delta T_e^k\,[x+n] - 2\sigma_T^k}\ . \tag{6.3}$$

Assuming that $\left|\Delta T_e^k\,[x+n]\right| \gg \left|\sigma_T^k\right|$ yields,

$$\Delta T_e^k\,[0] \cong -2\sigma_T^k\ . \tag{6.4}$$

Substituting into (6.2), the duty cycle can be calculated as:

$$D^k_{x+n} = \frac{(T_e^{ref} + \sigma_T^k) - T_e^k}{\Delta T_e^k\,[x+n] + 2\sigma_T^k}\ . \tag{6.5}$$

It should be noted that, under high-speed and loading conditions, the torque deviations produced by $\mathbf{V}_{x+2}$ and $\mathbf{V}_{x+4}$ reverse (see Fig. 4.3), re-

sulting in a negative D_{x+n}, according to (6.5). With such a situation, the conventional DRM-based methods [32] force the duty ratio to be zero, i.e., apply a ZVV for the whole control cycle. However, because the absolute values of the torque deviations produced by $\mathbf{V}_{x+2}$ and $\mathbf{V}_{x+4}$ are less than those of ZVV, the proposed method employs the AVV instead, using the following constraint:

$$D_{x+n}^{k} = \begin{cases} D_{x+n}^{k}, & \text{if } 0 \leq D_{x+n}^{k} \leq 1 \\ 1, & \text{otherwise.} \end{cases} \tag{6.6}$$

6.3.2 Control-Set Reduction

6.3.2.1 Candidate voltage-vectors selector

Thanks to (6.5), it is guaranteed that $\left|T_e^k\right.$ will never exceed $\left|T_e^{ref} + \sigma_T^k\right|$, regardless the rotation directions. Consequently, the upper boundary of the demanded torque $(T_e^{ref} + \sigma_T^k)$ can be employed to select the two-candidate AVVs using the following expression:

$$\mathbf{V}_{x+n}^{k} \in \begin{cases} \{\mathbf{V}_{x+1}, \mathbf{V}_{x+2}\}, & \text{if } (T_e^{ref} + \sigma_T^k) \geq T_e^k \\ \{\mathbf{V}_{x+4}, \mathbf{V}_{x+5}\}, & \text{if } (T_e^{ref} + \sigma_T^k) < T_e^k. \end{cases} \tag{6.7}$$

In this way, the proposed method needs to determine the duty ratio for only two AVVs using (6.5), minimizing the computations needed for the torque predictions. Also, it allows selection of the AVVs that produce high torque deviation during torque transients, providing good dynamic performance. As an illustration, Fig. 6.4 shows the AVV selection when a torque decrease is demanded at the kth-sampling instant for both rotation directions. Either $\mathbf{V}_{x+4}$ or $\mathbf{V}_{x+5}$ will be employed to decrease the torque

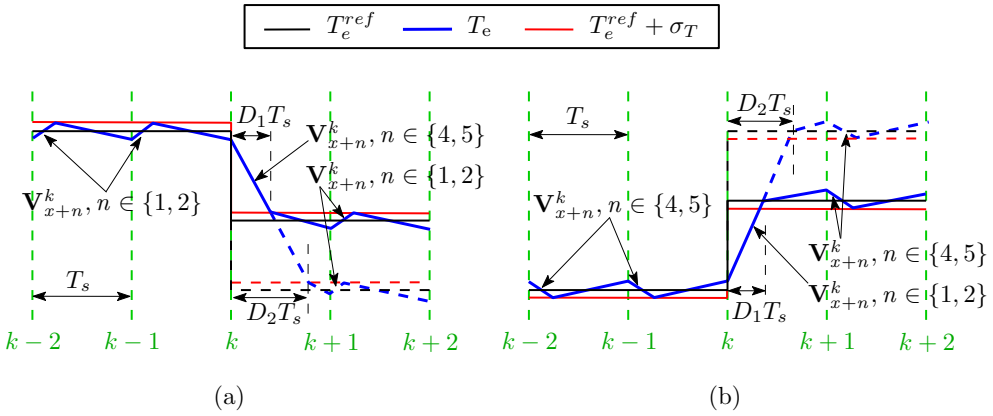

Figure 6.4: AVV selection of the proposed strategy under torque dynamics for both rotation directions: (a) Forward, and (b) Backward.

in the forward rotation, while $\mathbf{V}_{x+1}$ or $\mathbf{V}_{x+2}$ will do the same job during backward rotation. Referring to (6.5), the operating period of the AVV depends on the torque error. Hence, the higher the change in the demanded torque, the higher the duty cycle will be ($D_2 > D_1$), as shown in Fig. 6.4.

As for the candidate ZVVs, they are selected based on the AVV to minimize the switching frequency. Hence, $\mathbf{V}_1$, $\mathbf{V}_3$, and $\mathbf{V}_5$ are followed by $\mathbf{V}_0$, while $\mathbf{V}_7$ follows the remaining AVVs, avoiding the unnecessary switching jumps.

6.3.2.2 Reference-torque adjustment

For the candidate-vectors selection and duty calculation, the reference torque needs to be adjusted by the offset value σ_T. This value can be determined based on the filtered difference between T_e^{ref} and the estimated torque T_e using a low-pass filter (LPF), as presented in 5.3.2, which can be expressed as follows:

$$\sigma_T^k = \lambda(T_e^{ref} - T_e^k) + (1-\lambda)\,\sigma_T^{k-1}, \tag{6.8}$$

6.3.3 Cost-Function Design

Because the torque-control objective can be satisfied by the duty modulation, the cost function can consider the stator-flux control only. As a result, the weighting factor needed to tune the importance of the control objectives in the traditional cost function is eliminated. The cost function of the proposed method is given by:

$$g_{x+n}^{k} = \left|\psi_s^{ref} - \psi_s^{k+1}[x+n]\right|, \tag{6.9}$$

where $\psi_s^{k+1}[x+n]$ is the predicted stator-flux amplitude if $\mathbf{V}_{x+n}$ is applied for a period of $D_{x+n}T_s$. This cost function evaluates the two-candidate AVVs and their corresponding duty ratios, and those of them that gives the minimum g_{x+n} are delivered to the load.

6.3.4 Implementation Steps of M2PTFC Strategy

The flowchart illustrated by Fig. 6.5 shows the implementation stages of the proposed approach, which mainly includes torque and flux estimation, DRM with control-set reduction, and cost-function evaluation. Because the data processing of the control algorithm is not instantaneous, delay compensation should be performed by predicting the control variables one step further [138]. Hence, in the proposed method, the torque and flux at the $(k+2)$th instant are applied for the control-set reduction and cost-function evaluation.

Based on the measured states of the machine at the sampling instant kT_s, the stator flux can be estimated using either the current or voltage model or the closed-loop observer [71, 74]. Since the observer does not

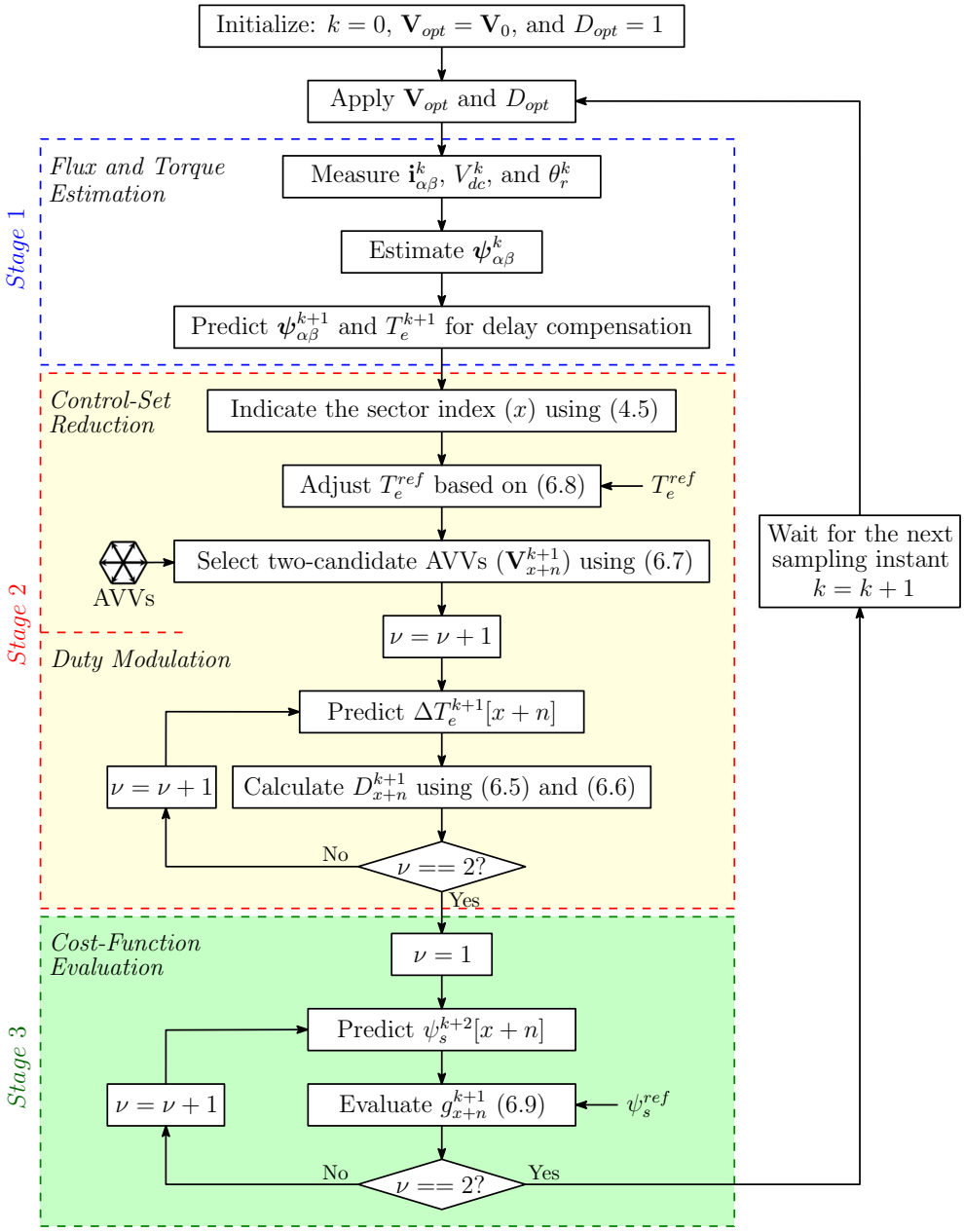

Figure 6.5: Flowchart of the proposed M2PTFC strategy.

constitute the main focus of the paper, the current model (3.4) is utilized in this work for $\boldsymbol{\psi}^k_{\alpha\beta}$ estimation for the sake of simplicity. Then, $\boldsymbol{\psi}^{k+1}_{\alpha\beta}$ and T^{k+1}_e are obtained by substituting the applied voltage at the kth sample into the discretized form of the PMSM model, as

$$\boldsymbol{\psi}^{k+1}_{\alpha\beta}[i] = \boldsymbol{\psi}^k_{\alpha\beta} + T_s\mathbf{V}_i - T_s\mathbf{i}^k_{\alpha\beta}R_s \tag{6.10}$$

and

$$T_e^{k+1}[i] = \frac{3p}{2}\left(\boldsymbol{\psi}_{\alpha\beta}^{k+1}[i] \times \mathbf{i}_{\alpha\beta}^{k+1}[i]\right) \tag{6.11}$$

where

$$\mathbf{i}_{\alpha\beta}^{k+1}[i] = \frac{1}{L_s}\left(\boldsymbol{\psi}_{\alpha\beta}^{k+1}[i] - \psi_{pm} e^{j\left(\theta_r^k + \omega_r^k T_s\right)}\right). \tag{6.12}$$

After that, the control-set-reduction stage starts with indicating x and adjusting T_e^{ref} based on (4.5) and (6.8), respectively, to decide the two-candidate AVVs $\mathbf{V}_{x+n}^{k+1}$ using (6.7). For each candidate, T_e^{k+2} is determined from (6.10) and (6.11) after replacing the kth and $(k+1)$th variables with the $(k+1)$th and $(k+2)$th variables, respectively. The prediction of D_{x+n}^{k+1} is subsequently executed according to (6.5) and (6.6). Finally, based on D_{x+n}^{k+1} and $\mathbf{V}_{x+n}^{k+1}$, the stator flux amplitude $\psi_s^{k+2}[x+n]$ is obtained for the evaluation of the cost function (6.9). The optimal AVV ($\mathbf{V}_{opt}$) with its duty cycle (D_{opt}), which achieves the minimum g_{x+n}^{k+1}, will be applied at the beginning of the future control interval.

6.4 Theoretical Comparison with Existing MPTFC Schemes

To highlight the differences between the proposed M2PTFC method and the existing approaches, a comparison of them is presented in this section, which is summarized in Table 6.1.

6.4.1 Comparison with Simplified MPTFC Strategies

These strategies imply simplifying the control implementation by eliminating the need for the weighting factor (ζ) of the conventional cost function

Table 6.1: Theoretical comparison between different MPTFC methods

Comparison indices		**Control methods**							
		[112], [139]	[40]	[44]	[45]	[46]	[47]	[123]	[124]	Proposed
Number of candidate voltage vectors		7	7	7	3	5	7	5 ($y = 4$)	3	2
Number of T_e predictions	for duty modulation	-	-	-	-	-	7	1	3	2
	for cost-function evaluation	7	7	7	3	-	6	4	2	-
Number of $\boldsymbol{\psi}_{\alpha\beta}$ predictions	for duty modulation	-	-	-	-	-	7	1	3	2
	for cost-function evaluation	7	2	7	3	5	6	4	2	2
Reference flux derivation		No	No	No	No	Yes	No	No	No	No
Need for a weighting factor		Yes	No	No	Yes	No	Yes	Yes (ε_ψ)	Yes	No
Sector detector		No	No	No	Yes	No	No	Yes	Yes	Yes
Performance under the same T_s	Torque ripple	High	High	High	High	High	Low	Low	Moderate	Low
	Flux ripple	High	High	High	High	High	Low	Moderate	Moderate	Low

expressed as:

$$g_i = \left|T_e^{ref} - T_e^{k+1}[i]\right| + \zeta \left|\psi_s^{ref} - \psi_s^{k+1}[i]\right|. \tag{6.13}$$

In [40] and [44], the torque-and flux-control objectives of (6.13) are separated into two cost functions. The torque predictions of all voltage vectors are first evaluated using $\left|T_e^{ref} - T_e^{k+1}[i]\right|$ to select a group of candidate voltage vectors. Then, among this group, the optimal vector that minimize $\left|\psi_s^{ref} - \psi_s^{k+1}[i]\right|$ is delivered to the load. Because all the voltage vectors need to be assessed by either or both cost functions in [40] and [44], the computational effort is heavier than that of the proposed method. In [42], the voltage vectors are sorted into three groups according to predefined constraints for each cost function to select the mutual. However, no more discussion is given to consider the computation complexity or the torque-ripple reduction.

The method [45] has reduced the computation burden by reducing the number of voltage vectors in the control set. It chooses one set of three voltage vectors (6.1), according to the torque-error sign. These vectors are then used for torque and flux predictions that need to be evaluated by (6.13). In [46], four vectors are selected based on the voltage vector applied in the previous control cycle. The control set of both methods (i.e., [45] and [46]) includes a higher number of voltage vectors than the proposed method and allows employing those of them that produce high torque deviations during steady-state operation, resulting in higher torque pulsations. Also, in [46, 140–142], the control set is assessed based on the stator-flux-vector error by the cost function expressed as:

$$g_i = \left|\boldsymbol{\psi}_{\alpha\beta}^{ref} - \boldsymbol{\psi}_{\alpha\beta}^{k+1}[i]\right|, \tag{6.14}$$

where ($\boldsymbol{\psi}_{\alpha\beta}^{ref} = \psi_s^{ref} e^{j\theta_s^{ref}}$) is the reference stator-flux vector obtained from the reference torque based on the principle of MTPA (4.15)-(4.17). Although the derivations of the relationship between the reference signals remove the weighting factor of the cost function, they increase the system complexity, especially in IPMSM drives [71], which is avoided in the proposed method. Moreover, the simplified MPTFC strategies employ one voltage vector for the whole control cycle, causing a higher torque ripple than those that utilize the modulation concept.

6.4.2 Comparison with Existing M2PTFC Methods

These approaches concern the torque-ripple reduction by controlling the duty cycle of the AVV. In the conventional M2PTFC [47], the duty ratio is optimized for all the AVVs to minimize the final values of torque error using D_f (5.18). Then, all the voltage vectors and their duties are used for the predictions needed for (6.13), resulting in better steady-state performance than MPTFC methods with a high computation burden. According to the analysis presented in 4.3, the AVV and ZVV combined by this approach at every control cycle need to produce opposite torque deviations to achieve (5.18). Thus, by artificially restricting the AVVs that violate this condition in the proposed method, the computation complexity is significantly reduced without deteriorating the steady-state performance. Moreover, the proposed strategy avoids the unnecessary involvement of the torque error in both processes of duty optimization and cost-function evaluation, eliminating the need for a weighting factor.

In [124], a similar duty controller is employed for a group of three voltage vectors chosen by (6.1) based on the torque-error sign, which reduces the computation complexity of [47] at the cost of a higher torque ripple.

A discrete duty controller (DDC) has been proposed in [123] to synthesize a number of candidate voltage vectors (y) using an AVV that is selected from a switching table depending on the predictions of the torque and flux produced by ZVV. Despite the simplified voltage-vector selection, this DDC leads to suboptimal duty-ratio calculation because it depends on y, according to the following expression:

$$D_\nu = \frac{\nu}{y}, \quad \nu = \{0, 1, .., y\}\,. \tag{6.15}$$

Moreover, the flux term of the cost function (6.13) is replaced by a hard constraint (φ), as follows:

$$g_\nu = \left|T_e^{ref} - T_e^{k+1}[\nu]\right| + \varphi[\nu] \tag{6.16}$$

where

$$\varphi[\nu] = \begin{cases} 0, & \text{if } (\psi_s^{ref} - \varepsilon_\psi) \leq \psi_s^{k+1}[\nu] \leq (\psi_s^{ref} + \varepsilon_\psi) \\ \infty, & \text{otherwise,} \end{cases} \tag{6.17}$$

where ε_ψ is the hysteresis limit of the stator-flux amplitude. In (6.16), the weighting factor is replaced by ε_ψ that requires an optimization to get its best value.

Fig. 6.6 shows the flowchart for the second and third stages of the M2PTFC methods presented in [47], [123], and [124] to illustrate the differences between them and the proposed strategy depicted in Fig. 6.5.

Table 6.1 summarizes the comparison between different MPTFC methods, showing that the proposed method achieves a considerable reduction in the number of torque and flux predictions, and eliminates the need for a weighting factor.

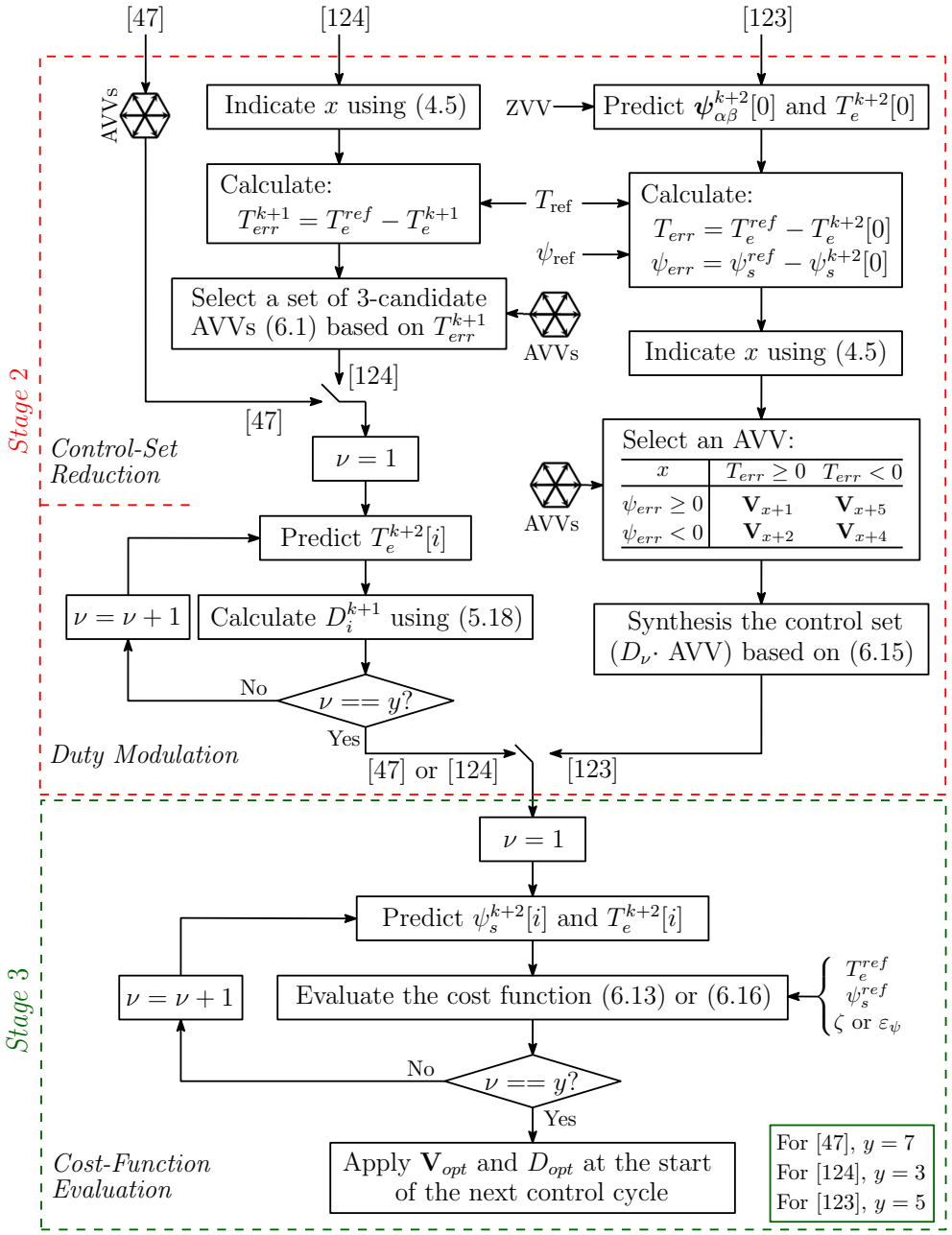

Figure 6.6: Flowchart of the M2PTFC methods presented in [47], [123], and [124].

6.5 Simulation Results

The theoretical analysis and the assumptions of the control-set reduction discussed in 6.2 consider a SPMSM, ignoring the magnetic-saturation effects. Thus, in this section, simulations are performed to verify the proposed method through comparisons with the conventional M2PTFC scheme [47], particularly the second and third stages. For this purpose, the sim-

ulation system presented in 3.3 is employed while considering only the nonlinear current-flux characteristics of the IPMSM, i.e., θ_r is maintained at zero to exclude the spacial harmonics effects from the FE-based IPMSM model (as discussed in 3.2.3).

The steps used to execute the second and third stages of the M2PTFC schemes in the simulation can be described as follows. To get ΔT_e^k needed for the duty modulation, the flux $\boldsymbol{\psi}_{dq}^{k+1}$ is first obtained for each candidate voltage vector $\mathbf{V}_i$ at $(D_i = 1)$ using forward Euler approximation of (3.8), as follows:

$$\boldsymbol{\psi}_{dq}^{k+1} = \boldsymbol{\psi}_{dq}^{k} + D^k T_s \mathbf{v}_{dq}^{k} - T_s(R_s \mathbf{i}_{dq}^{k} + j\omega_r \boldsymbol{\psi}_{dq}^{k}), \tag{6.18}$$

where $\mathbf{v}_{dq}$ can be obtained from (4.4) as,

$$\mathbf{v}_{dq} = \mathbf{V}_i \; e^{-j\theta_r}. \tag{6.19}$$

Then, the current vector $\mathbf{i}_{dq}^{k+1}$ is predicted from the inversed flux maps as $i_d^{k+1}(\psi_d^{k+1}, \psi_q^{k+1})$ and $i_q^{k+1}(\psi_d^{k+1}, \psi_q^{k+1})$. Substituting $\boldsymbol{\psi}_{dq}^{k+1}$ and $\mathbf{i}_{dq}^{k+1}$ into (3.10), T_e^{k+1} and $(\Delta T_e^k = T_e^{k+1} - T_e^k)$ can be successively obtained. To calculate the torque and flux needed for the cost-function evaluation, similar steps can be followed while using D_i obtained for each candidate vector.

In the simulation, the machine is driven in torque control mode with a variable speed source. The DC-link voltage and the sampling frequency are set to 540 Volt and 20 kHz, respectively. The reference flux amplitude is kept at 0.1837 Wb, and the weighting factor ζ of (6.13) is maintained at 2133 for equal importance of the control objectives.

Figs. 6.7 and 6.8 compare the steady-state performances of the proposed method and the conventional scheme under two different speeds (750

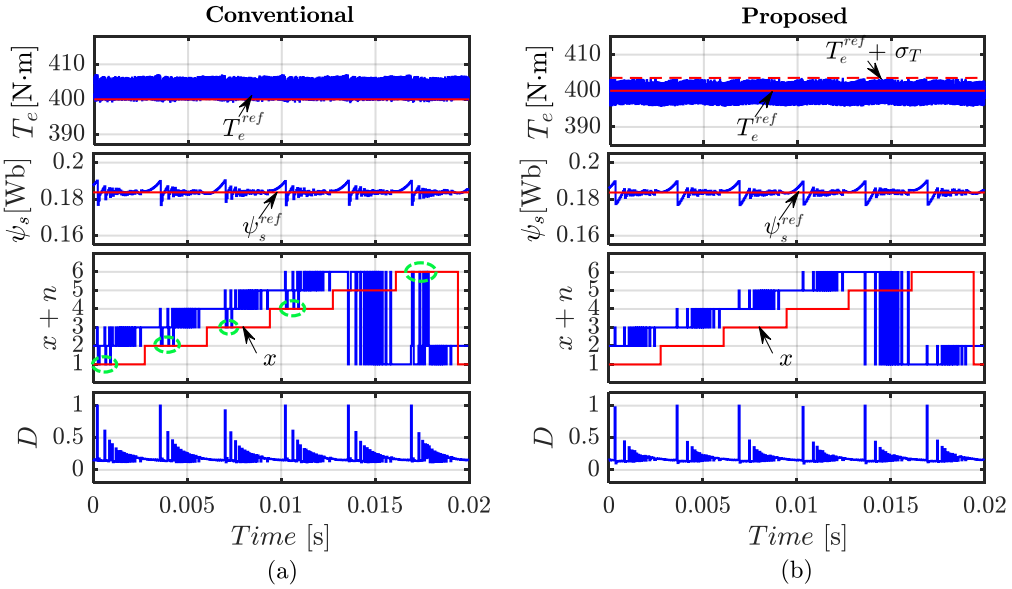

Figure 6.7: Simulation results of the steady-state-performance comparison at 750 r/min. (a) Conventional scheme. (b) Proposed method.

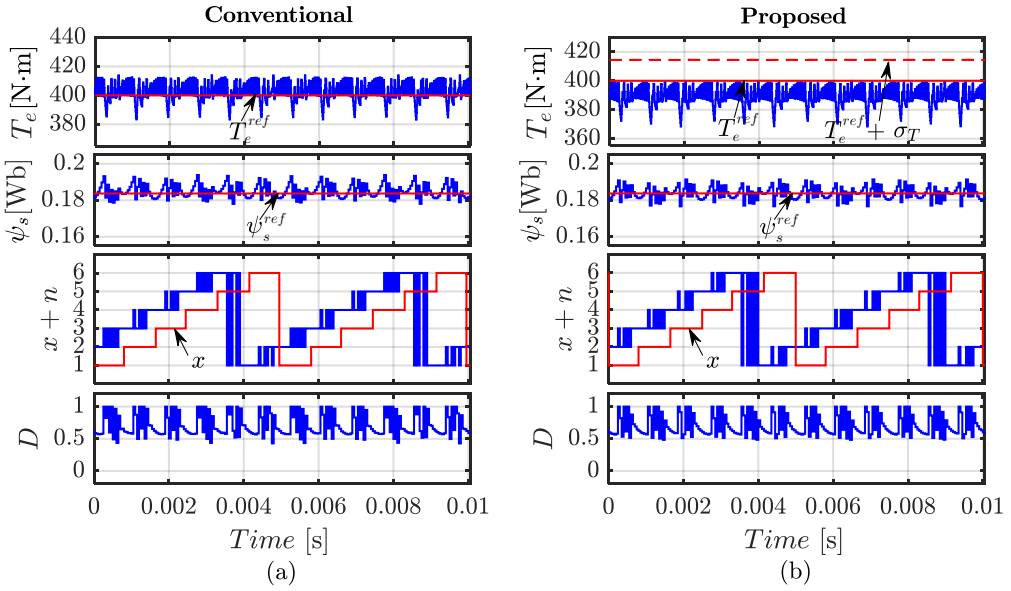

Figure 6.8: Simulation results of the steady-state-performance comparison at 3000 r/min. (a) Conventional scheme. (b) Proposed method.

and 3000 r/min) at the rated torque (400 N·m). At low speed (750 r/min), although the conventional method employs $\mathbf{V}_x$ (circled in Fig. 6.7(a)), discarding this voltage vector by the proposed method has almost no impact on the torque and flux ripples, as shown in Fig. 6.7(b). At high speed (3000 r/min), both methods select $\mathbf{V}_{x+1}$ and $\mathbf{V}_{x+2}$ as the optimal voltage vectors, as shown in Fig. 6.8.

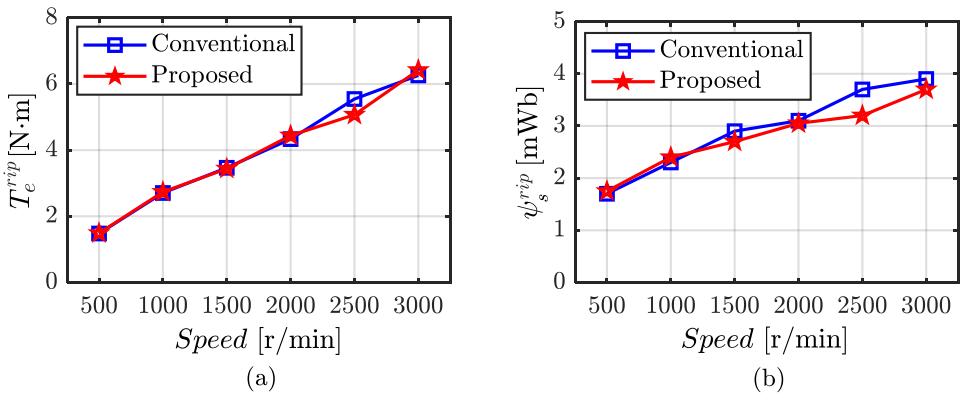

Figure 6.9: Quantitative comparison between the conventional and proposed methods under different speeds. (a) Torque ripple. (b) Flux ripple.

A quantitative evaluation for the torque and flux ripples of the two control strategies at different operating speeds is given in Fig. 6.9. It can be noticed that there are insignificant differences between the torque ripple produced by both control methods. Also, the proposed method provides a slight flux-ripple reduction by an average of 7% compared with the conventional approach. These results confirm the feasibility of the proposed strategy during steady-state operation.

Under torque dynamics, the optimal AVV is applied for longer periods to achieve the fastest possible torque response. Hence, as $\mathbf{V}_x$ is not selected at high speed during steady-state operation [see Fig. 6.8(a)], it will be expelled by the cost function at dynamic state due to the high flux deviations it produces. Therefore, the proposed M2PTFC maintains the fast dynamic response of the conventional method at high speed.

On the other hand, $\mathbf{V}_x$ is often employed in the first half of each sector at low speed, as can be observed in Fig. 6.7(a). Thus, the torque dynamic performance is tested at 750 r/min with a 50-N·m torque step, as shown in Fig. 6.10. This torque step is intentionally triggered at $\theta_s = -25$ (electrical degrees), i.e., at the first half of sector "$x = 1$". From Fig. 6.10, it can be noticed that both control methods employ $\mathbf{V}_{x+1}$ ($\mathbf{V}_2$)

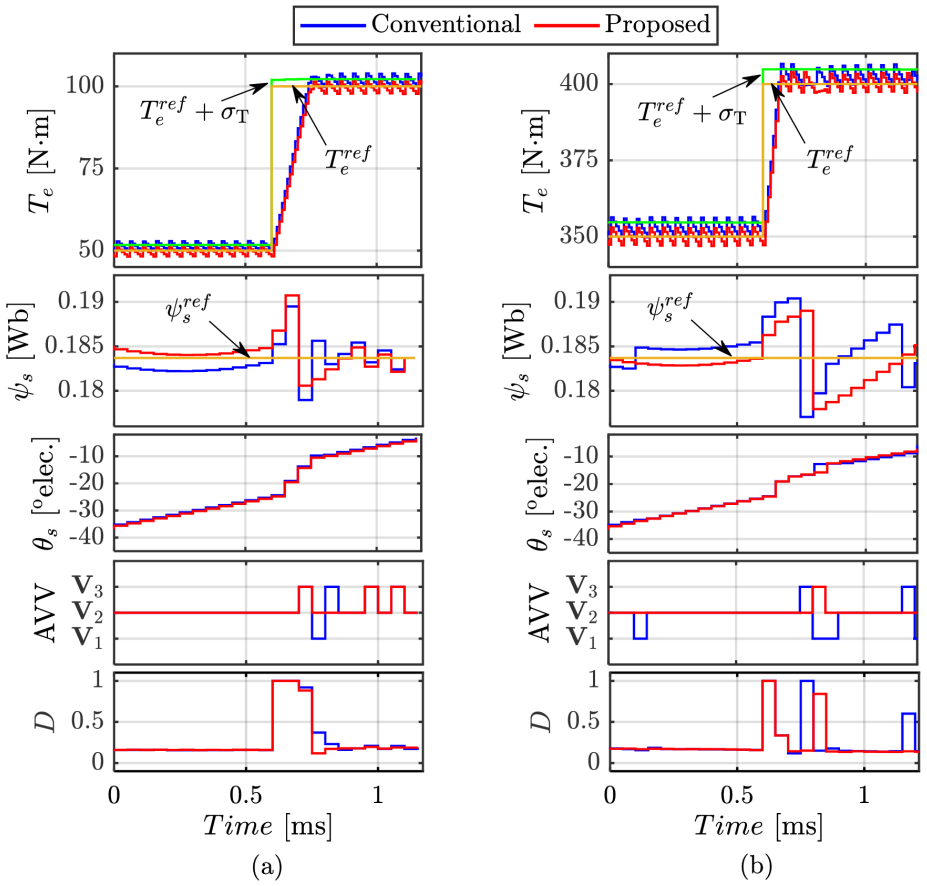

Figure 6.10: Simulation results of the dynamic-performance comparison with 50-N·m torque step. (a) From 50 to 100 N·m. (b) From 350 to 400 N·m.

to increase the torque with a unity D, and $\mathbf{V}_x$ ($\mathbf{V}_1$) is employed by the conventional approach during steady state only. It can therefore be stated that the proposed strategy can simplify the control implementation without causing suboptimal steady-state or dynamic performances compared to the conventional approach.

6.5.1 A Case Study for Torque-Ripple Reduction of IPMSM

In this section, the proposed M2PTFC strategy assisted with the FE-based model for predictions is utilized to suppress the torque ripple of IPMSM drives. The high fidelity of the FE model guarantees avoiding the model-

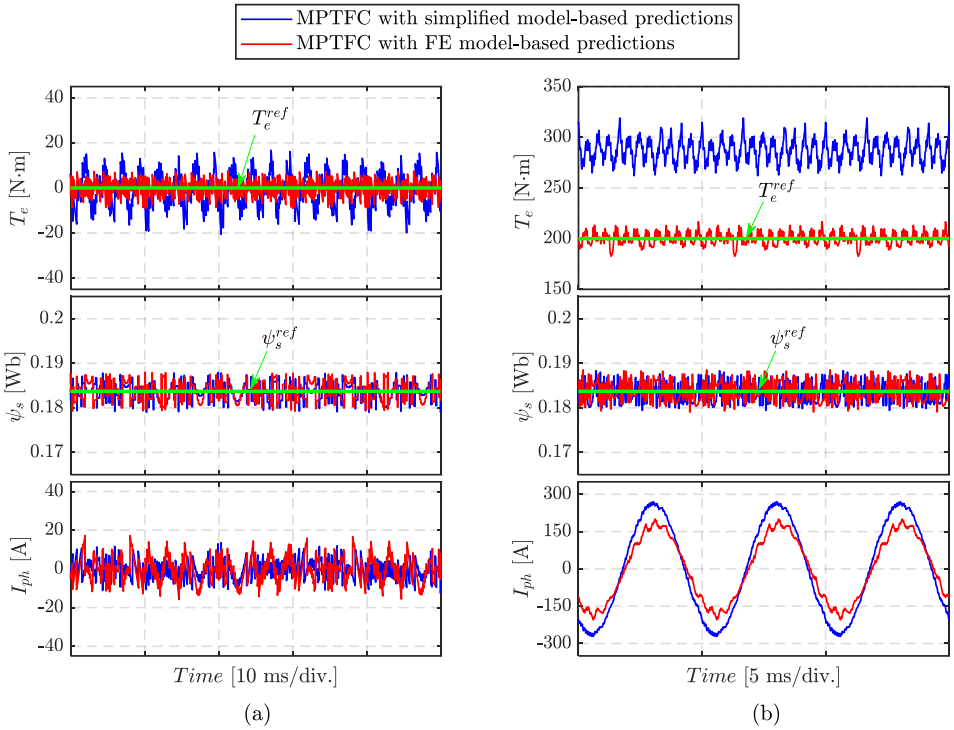

Figure 6.11: Comparison between the MPTFC performance when the simplified and FE models are employed for predictions. (a) 500 r/min and no load. (b) 3000 r/min and 200 N·m. [Simulation results at $T_s = 25$ μs]

machine mismatch that can degrade the control performance, and it allows the control-based mitigation of the cogging torque, saving cost and time. Fig. 6.11 compares the performance of MPTFC (without duty modulation) when the simplified (with constant parameters of $L_d = 0.6$ mH, and L_q= 1.33 mH) and FE-based models are employed for prediction under different operating conditions.

As can be noticed in Fig. 6.11, the FE model-based MPTFC reduces the torque ripple considerably for all operating conditions because the prediction can consider the electromagnetic variables of the machine accurately, including the cogging torque. On the other hand, the simplified model-based MPTFC shows a significant steady-state torque error (around 40%) under 200-N·m load because of the inaccurate current predictions using (3.8)-(3.10) that neglects the inductance variation with the magnetic

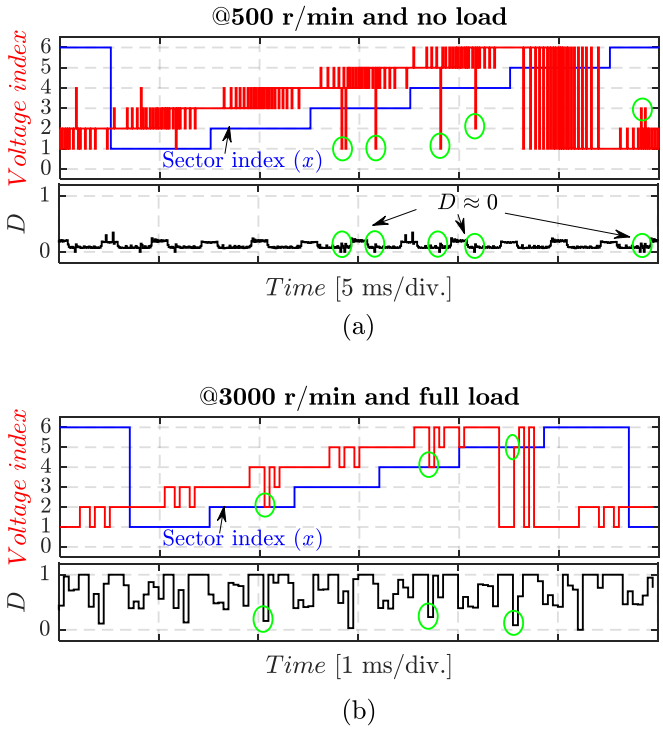

Figure 6.12: Voltage vector index and duty cycle selected by the conventional M2PTFC with the FE-based-model prediction. (a) 500 r/min and no load. (b) 3000 r/min and full load. [Simulation results at $T_s = 50$ μs]

saturation. These results verify that the FE model can be used for prediction in model-based control strategies to suppress the torque pulsation of IPMSM and improve the torque tracking performance.

The FE-based model prediction is also utilized in the conventional M2PTFC to validate the control-set reduction (Section 6.2). Fig. 6.12 illustrates the selected voltage vectors and their duties D at different speed and loading conditions. As can be noticed in Fig. 6.12, both $\mathbf{V}_{x+1}$ and $\mathbf{V}_{x+2}$ are the most frequently selected AVVs under all operating conditions. Even if other vectors are chosen (circled in Fig. 6.12), their duties are negligible ($D \approx 0$), i.e., a ZVV is employed for the entire control sample. Similar patterns are detected when the machine rotates in the opposite direction, applying either $\mathbf{V}_{x+4}$ or $\mathbf{V}_{x+5}$. Therefore, the theoretical analysis presented in 6.2 for control set reduction is feasible even when the spacial harmonics

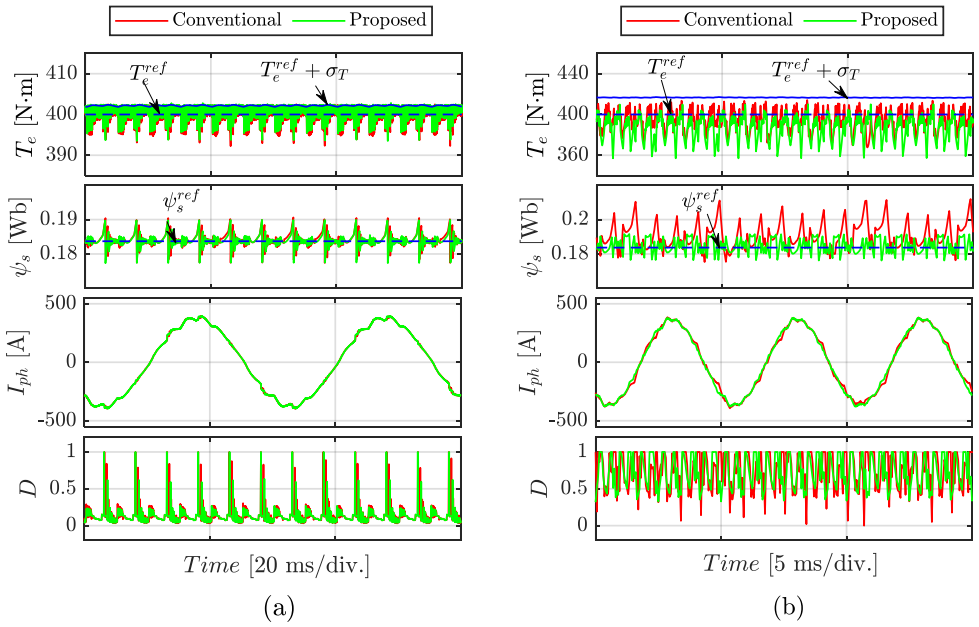

Figure 6.13: Steady-state performance of the proposed and conventional M2PTFC while employing FE-model for prediction at full load. (a) 500 r/min. (b) 3000 r/min. [Simulation results at $T_s = 50$ μs]

effects of the machine is taken into consideration.

Therefore, the proposed M2PTFC method assisted with FE-based prediction model can be used as a control-based torque ripple suppression technique for IPMSM. To verify that, the steady-state performance of the proposed M2PTFC is compared with that of the conventional method under different operating conditions, as shown in Fig. 6.13. In both methods, the flux and torque are predicted using (6.18), (3.14) and (3.12). From Fig. 6.13, there is insignificant difference between the two methods at low speed (500 r/min) in terms of torque ripple. However, at high speed (3000 r/min) the proposed method provides lower flux ripple than the conventional scheme, i.e., better balance between the flux and torque control performances under steady-state operation. These results confirm that the proposed method can be used for torque-ripple suppression of IPMSM, despite its reduced complexity, if the torque is accurately estimated using FE-based model.

6.6 Experimental Verification

In this section, the feasibility and effectiveness of the proposed strategy are experimentally tested through comparisons with the conventional M2PTFC scheme (M1 [47]) and two existing simplified methods (M2 [123] and M3 [124]) in terms of control complexity, steady-state behavior, and dynamic response. It should be noted that M1 is considered as a benchmark because it evaluates all the AVVs and their duty cycle, ensuring the optimal voltage-vector selection.

6.6.1 Comparison of Control Complexity

As a criterion of the control complexity, the execution time is directly measured by the ControlDesk of DS1202 (2 GHz). It includes the time of the code implementation of stages 1 to 3 illustrated by Figs. 6.5 and 6.6.

As shown in Fig. 6.14, the execution time is 6.96, 9.24, 4.8, and 4.6 μs for M1, M2, M3, and the proposed algorithm, respectively. It indicates that the computation effort of the proposed method is the lightest, which is 34%, 50%, and 4% less than those of M1, M2, and M3, respectively. This reduction is achieved owing to the simple DRM that reduces the control set to two voltage vectors before the prediction stage.

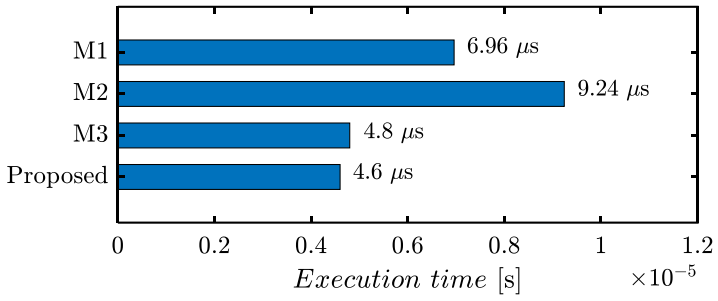

Figure 6.14: Execution time for stages 1-3 of M2PTFC algorithms.

Table 6.2: Control parameters of the four M2PTFC methods

Methods	Speed (r/min)	Control parameters
M1	750	$f_s = 10$ kHz, $\zeta = 250$ N·m/Wb
	2250	$f_s = 10$ kHz, $\zeta = 640$ N·m/Wb
M2	750	$f_s = 10$ kHz, $\varepsilon_\psi = 6.60$ mWb
	2250	$f_s = 10$ kHz, $\varepsilon_\psi = 9.42$ mWb
M3	750	$f_s = 12$ kHz, $\zeta = 440$ N·m/Wb
	2250	$f_s = 16$ kHz, $\zeta = 110$ N·m/Wb
Proposed	750	$f_s = 10$ kHz, $\lambda = 0.03$
	2250	$f_s = 11$ kHz, $\lambda = 0.03$

6.6.2 Comparison of Steady-State Performance

The steady-state performances are investigated under the four control algorithms at two different speeds (25% and 75% of the rated speed) and a constant load of around 1.8 N·m. Figs. 6.15 and 6.16 show the waveforms of torque, stator-flux amplitude, phase current (I_{ph}), index of the selected AVVs, duty ratio, and average switching frequency (f_{av}) from top to bottom. The control parameters (i.e., ζ, ε_ψ, and sampling frequency f_s) of the four tested strategies are presented in Table 6.2. They are chosen based on extensive experiments to satisfy good torque-and flux-control performances under approximately similar average switching frequencies. For quantitative comparison, the standard deviation is utilized to calculate the torque and flux ripples. Also, the total harmonic distortion (THD_I) of I_{ph} is calculated up to 10 kHz using the fast Fourier transform tool of MATLAB *powergui*.

At low speed (750 r/min), it can be noticed from Fig. 6.15 that M1 and the proposed method provide a roughly similar steady-state performance in terms of torque and flux ripples and current THD. Compared with M2 and M3, they achieve lower ripples in torque and flux and less current THD

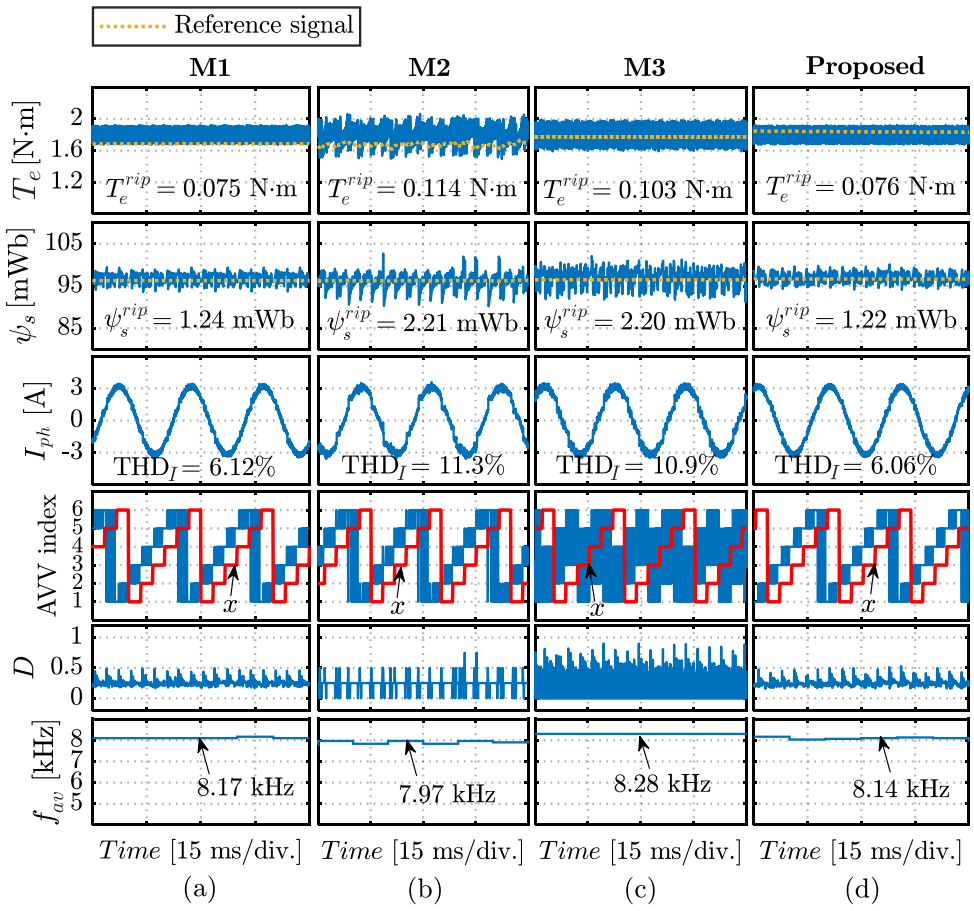

Figure 6.15: Steady-state waveforms of torque, stator-flux amplitude, stator phase current, index of the selected AVVs, duty ratio, and average switching frequency at 750 r/min and 1.8 N·m load. (a) M1, (b) M2, (c) M3, and (d) Proposed method.

by 29%, 43%, and 5% on average, respectively. Both methods select either $\mathbf{V}_{x+1}$ or $\mathbf{V}_{x+2}$ as the optimal AVVs during steady-state operation, confirming the theoretical analysis presented in 4.3 and proving the effectiveness of the proposed method despite the control-set reduction before the cost function evaluation. Although M2 can also select the optimal AVVs, the discrete nature of its duty modulator causes higher ripples in torque and flux and current distortions. On the other hand, M3 sometimes selects $\mathbf{V}_{x+4}$ or $\mathbf{V}_{x+5}$, as can be seen in Fig. 6.15(c). Because these two AVVs produce high negative torque deviations [see Fig. 4.3], the duty modulator of M3 set D to zero, applying a ZVV for the entire control period. As a result, M3 produces a higher torque ripple than both M1 and the proposed method as the ZVV generates higher absolute torque deviations

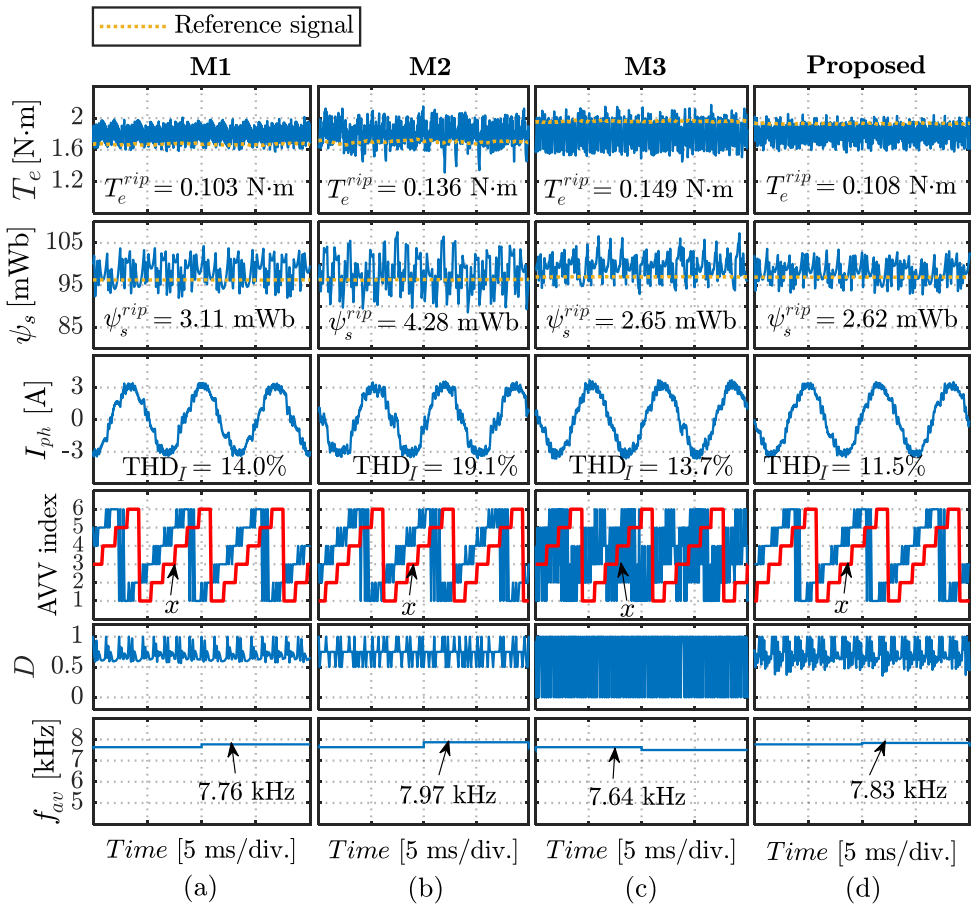

Figure 6.16: Steady-state waveforms of torque, stator-flux amplitude, stator phase current, index of the selected AVVs, duty ratio, and average switching frequency at 2250 r/min and 1.8 N·m load. (a) M1, (b) M2, (c) M3, and (d) Proposed method.

than the AVVs ($\mathbf{V}_{x+1}$ or $\mathbf{V}_{x+2}$) combined with ZVV. Comparing Fig. 6.15 with Fig. 6.16, it can be observed that the overall steady-state performance at low speed (750 r/min) under any control scheme is better than that at high speed (2250 r/min) because of the lower difference between the torque deviations produced by AVV and ZVV.

At 2250 r/min, it can be seen in Fig. 6.16 that the proposed strategy keeps selecting the optimal AVVs as those chosen by M1 (i.e., $\mathbf{V}_{x+1}$ and $\mathbf{V}_{x+2}$). Although it causes a slight increase in the torque ripple by around 5% compared with M1, the flux ripple and current distortions are reduced by 16% and 2.5%, respectively. Moreover, the proposed method achieves less torque ripple than M2 and M3 by about 21% and 28%, respectively.

In terms of flux ripple and current THD, the proposed approach provides reductions by averages of 20% and 5%, respectively, compared with M2 and M3. The reason behind the deterioration of the steady-state performance of M2 and M3 will be further discussed as follows.

For M2, since the flux-control objective is represented by a hard constraint defined by the hysteresis limits of the flux amplitude, according to (6.16) and (6.17), it gives a higher priority for the torque-ripple reduction. Therefore, $\mathbf{V}_{x+1}$ and $\mathbf{V}_{x+2}$ are chosen as the optimal AVVs, as can be seen in Fig. 6.16(b). However, with the discrete values of D_ν (6.15), the hysteresis band of the hard constraint need to be big to avoid the instability that may occur by the failure of both $\mathbf{V}_{x+1}$ and $\mathbf{V}_{x+2}$ to maintain ψ_s within this band. As a result, the flux ripple under M2 increases considerably, as shown in Fig. 6.16(b). On the other hand, M3 employs a ZVV for the whole control cycle instead of $\mathbf{V}_{x+4}$ or $\mathbf{V}_{x+5}$ ($D = 0$) when $T_{err} < 0$ because of the lower negative torque deviation that the ZVV produces. However, the ZVV torque deviation increases significantly at high speed [see Fig. 4.3(g)], leading to high negative pulsations in torque. Thus, either $\mathbf{V}_{x+1}$ or $\mathbf{V}_{x+2}$ is applied in the next control cycle with long working duration (i.e., $D \approx 1$) as the torque deviation produced by them decreases remarkably with the speed increase. Consequently, the duty regulation of M3 is less effective at high speeds than that at low speeds, resulting in a high torque ripple, as shown in Fig. 6.16(c), despite the higher sampling rate.

6.6.3 Comparison of Dynamic Performance

The dynamic torque responses for the four control strategies are also compared, as presented in Fig. 6.17. In this experiment, the machine is driven in torque control mode with a reference signal of 2 N·m, and the load is set

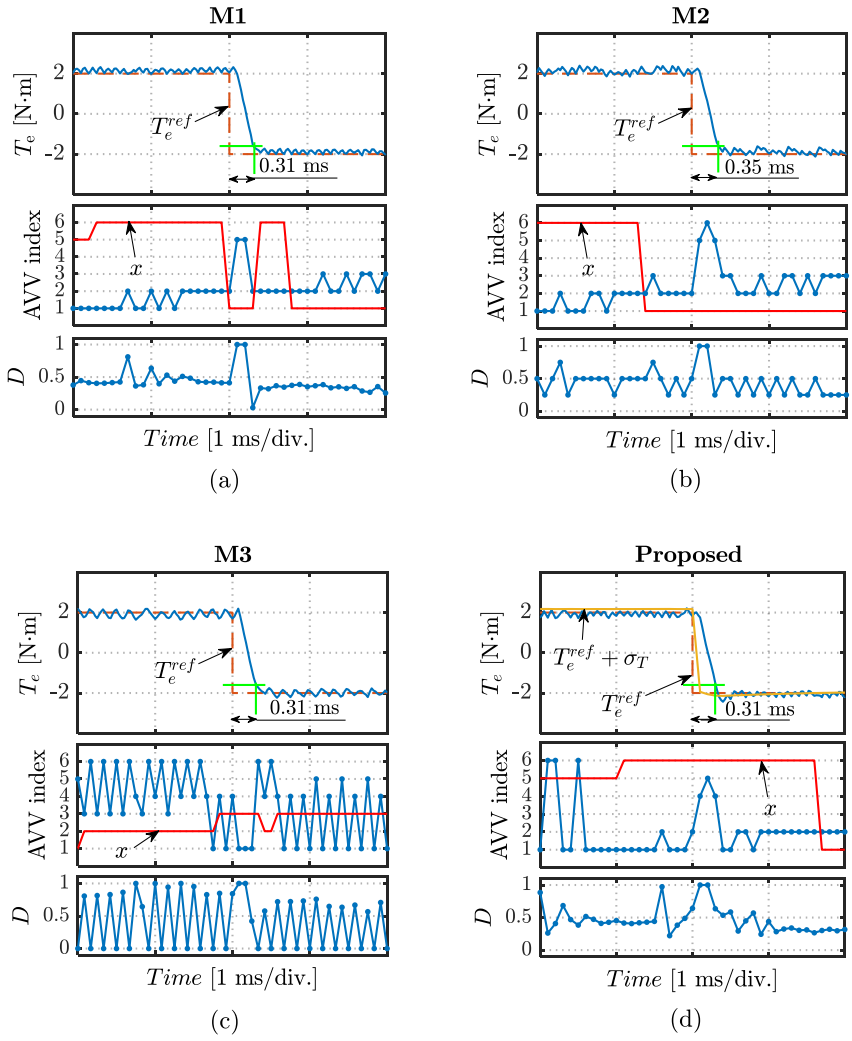

Figure 6.17: Comparison of dynamic performances when the reference torque changes from 2 to -2 N·m. (a) M1, (b) M2, (c) M3, and (d) Proposed method.

to around 1.8 N·m. Once the rotor speed reaches 0.5 p.u., the demanded torque is stepped down to -2 N·m. In Fig. 6.17(d), it can be noticed that the proposed method can select either $\mathbf{V}_{x+4}$ or $\mathbf{V}_{x+5}$ during torque dynamics. Hence, it can maintain the fast dynamic response of the other methods where the falling time is less than 0.4 ms, as shown in Fig. 6.17.

These comparisons confirm the effectiveness of the proposed strategy for the simplification of the control complexity and elimination of the need for a weighting factor while maintaining good steady-state and fast dynamic performances of the conventional M2PTFC method.

6.7 Chapter Summary

In this chapter, a low-complexity M2PTFC method without weighting factor has been proposed for a three-phase PMSM drive. Unlike the conventional method, the proposed scheme assigns separate control objectives for the processes of duty modulation and cost-function evaluation. Based on a detailed analysis of the impact of different voltage vectors on the torque and flux deviations, it utilizes the DRM not only to reduce the torque ripple by applying a combination of ZVV and AVV at every control cycle but also to achieve more goals, as follows:

1. Ensuring the reduction of the computational efforts by minimizing the number of candidate voltage vectors to two AVVs.
2. Maintaining good steady-state performance by avoiding selection of the AVVs that produce high torque deviation during steady-state operation.
3. Guaranteeing fast torque response by allowing these AVVs during dynamic state.
4. Simplifying control implementation by eliminating the need for the weighting factor as the cost-function can be dedicated to achieve the control objective of the stator flux only.

The proposed strategy can be used as a control-based torque-ripple suppression technique for IPMSM if the torque is accurately predicted using FE-based model. The effectiveness of the proposed M2PTFC strategy is verified through comparisons with prior methods in both simulations and experiments.

Chapter 7

Conclusions and Future Works

7.1 Conclusions

Because the 2L-VSI provides a limited number of voltage vectors in three-phase PMSM drives, selecting the optimal option is of significant importance to provide the high-performance torque control required in electrified transportation applications. Therefore, this thesis has closely investigated the voltage vector selection in some advanced DTC strategies applied to PMSM drives and presented solutions to improve the torque performance in terms of the torque ripple and steady-state error while maintaining the fast dynamic response. All the presented control strategies have been validated using a high-accuracy simulation of an 80-kW IPMSM prototype and an experimental setup of a 0.75-kW SPMSM drive.

Therefore, Chapter 2 reviewed the attempts to improve the torque performance for DTC of PMSM in the literature, including ST-DTC with a modified switching table and online tuned hysteresis regulator, SVM-DTC, DDR-DTC, MPTFC, and M2PTFC. As it has been shown, DDR-DTC and

M2PTFC are recommended from the viewpoint of the steady-state and dynamic performances because they can directly manipulate the converter switching transitions and apply voltage vector combination at each control cycle to reduce torque ripple. In Chapter 3, the mathematical model, simulation system, and experimental setup needed to analyze the torque control performance of the PMSM drive throughout the thesis have been introduced. Chapter 4 aims at minimization of torque ripple by first investigating the impact of each voltage vector on the torque and flux responses of ST-DTC, and based on that, an FST without hysteresis regulators has been then presented, which, unlike the conventional tables, considers the operating conditions for the voltage vector selection. This FST achieved about 40% torque ripple reduction in the conventional ST-DTC with reduced flux ripple, current distortions, and average switching frequency. However, both the FST and existing ST-DTC strategies can produce significant steady-state torque error that reaches 27% of the nominal torque.

To eliminate the steady-state torque error while providing further reduced torque ripple, Chapter 5 presented a multiobjective DRR-DTC strategy where the further torque ripple reduction is not only achieved by regulating the duty ratio but also by artificially restricting the AVVs that produce high deviations in torque, and the steady-state torque error is minimized using a virtual reference signal. The effectiveness of the multiobjective DRR-DTC is experimentally verified, showing its superior steady-state performance compared to prior DRR-DTC schemes.

Chapter 6 focused on the complexity reduction of the M2PTFC method that, despite guaranteeing selection of the optimal voltage vector and duty cycle, it needs high computational efforts for predictions and a weighting factor to set the importance of different control objectives. The computation complexity is minimized by preselecting only two-candidate voltage

vectors based on the torque error. The need for a weighting factor is omitted by devoting the torque and flux control objectives to the duty ratio calculation and cost function evaluation, respectively. The simulation and experimental results have verified that the low-complexity M2PTFC method did not cause suboptimality in either the steady-state or the dynamic performances compared with the conventional scheme.

In sum, as has been verified by the simulation and experimental results, this thesis has fulfilled the objectives that have been stated in the introduction by providing overall improvement in the torque performance performance for DTC of PMSM. Hence, the noise and vibration of the electric drive system used in electrified transportation application can be reduced without increasing the control-implementation complexity or degrading the fast dynamic performance of DTC.

7.2 Future Works

The following research works are recommended as future extensions to the DTC strategies presented in this thesis:

- The presented DTC schemes in this work have been only studied when the motor speed and torque are below the nominal values. Since the operation beyond these limits is necessary in transportation applications, especially traction systems, the proposed strategies should also be capable of controlling the machine in flux weakening region and when the load torque exceeds the rated value.
- Because this work focus on the torque-performance improvement of DTC, the voltage replacement strategy is employed in 4.5.2 and 5.3.5 to avoid degradation of the flux control performance during steady-

state operation. Consequently, the angle σ used to define the *Sub-sectors* I and II in (4.19) is arbitrarily set to $\pi/12$ rad, which cannot guarantee the optimal flux control performance. Further investigation can be conducted to determine the optimal value of that angle.

- The position-sensorless estimation of the torque and flux has not considered in this work, and it needs to be investigated for the proposed strategies to enhance the PMSM drive reliability against sensor faults and reduce the initial cost.
- A three-phase PMSM and 2L-VSI are only considered for this study. Thus, investigations to extend the proposed DTC strategies for application with the multi-three phase machines and multilevel converters can allow exploiting their advantages, such as fault tolerance capability and lower current distortions.
- The proposed strategies need to be further investigated to extend the number of employed voltage vector in the sampling period to more than two, therefore achieving a further enhanced steady-state performance.
- More investigations need to be conducted to extend the multiobjective DRR-DTC method (presented in Chapter 5) to be applicable with the IPMSM drives.

Bibliography

[1] Statista, "Transportation emissions worldwide," Available at https://www.statista.com/study/85839/global-transportation-emissions/ (2022/05/10).

[2] IEA, "Trends and developments in electric vehicle markets," Available at https://www.iea.org/reports/global-ev-outlook-2021/trends-and-developments-in-electric-vehicle-markets (2022/05/10).

[3] T. A. Johansen and T. I. Fossen, "Control allocation-a survey," *Automatica*, vol. 49, no. 5, pp. 1087–1103, 2013.

[4] M. Tang, "Torque ripple reduction in AC permanent magnet servo motor drives," Doctoral thesis, 2017.

[5] EETimes, "Electrification factor in transportation," Available at https://www.eetimes.com/electrification-factor-in-transportation/ (2022/05/12).

[6] I. Husain, B. Ozpineci, M. S. Islam, E. Gurpinar, G.-J. Su, W. Yu, S. Chowdhury, L. Xue, D. Rahman, and R. Sahu, "Electric drive technology trends, challenges, and opportunities for future electric vehicles," *Proceedings of the IEEE*, vol. 109, no. 6, pp. 1039–1059, 2021.

[7] L. Zhao, M.-I. Roh, and Zhou, "A thrust allocation method for ef-

ficient dynamic positioning of a semisubmersible drilling rig based on the hybrid optimization algorithm," *Mathematical Problems in Engineering*, vol. 2015, p. 12, 2015.

[8] D. K. Hyun, T. P. Aaron, and J. A. Phillip, "A review of distributed electric propulsion concepts for air vehicle technology," in *2018 AIAA/IEEE Electric Aircraft Technologies Symposium*, 2018, pp. 1–21.

[9] T. Goggia, A. Sorniotti, L. De Novellis, A. Ferrara, P. Gruber, J. Theunissen, D. Steenbeke, B. Knauder, and J. Zehetner, "Integral sliding mode for the torque-vectoring control of fully electric vehicles: Theoretical design and experimental assessment," *IEEE Transactions on Vehicular Technology*, vol. 64, no. 5, pp. 1701–1715, 2015.

[10] G. Qiao, G. Liu, Z. Shi, Y. Wang, S. Ma, and T. C. Lim, "A review of electromechanical actuators for more/all electric aircraft systems," *Proceedings of the Institution of Mechanical Engineers, Part C: Journal of Mechanical Engineering Science*, vol. 232, no. 22, pp. 4128–4151, 2018.

[11] B. Bilgin and A. Emadi, "Electric motors in electrified transportation: A step toward achieving a sustainable and highly efficient transportation system," *IEEE Power Electronics Magazine*, vol. 1, no. 2, pp. 10–17, 2014.

[12] W. Cai, X. Wu, M. Zhou, Y. Liang, and Y. Wang, "Review and development of electric motor systems and electric powertrains for new energy vehicles," *Automotive Innovation*, vol. 4, pp. 3–22, 2021.

[13] M.-S. Huang, K.-C. Chen, T.-K. Chen, Y.-C. Liang, and G.-Y. Pan, "An innovative constant voltage control method of PMSM-type ISG

under wide engine speed range for scooter with idling stop," *IEEE Access*, vol. 7, pp. 20 723–20 733, 2019.

[14] E. Sayed, M. Abdalmagid, G. Pietrini, N.-M. Sa'adeh, A. D. Callegaro, C. Goldstein, and A. Emadi, "Review of electric machines in more-/hybrid-/turbo-electric aircraft," *IEEE Transactions on Transportation Electrification*, vol. 7, no. 4, pp. 2976–3005, 2021.

[15] B. K. Bose, *Power electronics and motor drives: advances and trends*. Academic press, 2020.

[16] X. Chen, J. Wang, and A. Griffo, "A high-fidelity and computationally efficient electrothermally coupled model for interior permanent-magnet machines in electric vehicle traction applications," *IEEE Transactions on Transportation Electrification*, vol. 1, no. 4, pp. 336–347, 2015.

[17] K. Lewotsky, "Interior permanent magnet motors power traction motor applications," https://www.automate.org/industry-insights/interior-permanent-magnet-motors-power-traction-motor-applications (2022/05/14).

[18] X. Chen, J. Wang, B. Sen, P. Lazari, and T. Sun, "A high-fidelity and computationally efficient model for interior permanent-magnet machines considering the magnetic saturation, spatial harmonics, and iron loss effect," *IEEE Transactions on Industrial Electronics*, vol. 62, no. 7, pp. 4044–4055, 2015.

[19] S. Paitandi and M. Sengupta, "Analysis, fabrication and detailed comparative study of surface and interior rotor PMSM prototypes of identical nominal ratings and stators," *Sādhanā*, vol. 45, no. 1, pp. 1–24, 2020.

[20] S.-G. Lee, S. Kim, J.-C. Park, M.-R. Park, T. H. Lee, and M.-S. Lim, "Robust design optimization of SPMSM for robotic actuator considering assembly imperfection of segmented stator core," *IEEE Transactions on Energy Conversion*, vol. 35, no. 4, pp. 2076–2085, 2020.

[21] T. Sutikno, N. Rumzi Nik Idris, and A. Jidin, "A review of direct torque control of induction motors for sustainable reliability and energy efficient drives," *Renewable and Sustainable Energy Reviews*, vol. 32, pp. 548–558, 2014.

[22] Palma, J. Moreno, J. Palma, R. Domínguez, J. Rohten, and V. Esparza, "Comprehensive review of torque and vectoring control for electrical powertrains," in *2021 IEEE International Conference on Automation/XXIV Congress of the Chilean Association of Automatic Control (ICA-ACCA)*, 2021, pp. 1–7.

[23] W. Deng and S. Zuo, "Electromagnetic vibration and noise of the permanent-magnet synchronous motors for electric vehicles: An overview," *IEEE Transactions on Transportation Electrification*, vol. 5, no. 1, pp. 59–70, 2019.

[24] X. Wang, Z. Wang, Z. Xu, M. Cheng, and Y. Hu, "Optimization of torque tracking performance for direct-torque-controlled PMSM drives with composite torque regulator," *IEEE Transactions on Industrial Electronics*, vol. 67, no. 12, pp. 10 095–10 108, 2020.

[25] G. Wang, M. Valla, and J. Solsona, "Position sensorless permanent magnet synchronous machine drives—a review," *IEEE Transactions on Industrial Electronics*, vol. 67, no. 7, pp. 5830–5842, 2020.

[26] T. Geyer, "Introduction," in *Model predictive control of high power*

converters and industrial drives. John Wiley Sons, Ltd, 2017, ch. 1, pp. 1–28.

[27] F. Blaschke, "The principle of field orientation applied to the new transvector closed-loop control system of rotating field machines," *Siemens Rev.*, vol. 39, pp. 217–220, 1972.

[28] I. Takahashi and T. Noguchi, "A new quick-response and high-efficiency control strategy of an induction motor," *IEEE Transactions on Industry Applications*, vol. IA-22, no. 5, pp. 820–827, 1986.

[29] S.-H. Kim, *Electric Motor Control: DC, AC, and BLDC Motors*. Amsterdam, Netherlands: Elsevier Science, 2017.

[30] F. Niu, B. Wang, A. S. Babel, K. Li, and E. G. Strangas, "Comparative evaluation of direct torque control strategies for permanent magnet synchronous machines," *IEEE Transactions on Power Electronics*, vol. 31, no. 2, pp. 1408–1424, 2016.

[31] Z. Q. Zhu, Y. Ren, and J. Liu, "Improved torque regulator to reduce steady-state error of torque response for direct torque control of permanent magnet synchronous machine drives," *IET Electric Power Applications*, vol. 8, no. 3, pp. 108–116, 2014.

[32] F. Niu, K. Li, and Y. Wang, "Direct torque control for permanent-magnet synchronous machines based on duty ratio modulation," *IEEE Transactions on Industrial Electronics*, vol. 62, no. 10, pp. 6160–6170, 2015.

[33] F. Niu, X. Huang, L. Ge, J. Zhang, L. Wu, Y. Wang, K. Li, and Y. Fang, "A simple and practical duty cycle modulated direct torque control for permanent magnet synchronous motors," *IEEE Transactions on Power Electronics*, vol. 34, no. 2, pp. 1572–1579, 2019.

[34] Y. Ren, Z. Q. Zhu, and J. Liu, "Direct torque control of permanent-magnet synchronous machine drives with a simple duty ratio regulator," *IEEE Transactions on Industrial Electronics*, vol. 61, no. 10, pp. 5249–5258, 2014.

[35] Y. Zhang and J. Zhu, "Direct torque control of permanent magnet synchronous motor with reduced torque ripple and commutation frequency," *IEEE Transactions on Power Electronics*, vol. 26, no. 1, pp. 235–248, 2011.

[36] ——, "A novel duty cycle control strategy to reduce both torque and flux ripples for DTC of permanent magnet synchronous motor drives with switching frequency reduction," *IEEE Transactions on Power Electronics*, vol. 26, no. 10, pp. 3055–3067, 2011.

[37] Z. Zhang and X. Liu, "A duty ratio control strategy to reduce both torque and flux ripples of DTC for permanent magnet synchronous machines," *IEEE Access*, vol. 7, pp. 11 820–11 828, 2019.

[38] D. Świerczyński, "Direct Torque Control with Space Vector Modulation (DTC-SVM) of Inverter-fed Permanent Magnet Synchronous Motor Drive," Doctoral thesis, 2005.

[39] D. Świerczyński and M. Kazmierkowski, "Direct torque control of permanent magnet synchronous motor (PMSM) using space vector modulation (DTC-SVM)-simulation and experimental results," in *IEEE 2002 28th Annual Conference of the Industrial Electronics Society. IECON 02*, vol. 1, 2002, pp. 751–755 vol.1.

[40] M. Norambuena, J. Rodriguez, Z. Zhang, F. Wang, C. Garcia, and R. Kennel, "A very simple strategy for high-quality performance of AC machines using model predictive control," *IEEE Transactions on Power Electronics*, vol. 34, no. 1, pp. 794–800, 2019.

[41] Y. Zhang, B. Zhang, H. Yang, M. Norambuena, and J. Rodriguez, "Generalized sequential model predictive control of im drives with field-weakening ability," *IEEE Transactions on Power Electronics*, vol. 34, no. 9, pp. 8944–8955, 2019.

[42] F. Wang, H. Xie, Q. Chen, S. A. Davari, J. Rodriguez, and R. Kennel, "Parallel predictive torque control for induction machines without weighting factors," *IEEE Transactions on Power Electronics*, vol. 35, no. 2, pp. 1779–1788, 2020.

[43] S. A. Davari, M. Norambuena, V. Nekoukar, C. Garcia, and J. Rodriguez, "Even-handed sequential predictive torque and flux control," *IEEE Transactions on Industrial Electronics*, vol. 67, no. 9, pp. 7334–7342, 2020.

[44] E. Kusuma, K. M. R. Eswar, and T. Vinay Kumar, "An effective predictive torque control scheme for PMSM drive without involvement of weighting factors," *IEEE Journal of Emerging and Selected Topics in Power Electronics*, vol. 9, no. 3, pp. 2685–2697, 2021.

[45] M. Habibullah, D. D.-C. Lu, D. Xiao, and M. F. Rahman, "A simplified finite-state predictive direct torque control for induction motor drive," *IEEE Transactions on Industrial Electronics*, vol. 63, no. 6, pp. 3964–3975, 2016.

[46] M. Mamdouh and M. A. Abido, "Efficient predictive torque control for induction motor drive," *IEEE Transactions on Industrial Electronics*, vol. 66, no. 9, pp. 6757–6767, 2019.

[47] Y. Zhang and H. Yang, "Model predictive torque control of induction motor drives with optimal duty cycle control," *IEEE Transactions on Power Electronics*, vol. 29, no. 12, pp. 6593–6603, 2014.

[48] L. He, F. Wang, and D. Ke, "FPGA-based sliding-mode predictive control for PMSM speed regulation system using an adaptive ultralocal model," *IEEE Transactions on Power Electronics*, vol. 36, no. 5, pp. 5784–5793, 2021.

[49] C. Buccella, C. Cecati, and H. Latafat, "Digital control of power converters—a survey," *IEEE Transactions on Industrial Informatics*, vol. 8, no. 3, pp. 437–447, 2012.

[50] L. Zhong, M. Rahman, W. Hu, and K. Lim, "Analysis of direct torque control in permanent magnet synchronous motor drives," *IEEE Transactions on Power Electronics*, vol. 12, no. 3, pp. 528–536, 1997.

[51] M. Rahman, L. Zhong, M. Haque, and M. Rahman, "A direct torque-controlled interior permanent-magnet synchronous motor drive without a speed sensor," *IEEE Transactions on Energy Conversion*, vol. 18, no. 1, pp. 17–22, 2003.

[52] H. Yuwen, T. Cun, G. Yikang, Y. Zhiqing, L. Tang, and M. Rahman, "In-depth research on direct torque control of permanent magnet synchronous motor," in *IEEE 2002 28th Annual Conference of the Industrial Electronics Society. IECON 02*, vol. 2, 2002, pp. 1060–1065.

[53] L. Zhong, M. Rahman, W. Hu, K. Lim, and M. Rahman, "A direct torque controller for permanent magnet synchronous motor drives," *IEEE Transactions on Energy Conversion*, vol. 14, no. 3, pp. 637–642, 1999.

[54] S. Wang, C. Li, C. Che, and D. Xu, "Direct torque control for 2L-VSI PMSM using switching instant table," *IEEE Transactions on Industrial Electronics*, vol. 65, no. 12, pp. 9410–9420, 2018.

[55] P. Vas, "Vector and direct torque control of synchronous machines," in *Sensorless Vector and Direct Torque Control*. Oxford, United Kingdom: Oxford University Press, 1998, ch. 3, pp. 87–257.

[56] N. El Ouanjli, A. Derouich, A. El Ghzizal, S. Motahhir, A. Chebabhi, Y. El Mourabit, and M. Taoussi, "Modern improvement techniques of direct torque control for induction motor drives - a reviews," *Protection and Control of Modern Power Systems*, vol. 4, no. 11, pp. 1–12, 2019.

[57] M. Rahman, M. Haque, L. Tang, and L. Zhong, "Problems associated with the direct torque control of an interior permanent-magnet synchronous motor drive and their remedies," *IEEE Transactions on Industrial Electronics*, vol. 51, no. 4, pp. 799–809, 2004.

[58] Y. Sangsefidi, S. Ziaeinejad, A. Mehrizi-Sani, H. Pairodin-Nabi, and A. Shoulaie, "Estimation of stator resistance in direct torque control synchronous motor drives," *IEEE Transactions on Energy Conversion*, vol. 30, no. 2, pp. 626–634, 2015.

[59] M. Haque and M. Rahman, "Influence of stator resistance variation on direct torque controlled interior permanent magnet synchronous motor drive performance and its compensation," in *Conference Record of the 2001 IEEE Industry Applications Conference. 36th IAS Annual Meeting (Cat. No.01CH37248)*, vol. 4, 2001, pp. 2563–2569 vol.4.

[60] S. Mir, M. Elbuluk, and D. Zinger, "PI and fuzzy estimators for tuning the stator resistance in direct torque control of induction machines," *IEEE Transactions on Power Electronics*, vol. 13, no. 2, pp. 279–287, 1998.

[61] F. Zidani, D. Diallo, M. Benbouzid, and R. Nait-Said, "Direct torque control of induction motor with fuzzy stator resistance adaptation," *IEEE Transactions on Energy Conversion*, vol. 21, no. 2, pp. 619–621, 2006.

[62] G. H. B. Foo and M. F. Rahman, "Direct torque control of an IPM-synchronous motor drive at very low speed using a sliding-mode stator flux observer," *IEEE Transactions on Power Electronics*, vol. 25, no. 4, pp. 933–942, 2010.

[63] Y. Xu, N. Parspour, and U. Vollmer, "Torque ripple minimization using online estimation of the stator resistances with consideration of magnetic saturation," *IEEE Transactions on Industrial Electronics*, vol. 61, no. 9, pp. 5105–5114, 2014.

[64] Z. Q. Zhu, D. Liang, and K. Liu, "Online parameter estimation for permanent magnet synchronous machines: An overview," *IEEE Access*, vol. 9, pp. 59 059–59 084, 2021.

[65] J. Hu and B. Wu, "New integration algorithms for estimating motor flux over a wide speed range," *IEEE Transactions on Power Electronics*, vol. 13, no. 5, pp. 969–977, 1998.

[66] A. Choudhury, P. Pillay, and S. S. Williamson, "Modified stator flux estimation based direct torque controlled PMSM drive for hybrid electric vehicle," in *IECON 2012 - 38th Annual Conference on IEEE Industrial Electronics Society*, 2012, pp. 2965–2970.

[67] M. Hinkkanen, "Flux estimators for speed-sensorless induction motor drives," Doctoral thesis, 2004.

[68] T. J. Vyncke, R. K. Boel, and J. A. A. Melkebeek, "A comparison of stator flux linkage estimators for a direct torque controlled PMSM

drive," in *2009 35th Annual Conference of IEEE Industrial Electronics*, 2009, pp. 971–978.

[69] A. Shinohara, Y. Inoue, S. Morimoto, and M. Sanada, "Comparison of stator flux linkage estimators for PWM-based direct torque controlled PMSM drives," in *2015 IEEE 11th International Conference on Power Electronics and Drive Systems*, 2015, pp. 1035–1040.

[70] M. Koteich, "Flux estimation algorithms for electric drives: A comparative study," in *2016 3rd International Conference on Renewable Energies for Developing Countries (REDEC)*, 2016, pp. 1–6.

[71] I. Boldea, M. C. Paicu, and G.-D. Andreescu, "Active flux concept for motion-sensorless unified AC drives," *IEEE Transactions on Power Electronics*, vol. 23, no. 5, pp. 2612–2618, 2008.

[72] H. Saberi, M. Sabahi, M. B. B. Sharifian, and M. Feyzi, "Improved sensorless direct torque control method using adaptive flux observer," *IET Power Electronics*, vol. 7, no. 7, pp. 1675–1684, 2014.

[73] D. Nguyen, R. Dutta, M. F. Rahman, and J. E. Fletcher, "Performance of a sensorless controlled concentrated-wound interior permanent-magnet synchronous machine at low and zero speed," *IEEE Transactions on Industrial Electronics*, vol. 63, no. 4, pp. 2016–2026, 2016.

[74] X. Lin, W. Huang, W. Jiang, Y. Zhao, and S. Zhu, "Deadbeat direct torque and flux control for permanent magnet synchronous motor based on stator flux oriented," *IEEE Transactions on Power Electronics*, vol. 35, no. 5, pp. 5078–5092, 2020.

[75] S. Nakashima, Y. Inagaki, and I. Miki, "Sensorless initial rotor position estimation of surface permanent-magnet synchronous motor,"

IEEE Transactions on Industry Applications, vol. 36, no. 6, pp. 1598–1603, 2000.

[76] M. Haque, L. Zhong, and M. Rahman, "A sensorless initial rotor position estimation scheme for a direct torque controlled interior permanent magnet synchronous motor drive," *IEEE Transactions on Power Electronics*, vol. 18, no. 6, pp. 1376–1383, 2003.

[77] T. Michalski, C. Lopez, A. Garcia, and L. Romeral, "Sensorless control of five phase PMSM based on extended kalman filter," in *IECON 2016 - 42nd Annual Conference of the IEEE Industrial Electronics Society*, 2016, pp. 2904–2909.

[78] Y. Yao, Y. Huang, F. Peng, J. Dong, and Z. Zhu, "Compensation method of position estimation error for high-speed surface-mounted pmsm drives based on robust inductance estimation," *IEEE Transactions on Power Electronics*, vol. 37, no. 2, pp. 2033–2044, 2022.

[79] A. Shinohara, Y. Inoue, S. Morimoto, and M. Sanada, "Direct calculation method of reference flux linkage for maximum torque per ampere control in DTC-based IPMSM drives," *IEEE Transactions on Power Electronics*, vol. 32, no. 3, pp. 2114–2122, 2017.

[80] M. N. Uddin, H. Zou, and F. Azevedo, "Online loss-minimization-based adaptive flux observer for direct torque and flux control of pmsm drive," *IEEE Transactions on Industry Applications*, vol. 52, no. 1, pp. 425–431, 2016.

[81] S. Ekanayake, R. Dutta, M. F. Rahman, and D. Xiao, "Direct torque and flux control of interior permanent magnet synchronous machine in deep flux-weakening region," *IET Electric Power Applications*, vol. 12, no. 1, pp. 98–105, 2018.

[82] A. Shinohara, Y. Inoue, S. Morimoto, and M. Sanada, "Maximum torque per ampere control in stator flux linkage synchronous frame for DTC-based PMSM drives without using q-axis inductance," *IEEE Transactions on Industry Applications*, vol. 53, no. 4, pp. 3663–3671, 2017.

[83] M. H. Mahmud, Y. Wu, and Y. Zhao, "Extremum seeking-based optimum reference flux searching for direct torque control of interior permanent magnet synchronous motors," *IEEE Transactions on Transportation Electrification*, vol. 6, no. 1, pp. 41–51, 2020.

[84] S. B. H. Toufouti, R.and Meziane, "Direct torque control strategy of induction motors," *Acta Electrotechnica et Informatica*, vol. 7, no. 1, pp. 22–28, 2007.

[85] Y. Li, D. Gerling, and W. Liu, "A novel switching table using zero voltage vectors for direct torque control in permanent magnet synchronous motor," in *2008 18th International Conference on Electrical Machines*, 2008, pp. 1–6.

[86] C. Xia, S. Wang, Z. Wang, and T. Shi, "Direct torque control for VSI-PMSMs using four-dimensional switching-table," *IEEE Transactions on Power Electronics*, vol. 31, no. 8, pp. 5774–5785, 2016.

[87] O. Sandre-Hernandez, J. Rangel-Magdaleno, and R. Morales-Caporal, "A comparison on finite-set model predictive torque control schemes for PMSMs," *IEEE Transactions on Power Electronics*, vol. 33, no. 10, pp. 8838–8847, 2018.

[88] F. Ban, G. Lian, J. Zhang, B. Chen, and G. Gu, "Study on a novel predictive torque control strategy based on the finite control set for PMSM," *IEEE Transactions on Applied Superconductivity*, vol. 29, no. 2, pp. 1–6, 2019.

[89] J. A. Rohten, J. E. Muñoz, E. S. Pulido, J. J. Silva, F. A. Villarroel, and J. R. Espinoza, "Very low sampling frequency model predictive control for power converters in the medium and high-power range applications," *Energies*, vol. 14, no. 1, p. 199, Jan 2021.

[90] S. Mathapati and J. Bocker, "Analytical and offline approach to select optimal hysteresis bands of DTC for PMSM," *IEEE Transactions on Industrial Electronics*, vol. 60, no. 3, pp. 885–895, 2013.

[91] X. Zhang and G. H. B. Foo, "A constant switching frequency-based direct torque control method for interior permanent-magnet synchronous motor drives," *IEEE/ASME Transactions on Mechatronics*, vol. 21, no. 3, pp. 1445–1456, 2016.

[92] H. Miranda, P. Cortes, J. I. Yuz, and J. Rodriguez, "Predictive torque control of induction machines based on state-space models," *IEEE Transactions on Industrial Electronics*, vol. 56, no. 6, pp. 1916–1924, 2009.

[93] Y. Zhang, J. Zhu, and W. Xu, "Analysis of one step delay in direct torque control of permanent magnet synchronous motor and its remedies," in *2010 International Conference on Electrical Machines and Systems*, 2010, pp. 792–797.

[94] A. Rahideh, A. Rahideh, M. Karimi, A. Shakeri, and M. Azadi, "High performance direct torque control of a PMSM using fuzzy logic and genetic algorithm," in *2007 IEEE International Electric Machines Drives Conference*, vol. 2, 2007, pp. 932–937.

[95] M. N. Uddin and M. Hafeez, "FLC based DTC scheme to improve the dynamic performance of an IM drive," in *2010 IEEE Industry Applications Society Annual Meeting*, 2010, pp. 1–7.

[96] B. Badre, K. Mohammed, I. Silviu, and L. Ahmed, "DTC control based artificial neural network for high performance PMSM drive," *Journal of Theoretical and Applied Information Technology*, vol. 33, no. 2, pp. 165–176, 2011.

[97] R. Kumar, R. Gupta, S. Bhangale, and H. Gothwal, "Artificial neural network based direct torque control of induction motor drives," in *2007 IET-UK International Conference on Information and Communication Technology in Electrical Sciences (ICTES 2007)*, 2007, pp. 361–367.

[98] M. H. Vafaie, B. M. Dehkordi, P. Moallem, and A. Kiyoumarsi, "Improving the steady-state and transient-state performances of PMSM through an advanced deadbeat direct torque and flux control system," *IEEE Transactions on Power Electronics*, vol. 32, no. 4, pp. 2964–2975, 2017.

[99] J. S. Lee, C.-H. Choi, J.-K. Seok, and R. D. Lorenz, "Deadbeat-direct torque and flux control of interior permanent magnet synchronous machines with discrete time stator current and stator flux linkage observer," *IEEE Transactions on Industry Applications*, vol. 47, no. 4, pp. 1749–1758, 2011.

[100] W. Wang, C. Liu, H. Zhao, and Z. Song, "Improved deadbeat-direct torque and flux control for PMSM with less computation and enhanced robustness," *IEEE Transactions on Industrial Electronics*, pp. 1–1, 2022.

[101] Y. Wang, N. Niimura, and R. D. Lorenz, "Real-time parameter identification and integration on deadbeat-direct torque and flux control (DB-DTFC) without inducing additional torque ripple," *IEEE*

Transactions on Industry Applications, vol. 52, no. 4, pp. 3104–3114, 2016.

[102] J. Huang, Q. Xu, X. Shi, L. Cui, and Z. Xiang, "Direct torque control of PMSM based on fractional order sliding mode variable structure and space vector pulse width modulation," in *Proceedings of the 33rd Chinese Control Conference*, 2014, pp. 8097–8101.

[103] A. Naassani, E. Monmasson, and J.-P. Louis, "Synthesis of direct torque and rotor flux control algorithms by means of sliding-mode theory," *IEEE Transactions on Industrial Electronics*, vol. 52, no. 3, pp. 785–799, 2005.

[104] C. Lascu, A. Argeseanu, and F. Blaabjerg, "Supertwisting sliding-mode direct torque and flux control of induction machine drives," *IEEE Transactions on Power Electronics*, vol. 35, no. 5, pp. 5057–5065, 2020.

[105] L. Lianbing, W. Xiaojun, and S. Hexu, "A variable-voltage direct torque control based on DSP in PM synchronous motor drive," in *2002 IEEE Region 10 Conference on Computers, Communications, Control and Power Engineering. TENCOM '02. Proceedings.*, vol. 3, 2002, pp. 2065–2068 vol.3.

[106] D. Casadei, G. Serra, and K. Tani, "Implementation of a direct control algorithm for induction motors based on discrete space vector modulation," *IEEE Transactions on Power Electronics*, vol. 15, no. 4, pp. 769–777, 2000.

[107] J.-K. Kang and S.-K. Sul, "New direct torque control of induction motor for minimum torque ripple and constant switching frequency," *IEEE Transactions on Industry Applications*, vol. 35, no. 5, pp. 1076–1082, 1999.

[108] J. Rodriguez, C. Garcia, A. Mora, S. A. Davari, J. Rodas, D. F. Valencia, M. Elmorshedy, F. Wang, K. Zuo, L. Tarisciotti, F. Flores-Bahamonde, W. Xu, Z. Zhang, Y. Zhang, M. Norambuena, A. Emadi, T. Geyer, R. Kennel, T. Dragicevic, D. A. Khaburi, Z. Zhang, M. Abdelrahem, and N. Mijatovic, "Latest advances of model predictive control in electrical drives—part II: Applications and benchmarking with classical control methods," *IEEE Transactions on Power Electronics*, vol. 37, no. 5, pp. 5047–5061, 2022.

[109] G. Cimini, D. Bernardini, S. Levijoki, and A. Bemporad, "Embedded model predictive control with certified real-time optimization for synchronous motors," *IEEE Transactions on Control Systems Technology*, vol. 29, no. 2, pp. 893–900, 2021.

[110] P. Karamanakos and T. Geyer, "Guidelines for the design of finite control set model predictive controllers," *IEEE Transactions on Power Electronics*, vol. 35, no. 7, pp. 7434–7450, 2020.

[111] A. A. Ahmed, B. K. Koh, and Y. I. Lee, "A comparison of finite control set and continuous control set model predictive control schemes for speed control of induction motors," *IEEE Transactions on Industrial Informatics*, vol. 14, no. 4, pp. 1334–1346, 2018.

[112] T. Geyer, G. Papafotiou, and M. Morari, "Model predictive direct torque control—part I: concept, algorithm, and analysis," *IEEE Transactions on Industrial Electronics*, vol. 56, no. 6, pp. 1894–1905, 2009.

[113] C. A. Rojas, J. R. Rodriguez, S. Kouro, and F. Villarroel, "Multiobjective fuzzy-decision-making predictive torque control for an induction motor drive," *IEEE Transactions on Power Electronics*, vol. 32, no. 8, pp. 6245–6260, 2017.

[114] M. Novak, H. Xie, T. Dragicevic, F. Wang, J. Rodriguez, and F. Blaabjerg, "Optimal cost function parameter design in predictive torque control (PTC) using artificial neural networks (ANN)," *IEEE Transactions on Industrial Electronics*, vol. 68, no. 8, pp. 7309–7319, 2021.

[115] Q. Wang, H. Yu, C. Li, X. Lang, S. S. Yeoh, T. Yang, M. Rivera, S. Bozhko, and P. Wheeler, "A low-complexity optimal switching time-modulated model-predictive control for PMSM with three-level NPC converter," *IEEE Transactions on Transportation Electrification*, vol. 6, no. 3, pp. 1188–1198, 2020.

[116] Y. Zhang and X. Wei, "Torque ripple RMS minimization in model predictive torque control of PMSM drives," in *2013 International Conference on Electrical Machines and Systems (ICEMS)*, 2013, pp. 2183–2188.

[117] S.-S. Lv and H. Lin, "Model predictive direct torque control for PMSM with duty cycle optimization," in *2015 Fifth International Conference on Instrumentation and Measurement, Computer, Communication and Control (IMCCC)*, 2015, pp. 866–871.

[118] Z. Song, X. Ma, and R. Zhang, "Enhanced finite-control-set model predictive flux control of permanent magnet synchronous machines with minimum torque ripples," *IEEE Transactions on Industrial Electronics*, vol. 68, no. 9, pp. 7804–7813, 2021.

[119] W. Chen, S. Zeng, G. Zhang, T. Shi, and C. Xia, "A modified double vectors model predictive torque control of permanent magnet synchronous motor," *IEEE Transactions on Power Electronics*, vol. 34, no. 11, pp. 11 419–11 428, 2019.

[120] Z. Zhou, C. Xia, Y. Yan, Z. Wang, and T. Shi, "Torque ripple minimization of predictive torque control for pmsm with extended control set," *IEEE Transactions on Industrial Electronics*, vol. 64, no. 9, pp. 6930–6939, 2017.

[121] T. Wang, C. Liu, G. Lei, Y. Guo, and J. Zhu, "Model predictive direct torque control of permanent magnet synchronous motors with extended set of voltage space vectors," *IET Electric Power Applications*, vol. 11, no. 8, pp. 1376–1382, 2017.

[122] T. Geyer, "Computationally efficient model predictive direct torque control," *IEEE Transactions on Power Electronics*, vol. 26, no. 10, pp. 2804–2816, 2011.

[123] M. R. Nikzad, B. Asaei, and S. O. Ahmadi, "Discrete duty-cycle-control method for direct torque control of induction motor drives with model predictive solution," *IEEE Transactions on Power Electronics*, vol. 33, no. 3, pp. 2317–2329, 2018.

[124] M. Wu, X. Sun, J. Zhu, G. Lei, and Y. Guo, "Improved model predictive torque control for PMSM drives based on duty cycle optimization," *IEEE Transactions on Magnetics*, vol. 57, no. 2, pp. 1–5, 2021.

[125] W. Q. Chu and Z. Q. Zhu, "Investigation of torque ripples in permanent magnet synchronous machines with skewing," *IEEE Transactions on Magnetics*, vol. 49, no. 3, pp. 1211–1220, 2013.

[126] T. Sebastian, G. Slemon, and M. Rahman, "Modelling of permanent magnet synchronous motors," *IEEE Transactions on Magnetics*, vol. 22, no. 5, pp. 1069–1071, 1986.

[127] N. Nakao and K. Akatsu, "Suppressing pulsating torques: torque

ripple control for synchronous motors," *IEEE Industry Applications Magazine*, vol. 20, no. 6, pp. 33–44, 2014.

[128] C. Lai, G. Feng, K. Mukherjee, V. Loukanov, and N. C. Kar, "Torque ripple modeling and minimization for interior PMSM considering magnetic saturation," *IEEE Transactions on Power Electronics*, vol. 33, no. 3, pp. 2417–2429, 2018.

[129] H. Kaimori, N. Nakao, T. Sakaue, and K. Akatsu, "Behavior modeling of permanent magnet synchronous motors using flux linkages for coupling with circuit simulation," in *2014 International Conference on Electrical Machines (ICEM)*, 2014, pp. 2695–2701.

[130] N. Bracikowski, M. Hecquet, P. Brochet, and S. V. Shirinskii, "Multiphysics modeling of a permanent magnet synchronous machine by using lumped models," *IEEE Transactions on Industrial Electronics*, vol. 59, no. 6, pp. 2426–2437, 2012.

[131] J. S. Lee and G. Choi, "Modeling and hardware-in-the-loop system realization of electric machine drives — a review," *CES Transactions on Electrical Machines and Systems*, vol. 5, no. 3, pp. 194–201, 2021.

[132] J. D'Errico, "Surface fitting using gridfit," Matlab Central Files Exchange, https://https://www.mathworks.com/matlabcentral/fileexchange/8998-surface-fitting-using-gridfit (2022/11/14).

[133] Y. Wang, W. Xie, X. Wang, W. Yang, M. Dou, S. Song, and D. Gerling, "Fast response model predictive torque and flux control with low calculation effort for PMSMs," *IEEE Transactions on Industrial Informatics*, vol. 15, no. 10, pp. 5531–5540, 2019.

[134] Y. Ren and Z. Q. Zhu, "Enhancement of steady-state performance in direct-torque-controlled dual three-phase permanent-magnet syn-

chronous machine drives with modified switching table," *IEEE Transactions on Industrial Electronics*, vol. 62, no. 6, pp. 3338–3350, 2015.

[135] J. E. Everett, "The exponentially weighted moving average applied to the control and monitoring of varying sample sizes," *WIT transactions on modelling and simulation*, vol. 51, pp. 3–13, 2011.

[136] S. J. Orfanidis, "Exponential smoothing," in *Applied Optimum Signal Processing*. New York, NY, USA: McGraw-Hill, 2018, ch. 6, pp. 221–314.

[137] M. Pacas and J. Weber, "Predictive direct torque control for the PM synchronous machine," *IEEE Transactions on Industrial Electronics*, vol. 52, no. 5, pp. 1350–1356, 2005.

[138] P. Cortes, J. Rodriguez, C. Silva, and A. Flores, "Delay compensation in model predictive current control of a three-phase inverter," *IEEE Transactions on Industrial Electronics*, vol. 59, no. 2, pp. 1323–1325, 2012.

[139] M. Preindl and S. Bolognani, "Model predictive direct torque control with finite control set for PMSM drive systems, part 1: maximum torque per ampere operation," *IEEE Transactions on Industrial Informatics*, vol. 9, no. 4, pp. 1912–1921, 2013.

[140] Y. Zhang, H. Yang, and B. Xia, "Model-predictive control of induction motor drives: Torque control versus flux control," *IEEE Transactions on Industry Applications*, vol. 52, no. 5, pp. 4050–4060, 2016.

[141] X. Zhang and B. Hou, "Double vectors model predictive torque control without weighting factor based on voltage tracking error," *IEEE Transactions on Power Electronics*, vol. 33, no. 3, pp. 2368–2380, 2018.

[142] X. Li, Z. Xue, L. Zhang, and W. Hua, "A low-complexity three-vector-based model predictive torque control for SPMSM," *IEEE Transactions on Power Electronics*, vol. 36, no. 11, pp. 13 002–13 012, 2021.

Appendices

Appendix A

Reference Frames Definition

The modeling, simulation, and implementation of the control scheme of the electric drive can be simplified by using the proper reference frame transformation. In this work, two reference frames are used: the stationary frame (abc or $\alpha\beta$) and the synchronous rotating frame (dq).

As shown in Fig. A.1, the abc axes are 120° shifted from each other. α axis coincides with a axis, while β axis is leading by 90°. The dq axes are synchronously rotating with the rotor. The d axis is chosen to be aligned with the direction of the rotor magnetic flux, and q axis is leading by 90°.

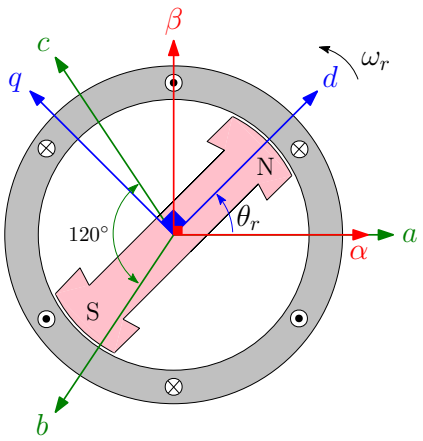

Figure A.1: Stationary and rotating reference frames of PMSM.

According to these definitions, the electrical quantities of the machine (i.e., current, voltage, and flux) can be transformed from abc frame to $\alpha\beta$ using Clarke transformation (3.3) and from $\alpha\beta$ to dq using Park transformation (3.7).

Appendix B

Control Performance Assessment

To evaluate the torque control strategies of the PMSM drive, various performance indices are defined in this appendix, which can be determined based on the captured results from the simulation and experimental system.

The torque ripple (T_e^{rip}) can be calculated using the standard deviation, as expressed by [35]

$$T_e^{rip} = \sqrt{\frac{1}{m}\sum_{k=1}^{m}(T_e^k - T_e^{av})^2}, \quad T_e^{av} = \frac{1}{m}\sum_{k=1}^{m}T_e^k, \tag{B.1}$$

where m is the number of samples, T_e^k is the instantaneous value of torque at sample k, and T_e^{av} is the average value.

A similar approach can be used to obtain the flux ripple (ψ_s^{rip}) after replacing the torque T_e in (B.1) by the stator flux amplitude ψ_s.

The steady-state torque error (T_{sse}) can be obtained by averaging the difference between the reference signal T_e^{ref} and the instantaneous value of

torque, using the following expression:

$$T_{sse} = \frac{1}{m} \sum_{k=1}^{m} \left(T_e^{ref} - T_e^k \right) \tag{B.2}$$

The average switching frequency (f_{av}) is determined by averaging the total number of switching instants of the three legs of the inverter during a fixed period [30] that is 10 ms in this work.

The percentage total harmonic distortion (THD_I) of the stator phase current can be expressed as follows [87]:

$$\text{THD}_I = \frac{\sqrt{{i_2}^2 + {i_3}^2 + \cdots + {i_N}^2}}{i_1} * 100, \tag{B.3}$$

where i_N and i_1 are the N^{th} order harmonic and fundamental components of phase current, respectively. THD_I is calculated up to 10 kHz using the Fast Fourier Transform tool of MATLAB *powergui*.